Development and Application of Models and Diagnostics for Geophysical Fluid Flows

by

Benjamin Aaron Storer

A thesis
presented to the University of Waterloo
in fulfillment of the
thesis requirement for the degree of
Doctor of Philosophy
in
Applied Mathematics

Waterloo, Ontario, Canada, 2019

Examining Committee Membership

The following served on the Examining Committee for this thesis. The decision of the Examining Committee is by majority vote.

Supervisor: Francis Poulin
Professor, Dept. of Applied Mathematics,
University of Waterloo

External Examiner: David Straub
Professor, Dept. of Atmosphere and Ocean Sciences,
McGill University

Internal Member: Kevin Lamb
Professor, Dept. of Applied Mathematics,
University of Waterloo

Internal Member: Lilia Krivodonova
Professor, Dept. of Applied Mathematics,
University of Waterloo

Internal-External Member: Cecile Devaud
Professor, Dept. of Mechanical and Mechatronics Engineering,
University of Waterloo

Author's Declaration

Abstract

This thesis presents the development and application of numerical tools for simulating and diagnosing quasi-geostrophic fluid systems.

In this thesis we present a new numerical model called *SPIQG* that is pseudo-spectral but also allows for a channel geometry and correctly computes the evolution of the zonal transport while maintaining spectral accuracy. There are numerous numerical models that simulate the non-linear evolution of the continuously stratified Quasi-Geostrophic (QG) system, and many of these models are pseudo-spectral in order to achieve high-order accuracy in the spatial discretization, but those typically assume a doubly-periodic geometry. *SPIQG* is built using the framework provided by *SPINS*, a spectral and parallel model for simulating the 3D incompressible, non-hydrostatic, Boussinesq Navier-Stokes equations. This framework provides powerful MPI-based parallelization in order to perform large-scale simulations in high powered computing environments. To validate this model, we present the results from various test cases, including quasi-geostrophic turbulence, jet destabilization, and vortex destabilization. The spectral accuracy allows for the total energy to be very well conserved as well as providing accurate calculation of power spectra, spectral fluxes, and anisotropy metrics.

Next, we propose a spectrally computed diagnostic for spatial anisotropy: a measure of the extent to which a field exhibits a bias between different orientations. The diagnostic is presented in the framework of fluid dynamics, but can be applied to any field for which Parseval's theorem applies and to which discrete Fourier, sine, or cosine transforms can be applied. The proposed metric provides both a local, or per-wavelength, measure of anisotropy, as well as a global measure. In order to determine when the anisotropy of a system is significant, the anisotropy of white noise is diagnosed both analytically and numerically. This reference anisotropy then provides a statistically sound method for determining if the observed field is significantly more or less anisotropic than noise. An idealized geophysical fluid dynamics simulation is used to illustrate the diagnostic power of the proposed metric.

These tools are then applied to study the stability of lens-shaped vortices. We compute the stability characteristics with higher accuracy and for a wider range of Burger numbers (Bu) than what was previously done. It is found that there are four distinct Bu-regions of linear instability. Over the primary region of interest, $0.1 < \mathrm{Bu} < 10$, we confirm that the first and second azimuthal modes are the only linearly unstable modes, and they are associated with vortex tilting and tearing respectively. Moreover, the most unstable first azimuthal mode is not precisely captured by the linear stability analysis because of the extra condition that is imposed at the vortex center, and accurate calculations of the second azimuthal mode requires higher resolution than was previously considered.

We also study the non-linear evolution of lens-shaped vortices in the context of this model and present the following results. First, that vortices with a horizontal length scale a little less than the radius of deformation ($\mathrm{Bu} > 1$) are barotropically unstable and develop a wobble, whereas those with a larger horizontal length scale ($\mathrm{Bu} < 1$) are baroclinicly unstable and often split. Second, the transfer of energy between different horizontal scales is quantified in two typical cases of barotropic and baroclinic instability. Third, after the instability the effective Bu is closer to unity.

Acknowledgements

It has been an adventure.
Twenty-four out of my twenty-eight years have been spent in one form of school or another.
Of those, ten years and four months were at the University of Waterloo: longer than I have lived in any other city.
There is a high probability that I have spent more time in MC than in any of my undergraduate apartments, and, I shudder to admit, quite possibly more than in my graduate housing.

I began by university career as a mathematical purist; shunning context for the beauty of abstraction.
My horror at encountering memory management in C led to my fervent belief that I could never, would never, be a programmer…
and then there was Python, and Matlab; SPINS gave me C++; there was even a spattering of Fortran, for good measure.
Now I all but live in a terminal session, and my Vim-fu grows stronger.
best laid plans indeed

This work was supported through multiple Ontario Graduate Scholarships, and was only made possibly through the incredible access to computing resources that was made available to me through ComputeCanada and the Fluids Group.

Claire Ménesguen, thank you for hosting me at IFREMER in Brest. It was an incredibly opportunity and I greatly appreciate it.

I would also like to thank my fellow lab-mates. Our social/academic community has been a great source of stimulating discussion, bizarre antics, and all-around good fun, not to mention the great food.

Marek, even though I'm not one of your students, you've always welcomed me into your group, and together we've both had a lot of fun and done some good science. Thank you.

Thank you Francis. We've shared many hours debugging code, and many pots of tea. Your guidance and support throughout this journey has been greatly appreciated. My transformation into who I am today is in no small part thanks to your influence.

My sincerest thanks to you all:
it has been an adventure.

Dedication

To my family.

> *These are the voyages of the starship Enterprise.*
> *Its continuing mission: to explore strange, new worlds;*
> *to seek out new life and new civilizations;*
> *to boldly go, where no-one has gone before.*
>
> Captain Jean-Luc Picard

Table of Contents

List of Tables **xii**

List of Figures **xiii**

1 Introduction **1**

1.1 Large-scale Oceanic Systems 2

1.1.1 Effect of Rotation 2

1.1.2 Effects of Curvature 5

1.2 Geophysical Fluid Dynamics 9

1.2.1 Geostrophic Balance: A Note on Coriolis effects 10

1.3 How large is large? 13

1.4 Technical Background 14

1.4.1 Quasi-geostrophy 14

1.4.2 Spectral Methods 16

1.4.3 Discussion 19

2 SPIQG **20**

2.1 Physical Model 22

2.1.1 Physical Decomposition 23

2.2 Boundary Conditions and Numerical Decomposition 24

2.2.1 Incorporating Circulation 25

2.2.2 Methodology 27

2.3 Implementation . . . 29
2.3.1 Spectral Diagnostics . . . 29
2.4 Demonstrations and Sample Cases . . . 32
2.4.1 Two-Dimensional Turbulence . . . 32
2.4.2 Interior Forcing . . . 34
2.4.3 Constrained Barotropic Jet . . . 34
2.4.4 Interior Vortices . . . 36
2.4.5 Forced Shear Flow . . . 38
2.5 Conclusions . . . 40
2.6 Summary of Features . . . 40
2.6.1 Summary of Limitations . . . 41

3 Spectral Quantification of Anisotropy 42
3.1 Proposed Quantification . . . 44
3.1.1 Lengthscale-dependent Anisotropy . . . 45
3.1.2 Global Metric . . . 47
3.1.3 Extension to Three-Dimensional Fields . . . 47
3.1.4 Limitations . . . 48
3.2 Anisotropy of Noise . . . 48
3.2.1 Theoretical Results . . . 48
3.2.2 Numerical Results . . . 49
3.2.3 Determining Statistical Significance . . . 50
3.3 Sample Application . . . 50
3.3.1 Comparison with Reference Gaussian Noise . . . 52
3.3.2 Anisotropy Results . . . 52
3.3.3 Comparison with McWilliams Method . . . 55
3.4 Summary and Discussion . . . 55

4 Quasi-geostrophic Lens Vortices **58**

4.1 Model Equations and Numerical Methods 60

4.1.1 Quasi-Geostrophic Equations 60

4.1.2 Initial Conditions 60

4.1.3 Formulation and Numerical Method for Linear Stability Problem . 61

4.1.4 Numerical Method for the Non-linear Dynamics 63

4.2 Linear Stability Analysis: Dependence on the Burger Number 63

4.2.1 Growth Rates of Eigenmodes and Comparisons to Previous Works . 64

4.2.2 Identification of Unstable Modes 67

4.3 Impact of the Burger Number on Non-linear Evolution 71

4.3.1 Large Burger Number Regime 71

4.3.2 Small Burger Number Regime 73

4.3.3 Azimuthal Decomposition: a Comparison with Linear Theory . . . 75

4.3.4 Main Stages of Non-Linear QG Evolution 77

4.3.5 Spectral Distribution of Energy and Energy Transfers 81

4.4 Anisotropy 87

4.5 Conclusions and Discussion 87

5 Summary and Conclusions **91**

5.1 Future Work 92

References **94**

APPENDICES **99**

A Derivations for *SPIQG* **100**

A.1 Conservation of Mass 100

A.2 Conservation of Circulation 101

A.3 Deriving the evolution equation for the mean potential vorticity 101

A.3.1 Zonally Averaged Order Rossby Zonal Momentum 101

A.3.2 Zonally Averaged Order Rossby Thermodynamic Equation 102
A.3.3 Eliminating the Ageostrophic Velocity 102
A.4 Zonal Decomposition for 2D Quasigeostrophy 103
A.4.1 Order Rossby Zonal Momentum 104
A.4.2 Order Rossby Continuity 104
A.4.3 Eliminating the Ageostrophic Velocity 105
A.5 Coefficients for F-laut 105

B Derivation of Quasi-Geostrophic Meddy Linear Stability Problem 106

List of Tables

4.1 Description of parameters and notation 61

4.2 Simulation parameters for interior lens vortex simulations 62

List of Figures

1.1 Illustration of how the centripetal force can be combined with Newtonian gravity to form an effective gravitational force. 6

1.2 Illustration of Curvature and Non-traditional Coriolis Effects 7

1.3 Illustration of Coriolis effects in large-scale pressure systems 11

1.4 Illustration of a Geostrophically Balanced Cyclone 12

1.5 Basic procedure for pseudo-spectral methods 18

2.1 Zonal mean PV for f- and β-plane turbulence 33

2.2 Wavenumber-dependent anisotropy of KE for f- and β-plane turbulence . . 33

2.3 Potential vorticity of the interior forcing demonstration 35

2.4 Potential vorticity of the leading dipole in figure 2.3 35

2.5 Potential vorticity at selected times for the barotropic jet demonstration . 37

2.6 Growth rate comparison for the unconstrained and constrained barotropic jets 38

2.7 Zonal mean fields of the forced shear flow demonstration 39

3.1 Illustration of procedure for computing anisotropy. 46

3.2 Anisotropy diagnostics for white noise 51

3.3 Anisotropy diagnostics for f-plane turbulence. 53

3.4 Comparison of wavenumber-dependent anisotropy for f- and β-plane turbulence. 54

3.5 Comparison of the presented and McWilliams anisotropy metrics for a double jet aligned along $y = -x$. 56

4.1 Linear stability analysis of lens vortices 65
4.2 Illustration of the Ash and Khorrami geometric argument. 66
4.3 Contours of the dominant mode-1 instabilities for selected Bu. 69
4.4 Contours of the dominant mode-2 instabilities for selected Bu. 70
4.5 Three-dimensional visualization of a Bu = 5 vortex at selected times. . . . 72
4.6 Three-dimensional visualization of a Bu = 0.14 vortex at selected times. . 74
4.7 Azimuthal decompositions for a selection of non-linear simulations. 76
4.8 Growth rates and energetics of selected non-linear simulations. 78
4.9 Net energy conversions and initial and terminal Bu for the non-linear simulations. 80
4.10 Linear wavenumber-dependent time-rate of change of KE and PE 82
4.11 Non-linear wavenumber-dependent time-rate of change of KE and PE . . . 83
4.12 Time averaged wavenumber-dependent time-rate of change of energy across the full linear phase. 85
4.13 Quantifications of the generation of small-scale energy. 86
4.14 Anisotropy metrics for selected lens vortex cases 88

Chapter 1

Introduction

The world's lakes, seas, and oceans are teeming with life, both metaphorically and literally. The literal life, ranging from microscopic organisms to vast blue whales, from bizarre deep-dwelling creatures to the delicious fish that we know so well, demonstrates an incredible variety of sizes and characteristics. The metaphoric life, the dynamic physical features, are no less varied in scale and behaviour. On the micro-scale there are features such as the vortex-rich dynamics of small swimming creatures and the sharp transitions in salt- and temperature-stratified structures. Slightly larger, and surface tension leads to centimetre-scale capillary waves that speed along the water's surface. Larger still, wind drives the water waves that we most commonly associate with open waters: ranging from slow, gentle waves that slowly rock ships, to strong white-caps that eject spray into the air, releasing particulates and aerating the water. Beneath the surface even larger features can be found: internal gravity waves. With a variety of generation mechanisms, these waves ride along density interfaces and can grow to massive scales, taking advantage of the reduced gravity from being submerged. Larger again are dynamical systems so large that they are influenced by the rotation and curvature of the Earth. These are the blue whales of ocean dynamics and are here-after simply termed *large-scale*; the study of such objects is the purvue of, among others, geophysical fluid dynamics (GFD).

This chapter gives a primarily heuristic introduction to the study of large-scale fluid systems. Section 1.4 provides a more technical introduction into some of the principle concepts used in this thesis: quasi-geostrophy and spectral methods. Chapter 2 presents a computational model, *SPIQG*, which was developed in order to numerically study quasi-geostrophic systems. Chapter 3 introduces a spectrally-defined metric of anisotropy, which provides a measure of the importance of orientation across a range of length-scales. Chapter 4, a nearly verbatim reproduction of Storer et al. (2018), then applies these methods to the study of quasi-geostrophic lens-shaped vortices. Finally, chapter 5 provides a brief summary of the results presented in this thesis and proposes some directions for future research.

Each of the three main content chapters, chapters 2 - 4, includes an additional introduction section which provides a more in-depth introduction to the topics discussed therein, as well as situating the presented work within the literature.

1.1 Large-scale Oceanic Systems

Large-scale oceanic and atmospheric features are abundant in nature, both terrestrial and otherwise. The raging storm of Jupiter's great red spot and Saturn's curiously hexagonal polar vortex are massive atmospheric features, both features roughly the size of Earth, and are strongly rotational features (Baines et al., 2009; Vasavada et al., 1998). On Earth, the trade winds are persistent and large-scale atmospheric features that are heavily influenced by the Earth's rotation and are part of a larger global circulation system. El Niño, a well known multi-year cycle that demonstrates the potential for powerful ocean-atmosphere interaction (Holton, 1972), is strongly impacted by large-scale eastward- and westward-propagating oceanic waves.

Because of a shift in the dominant force balance, large-scale fluid systems have a tendency towards forming vortical features. So much so that the world's oceans are a veritable panoply of vortices (Chelton et al., 2011). Their characteristics, whether they are interior- or surface-intensified, how long they live, the direction in which they spin, the salt/temperature/density structure, all depend on the context of their creation.

On sufficiently small scales, the rotation and curvature of the Earth exhibit a negligible effect on the behaviour of fluid systems. A classic misconception, popularized by, among others, the show "The Simpsons", is that the direction of flow in a drain, such as a kitchen sink or flushing toilet, is dictated by the rotation of the Earth and that, as a result, always flows in the same direction in the northern hemisphere and the opposite direction in the southern hemisphere. The reality of the situation is that the lengthscale of the flow in the drain's basin is so very small compared to planetary scales that, unless the water is nearly perfectly still and the basin is strongly symmetric, the impact of Earth's rotation is highly negligible. Instead, the initial direction of the flow is typically what dictates the direction of spin. However, when considering slowly-moving large-scale systems, effects from the Earth's spin can become significant, and even dominant.

1.1.1 Effect of Rotation

In mathematical systems, the choice of coordinate system dictates how we measure or discuss where something is situated in space or time. The most common choice of coordinate system, termed an Eulerian coordinate system, is one in which the reference points are held constant throughout time. A common example is the fixed "distant-stars" system, in which distant stars are taken to be the reference points by which position is measured. However, a canonical Earth-based coordinate system, such as latitude-longitude-elevation, is not a fixed Eulerian system, since the Earth is rotating within the "distant-stars" system.

To better illustrate this, consider a Merry-go-'Round, the face of which has been decorated like a clock. Children riding the Merry-go-'Round could use the clock numbering as a fixed coordinate system since they are within the frame of reference of the ride, and could easily communicate their positions using the clock. Meanwhile, an on-looking parent would observe the children's coordinate system as changing in time: the position of three o'clock at one moment would be different from the next.

The distinction between a fixed and accelerating coordinate system is important, since many of the physical laws used in studying fluid mechanics, such a Newton's law and conservation of energy and momentum, are derived for non-accelerating systems. As a result, the time-dependence of a fixed Earth-based coordinate system must be accounted for in the governing equations of motion. The details of such a derivation can be found in many texts, including Kundu and Cohen (section 4.12 of 2008), and will not be reproduced here. The result, however, is that

$$\vec{a} = \vec{a}_F - 2\vec{\Omega} \times \vec{u} + \Omega^2 \vec{R}, \tag{1.1.1}$$

where $\vec{a}_F$ is the acceleration with respect to the "distant-stars" coordinates, $\vec{a}$ is the acceleration with respect to the rotating coordinates (that is, from the perspective of an observer within the rotating frame), $\vec{\Omega}$ is the angular velocity with magnitude Ω, $\vec{u}$ is the velocity with respect to the rotating coordinates, and $\vec{R}$ is the component of the position vector orthogonal to $\vec{\Omega}$

The two observer-apparent terms each represent a component of the observed rotational effects: the Coriolis, $2\vec{\Omega} \times \vec{u}$, and centripetal, $\Omega^2 \vec{R}$, accelerations.

1.1.1.1 Coriolis Acceleration

Using a traditional right-handed coordinate system, $\vec{\Omega}$ points upwards (by aligning the thumb of your right hand with $\vec{\Omega}$, the curl of your fingers indicates the direction of rotation), and so in the northern hemisphere the Coriolis term induces a right-ward deflection. Note that 'right' refers to 'right with respect to the direction of motion', so that northward motions deflect eastward, eastward motion deflects southward, southward motion deflects westward, and westward motion deflects northward. In the southern hemisphere the effect is reversed to induce a left-ward deflection.

Intuitively, how can one motivate and understand the right-ward deflection of the northern hemisphere? For this, consider the following thought experiment.

Imagine a piece of paper resting on a table. The table remains fixed and unmoving, and so in this situation serves as our "fixed-stars" reference. The piece of paper, on the other hand, we can spin to simulate a rotating system. To begin, picture drawing a straight line on the piece of paper without spinning it, so that the paper is in the same reference frame as the table. The line drawn represents the pencil's path in the table's frame of reference: i.e., a non-rotating reference frame. Next reset your pencil to the original position so that the tip points at the start of your previous (straight) line. This time, you will slowly spin the paper anti-clockwise while moving your pencil in exactly the same fashion as before: that is, the pencil will move in a straight line with respect to the table. This newer line reflects the path taken within the rotating reference frame. Even though the pencil itself moved through the same path in space, the two lines are distinct: the second path peels away to the right from the original line. This is the underlying mechanism behind the observed rightward deflection induced by the Coriolis forces.

Were a bug to be sitting on the paper, they would see the pencil as moving in a curved path, while in reality it is actually the movement of the bug on the spinning paper that simply makes the pencil's path appear curved.

Should you reset the paper to its original position and repeat the process but this time spinning the paper clock-wise, you would find that the new line peels away to the left from the original line. This corresponds to the left-wards deflection in the southern hemisphere.

1.1.1.2 Centripetal Acceleration

The centripetal acceleration term, $\Omega^2\vec{R}$, always points horizontally and directly away from Earth's axis[1]. Further, this term depends only on the rotation of the Earth and on your position; unlike the Coriolis term, it doesn't depend on your velocity. If we take the rotation of the Earth to be known and constant, then the centripetal acceleration is simply a function of your position. In a similar way, if we take the mass of the Earth to already be accounted for, then the gravitation acceleration caused by the Earth can also be considered to only be a function of position: namely, your distance from the Earth's centre of mass.

Following this reasoning, it is possible to define an effective gravitational force that is the sum of these two position-dependent forces: centripetal and gravitational. In the absence of centripetal effects, the effective gravity would only depend on your distance

---

[1] Centripetal acceleration is typically used to refer to an *inwards* pointing acceleration, in contrast to the one presented here, which is pointing *outwards*. More accurately, the term discussed here is the acceleration resulting from the centrifugal forces, which point *outwards*. However, the term centripetal acceleration is used here for ease of speech.

from the centre of mass, and not latitude. In this scenario, the Earth would be, ignoring topographic features such as mountains and valleys, spherical. However, that is not the case, as the Earth demonstrates a larger centre-to-equator distance than centre-to-pole distance, as well as a thicker atmosphere at the equator than the poles. The centripetal force is precisely that which causes this deformation. By adding a horizontal outward-pointing gravity-like force to the traditional Newtonian gravity, the direction of gravity shifts from being directly towards Earth's centre to being angled slightly equatorward and is weakened in overall strength. Since the centripetal acceleration depends on the horizontal distance from Earth's axis, this effect weakens towards the poles.

Figure 1.1 illustrates this process. The horizontal magenta arrows indicate the centripetal force, which points horizontally outwards and weakens towards the pole, as indicated by the decreasing length of the arrow. The traditional Newtonian gravity, given in black, is combined with the centripetal force to produce the effective gravitational force, given in cyan. At each latitude, the modified gravity is weaker than the Newtonian gravity, again given by the arrow lengths, and is deflected to point more towards the equatorial plane.

These deviations in gravity are quite small, causing a total variation in strength of approximately 0.3% at the equator, where the effect is strongest. For the purposes of the work considered in this document, the impacts of the centripetal acceleration is negligible and only the traditional Newtonian gravity is considered.

1.1.2 Effects of Curvature

Recall the thought experiment involving moving a pencil across a spinning piece of paper that was used to illustrate the Coriolis deflection. By moving a pencil in a straight line across a spinning piece of paper, we can reproduce the deflection that arises in rotating reference frames. However, the piece of paper on a table is flat, unlike the (nearly) spherical Earth.

It is important to recognize that the circumference of latitudinal bands, that is, rings along a fixed latitude, decreases towards the poles and increases towards the equator. However, since the Earth rotates as a solid body, each latitude spins about the axis with the same angular frequency: one revolution per day. Since the equator has a greater circumference than the mid-latitudes, but revolves in the same time, the linear speed of rotation is greater near the equator and lesser near the poles.

To better understand the influence of curvature, consider figure 1.2, which illustrates how the rotation vector $\vec{\Omega}$ can be decomposed into a part that is perpendicular to the Earth, termed the traditional part, and a part that is tangential to the Earth: the non-traditional component. The component that is perpendicular to the reference point corresponds to

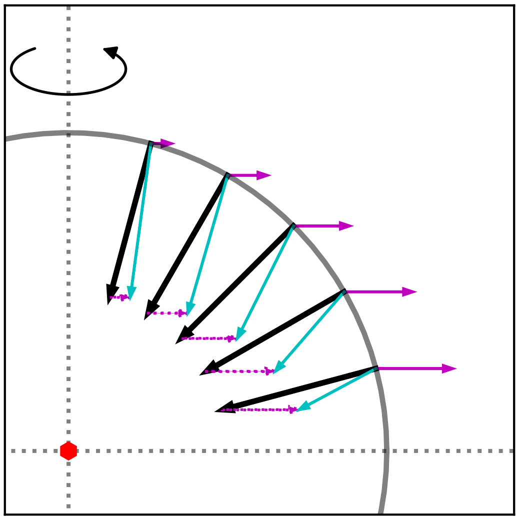

Figure 1.1: Illustration of how the centripetal force can be combined with Newtonian gravity to form an effective gravitational force. The dark grey circle denotes the Earth, the horizontal dotted line the equator, and the vertical dotted line the axis of rotation. Black arrows indicate the traditional Newtonian gravity, which point directly to the centre of the Earth (red hexagon). The solid magenta lines indicate the centripetal forces, while the dotted magenta lines simply repeat the centripetal force, but placed head-to-toe with the Newtonian gravity. The cyan arrows then indicate the resulting effective gravitational force, which is the sum of the Newtonian and centripetal forces. The length of the arrow indicates the strength of the force. Note that the relative strength of the centripetal forces has been greatly exaggerated for the purpose of demonstration.

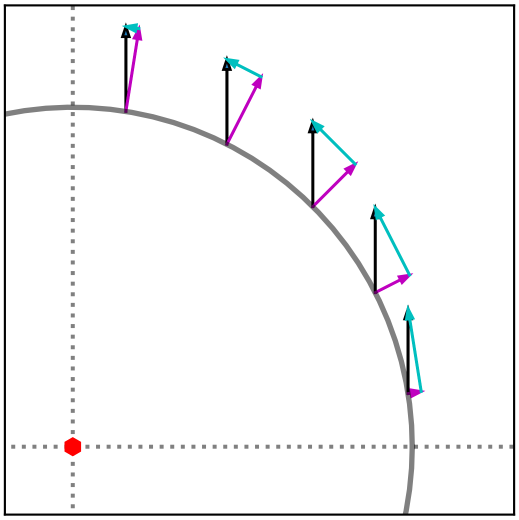

Figure 1.2: Illustration of curvature and non-traditional Coriolis effects. Each trio of arrows gives a sample decomposition of the rotation vector $\vec{\Omega}$ (black) into a locally perpendicular part (magenta, traditional approximation) and a tangential part (cyan, non-traditional). The dotted black lines indicate the equator and rotation axis while the red hexagon indicates the centre of the Earth.

rotation in the same sense of the piece of paper in the thought experiment in section 1.1.1.1: rotation in the horizontal plane. The tangential component, however, incorporates the vertical coordinate into the induced rotation.

1.1.2.1 Traditional versus Non-traditional Coriolis

Recall that the Coriolis term induces a right-ward deflection: importantly, it is rightward when looking *down* with respect to the upwards pointing traditional Coriolis term. More accurately, this is the deflection induced by the *traditional*, or locally perpendicular, term. The non-traditional component works in much the same way, inducing a right-ward deflection when looking *down* with respect to the sideways pointing rotation vector. As a result, the non-traditional term deflects eastward motion slightly upwards, upwards motion slightly westward, westward motion slightly downwards, and downward motion slightly eastward.

These non-traditional effects, however, are often neglected in geophysical settings. To understand why, it is important to consider the scales at play. At its absolute deepest, the ocean extends roughly eleven kilometres in the vertical. However, in many contexts it is only the upper few hundred metres to few kilometres that are of dynamical interest. In contrast, the horizontal extent of systems can easily reach hundreds or thousands of kilometres. This shallow aspect ratio, in addition to vertical density gradients, lead to predominantly horizontal motions in many geophysical settings, where horizontal velocities are typically much stronger than vertical velocities.

Consider again that the non-traditional terms induce eastward and westward motions from downwards and upwards motions. However, eastward and westward motions are also being induced by southward and northward motions, and those horizontal motions are likely much larger than the corresponding vertical motions. As a result, for mid-latitudes, the non-traditional Coriolis terms can generally be neglected in favour of the traditional approximation. As a matter of consistency, it is then also necessary to ignore the upward and downward deflections, since the non-traditional component would otherwise serve as an energy source.

1.1.2.2 Simplifications to the Traditional Approximation

As a result of taking the traditional approximation, the local rotation vector, the magenta arrows in figure 1.2, can be written as $(0, 0, f(\theta))$, where $f = 2\Omega\sin(\theta)$, Ω is the magnitude of the planetary rotation vector and θ is the latitude in question. There are two common approximations that are used to further simplify this term, called the f- and β-plane approximations respectively.

The f-plane approximation simplifies the Coriolis deflection by assuming that it is *independent of space*. This ultimately ignores the curvature of the Earth by instead supposing that we are considering a small enough area that the Earth be reasonably approximated as being flat (but still rotating!). Mathematically, this manifests by writing $f(\theta) = f_0$, where $f_0 = 2\Omega\sin(\theta_0)$ and θ_0 is a typical latitude for the domain in question.

The β-plane approximation slightly relaxes the f-plane assumption by instead permitting the Coriolis parameter to vary linearly with latitude. This can be thought of as approximating the Earth as a cone, which, while absurd on a planetary scale, can be very reasonable over a sufficiently small area. Mathematically, this manifests by writing $f(y) = f_0 + \beta y$, where f_0 is the same, $\beta = \frac{2\Omega}{r_{\text{Earth}}}\cos(\theta_0)$, r_{Earth} is the mean radius of the Earth, and y is the latitudinal distance (in metres) between the point of interest and the reference latitude θ_0.

Higher approximations to the Coriolis frequency are typically not used, and instead a spherical coordinate system is used to accurately implement the true Coriolis parameters.

1.2 Geophysical Fluid Dynamics

> *one of the most important questions to answer in the study of climate*
> *is to understand just what is a detail and what is essential*
>
> ---
>
> Geoffrey K. Vallis (Vallis, 2012)

With the extraordinary complexity of the governing equations of fluid motion, the Navier-Stokes equations, it is often necessary to make simplifying assumptions in order to make the problem analytically or numerically tractable. However, it is fundamentally important that these simplifying assumptions be made in a rigorous, justified, and self-consistent manner: that only details are removed, and nothing essential.

For example, the bulk of human experience suggests that air is essentially inviscid, and in a vast array of subjects it may reasonably be assumed to be so. However, it is by making exactly this seemingly reasonable assumption that one is able to conclude that airplanes cannot fly. Planes, of course, can fly, but the mechanism for generating lift relies on viscous effects, which produce a millimetres thin layer of slow-moving air along the airfoil. Outside of this very thin region the viscosity of air is negligible, but failure to account for its effects leads to a categorical shift in the predicted behaviour.

Equation (1.2.1) outlines some of the key terms in the incompressible formulation of the Navier-Stokes equations, sometimes termed the momentum equation, since it arises from conservation of momentum. This, combined with a thermodynamic equation and a conservation of mass statement form a system of equations that can be used to simulate fluid systems.

$$\rho\left(\underbrace{\partial_t\vec{u}}_{\text{Acceleration}} + \underbrace{\vec{u}\cdot\nabla\vec{u}}_{\substack{\text{Advection of the}\\ \text{flow by the flow}}} + \underbrace{2\vec{\Omega}\times\vec{u}}_{\substack{\text{Deflection of the}\\ \text{flow by rotation}}}\right) = \underbrace{-\nabla p}_{\substack{\text{Force caused by}\\ \text{pressure gradients}}} + \underbrace{\rho\vec{g}}_{\substack{\text{Gravitational}\\ \text{force}}} + \underbrace{\mu\nabla^2\vec{u}}_{\text{Viscous//dissipation}} \tag{1.2.1}$$

Mathematically, there are many ways that one can seek to simplify the Navier-Stokes equations (Kundu and Cohen, 2008). A traditional and productive way to begin is to use non-dimensionalization, in which a typical scale is chosen for the physical variables under consideration, such as a typical time-scale and length-scale, which are in turn used to scale-out the variables. For example, if the typical velocity scale is U, then the velocity u can be non-dimensionalized by $u = U\tilde{u}$, where $\tilde{u}$ is dimensionless and on the order of one. The typical scales and physical parameters, such as gravity, are then combined in a meaningful way to form a collection of dimensionless parameters, which together determine the magnitude of each term in the equation. These dimensionless parameters can be viewed as the ratio between two things; whether those things are forces, length scales, time scales, or otherwise depends on the specific context and interpretation. In the context of geophysical fluid dynamics, two important dimensionless parameters are the Rossby (Ro) and Burger (Bu) numbers.

Under an advective timescale, the Rossby number can be thought of as the ratio between the advection of the flow, either the $\partial_t \vec{u}$ or $\vec{u} \cdot \nabla \vec{u}$ term, and the Coriolis acceleration $2\vec{\Omega} \times \vec{u}$. Ro is a general measure of the importance of rotational effects: the smaller the Rossby number is, the more important that rotation is. The Burger number is often viewed as the (square of the) ratio between Rossby deformation radius and the length-scale of the flow in consideration, where the Rossby deformation radius, an important scale for large-scale systems, specifies the scale at which rotational effects are as important as buoyancy effects (Gill, 1982).

1.2.1 Geostrophic Balance: A Note on Coriolis effects

Recall that in the northern hemisphere the Earth's rotation causes a right-ward deflection for objects that are moving over long distances. To understand how this impacts geophysical systems, consider figure 1.3, which presents the situation in which a low pressure region is encircled by a high pressure area. The change in pressure induces a force that seeks to drive material from the high pressure and into the lower. However, if we suppose that this diagram spans a sufficiently large area, as is often the case with atmospheric pressure systems, then the inwards pressure-driven flow is deflected rightwards, producing a net anti-clockwise motion. Were the same pressure system to occur in the southern hemisphere, the deflection would instead be leftwards, producing a net clockwise rotation.

The term *cyclonic* describes systems having rotation in the same sense of the Earth, which is anti-clockwise when viewed from above the northern pole and clockwise when viewed from below the southern pole; much as how a clock, when viewed from behind, would appear to move anti-clockwise, while moving clockwise when viewed normally. This means that anti-clockwise rotation in the northern hemisphere and clockwise rotation in the southern hemisphere are both termed cyclonic, and would both arise from a high pressure region encircling a low pressure area. Flows rotating in the opposite sense as the Earth are termed anti-cyclonic and would arise from exchanging the high and low pressure regions in figure 1.3.

Systems in which the pressure gradient is balanced by the Coriolis forces are termed geostrophic (geo 'earth' + stroph 'to turn'). Pressure gradients always drive to move

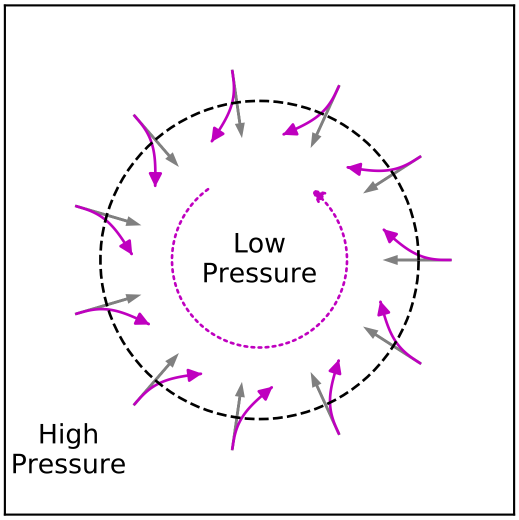

Figure 1.3: Illustration of Coriolis effects in large-scale pressure systems. The circular dashed black line demarcates the separation between a high pressure region (outside) and a low pressure region (inside). The grey arrows indicate the pressure-induced motions in the absence of rotation. The solid magenta arrows indicate the rightward deflection caused by rotation (assuming northern hemisphere). The deflections of the inward motions induce a mean rotating flow, indicated by the dotted magenta arrow.

material from high pressure areas into low pressure areas. As a result, we typically think of fluid as moving *down* pressure gradients: from high to low. However, geostrophically balanced systems behave differently. While pressure still exerts a force to push material from high pressure areas to low pressure areas, that force is counteracted by the deflections caused by the Earth's rotation. Figure 1.4 illustrates how geostrophic balance serves to maintain circulating flows around low pressure areas. This force balance leads to what can initially seem as counter-intuitive behaviour: the fluid moves *along* lines of constant pressure, not across them.

Simple Demonstration

To help illustrate the strength of geostrophic balance, consider the following hypothetical setting, adapted from Vallis (2012). Suppose the elevation of an ocean's surface increases by one metre ($\Delta h = 1$m) over a distance of one thousand kilometres ($L = 1{,}000{,}000$m): an inclination of approximately 0.00006°. Suppose next that the primary source of pressure at a point is the weight of the water above it; this assumption is known as hydrostatic

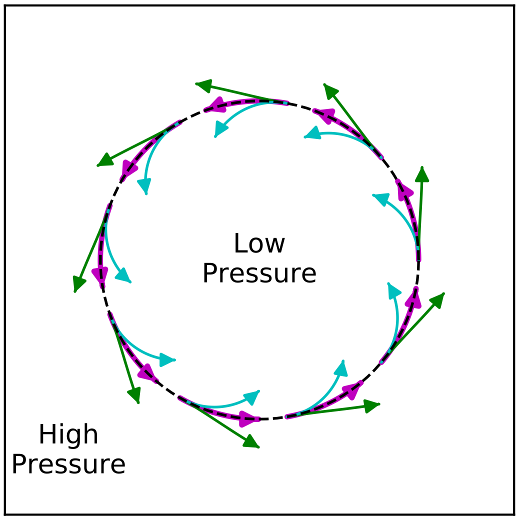

Figure 1.4: Illustration of a geostrophically balanced cyclone. The circular dashed black line demarcates the separation between a high pressure region (outside) and a low pressure region (inside). The magenta arrows indicate the motion caused by the cyclone, in which the outwards deflection from rotation (green arrows) and inwards deflection from pressure (cyan arrows) balance each other. The result is flow that moves along lines of constant pressure.

balance, and is generally valid for geophysical contexts. Under this assumption, the pressure gradient caused by this elevation would then be $\Delta p/L = \rho \cdot g \cdot \Delta h/L$, where ρ is the density of water and g is the acceleration due to gravity.

We would then like to ask, *what velocity would be required to maintain geostrophic balance?* Suppose a mid-latitude setting, for which a horizontal scale of one thousand kilometres is nearing the upper limit of an f-plane approximation. Under such an approximation, the magnitude of the Coriolis term is then $\rho \cdot f_0 \cdot U$, where again ρ is the density of water, $f_0 \approx 10^{-4}\,\mathrm{s}^{-1}$ in mid-latitudes, and U is the magnitude of the geostrophic velocity.

Equating these two terms under geostrophic balance yields that the resulting geostrophic velocity is approximately 10 centimetres per second ($U \approx 10^{-1}$m/s). Knowing the velocity scale, we can now go further to compute that the Rossby number associated with such a flow is $\mathrm{Ro} = U/(fL) \approx 10^{-3} \ll 1$.

A Note on Equatorial Dynamics The equatorial and near-equatorial regions provide an interesting dynamical change from the mid-latitude regions for a few reasons. First, an f-plane approximation is inappropriate in equatorial regimes, since f_0 vanishes at the equator. Instead, it is necessary to use a β-plane approximation. Additionally, the equator serves as a wave-guide, allowing the formation of additional wave types in the ocean's interior along the equator. While the equatorial region provides a large supply of interesting physical and dynamical features, it is not considered in this thesis, and instead emphasis is placed on the mid-latitudes.

1.3 How large is large?

So far the term "large-scale" has been used with only the vague definition of "large enough to be impacted by rotation". However, it is important to ask: *how large is large?*

First, how large does a system need to be to be influenced by the rotation of the Earth? Answering this question requires introducing a new term, the Rossby radius of deformation, often abbreviated as simply the deformation radius and denoted by L_D. This term will be formally defined in the technical background (section 1.4), but can be intuitively thought of as the length scale for which rotational effects are as important as buoyant effects. The two main requirements for a system to be influenced by the rotation of the Earth are that $\mathrm{Ro} < 1$ and $L_D \lesssim L$. Note that these conditions are only meant as general guides, and not to be considered absolute restrictions. For the former requirement, setting $\mathrm{Ro} = 0.1$ and taking typical mid-latitude values of $f_0 = 10^{-4}\,\mathrm{s}^{-1}$, and $U = 0.1$m/s gives a length scale of ten kilometres. For the latter requirement, a typical mid-latitude value for the Rossby deformation radius is roughly 10–30 km for internal motions and 1000 km for surface motions Gill (1982). Combined, these suggest that at mid-latitudes interior motions on scales of 10km or larger could be reasonably considered large enough to be impacted by rotation.

Having determined when rotation matters, we now investigate when, and to what extent, curvature must be incorporated. Following the f- and β-plane approximations, we can approximate the length-scales on which each is applicable. First, we can readily determine the length-scale at which an f-plane approximation is insufficient and a β-plane should be used. Consider the ratio $\beta L/f_0$, which is the ratio of the linear Coriolis deviation βL over a latitudinal distance L compared to the reference value f_0. Using the equations given for each approximation, it is a simple matter to determine the lengthscale L at which the variations in the Coriolis frequency are, for example, 10% of the reference frequency, possibly indicating that a β-plane should be used. For example, at 10° latitude $L \approx 100$ km, at 40° latitude $L \approx 500$ km and at 60° latitude $L > 1,000$ km. Since the β parameter is a first approximation to incorporating curvature, these length-scales can be considered to be the scales at which the curvature of the Earth becomes important.

1.4 Technical Background

This section provides a general technical background to the quasi-geostrophic model and spectral methods. In each of the three main body chapters, chapters 2 - 4, additional and more in-depth introduction is given to the specific details for the work presented therein.

1.4.1 Quasi-geostrophy

The quasi-geostrophic model, which is first presented in Charney (1948), is derived in many sources (Vallis, 2006; Pedlosky, 1987), and those details will not be repeated here. Instead, a brief summary of the underlying assumptions and characteristics of the quasi-geostrophic system are discussed. Two necessary parameters for such a discussion are the deformation radius, L_D, and the Burger number, Bu. The deformation radius is defined as

$$L_D = \frac{\sqrt{gH}}{f} \qquad \text{or} \qquad L_D = \frac{NH}{f}, \tag{1.4.1}$$

where the first definition applies to two-dimensional horizontal sytems and the second applies to three-dimensional settings. g, H, and N provide the acceleration due to gravity, characteristic depth of the fluid, and buoynacy frequency, respectively. The Burger number is defined as

$$\mathrm{Bu} = \left(\frac{L_D}{L}\right)^2. \tag{1.4.2}$$

The main assumptions underlying the quasi-geostrophic simplification are:

- Ro $\ll 1$: that the timescale on which the flow evolves is significantly larger than the local inertial timescale.
- Bu $\lesssim 1$: that the length-scales of the flow are on the order of, or larger than, the deformation radius.
- Bu $\not\ll 1$: fluid systems whose length-scales greatly exceed the deformation radius fall under planetary geostrophy, not quasi-geostrophy
- Advective time-scale; that the primary mechanism by which matter and energy moves is through advection.
- Hydrostasy: that the pressure at a given location is due solely to the weight of the fluid above it, not the fluid motion.

In addition to the traditional QG assumptions, the work presented here makes use of additional simplifications. First, we restrict our attention to Cartesian coordinate systems, incorporating first order curvature effects through the use of a β-plane when necessary. Second, we will assume a linear background stratification to focus on idealized settings. While not strictly necessary, it does simplify the set-up and algebra considerably.

Equation (1.4.3) states the governing equation for the quasi-geostrophic model in the absence of external forcing. q is the potential vorticity, which measures the local rotation or spin of the fluid flow, $\vec{u}$ is the horizontal velocity vector, and ∇_H is the horizontal gradient operator. Physically, this equation states that potential vorticity is conserved following the flow: that is, as a fluid parcel is advected through the domain, its potential vorticity remains unchanged.

$$\partial_t q + \vec{u} \cdot \nabla_H q = 0 \tag{1.4.3}$$

The definition of the potential vorticity in relation to the other physical variables depends on the context of the problem. In a two-dimensional system q is given by

$$q = \nabla_H^2 \psi - L_D^{-2} \psi, \tag{1.4.4}$$

where ψ is the streamfunction such that $u = -\partial_y \psi$ and $v = \partial_x \psi$. The former term, $\nabla_H^2 \psi$, represents relative vorticity, and the latter, $L_D^{-2}\psi$, vortex stretching, with the ratio between the two terms being the Burger number.

In the case of a three-dimensional system, the potential vorticity is defined by

$$q = \nabla_H^2 \psi + \frac{f^2}{N_0^2} \frac{\partial^2}{\partial z^2} \psi, \tag{1.4.5}$$

where once again the ratio between the two terms is the Burger number and N_0 is the buoyancy frequency, which measures the strength of the stratification.

1.4.1.1 Properties

It is important to note that the QG model has a single evolution equation, but four state variables: q, u, v, and ψ. Because of this, it is necessary to invert the potential vorticity equation, either (1.4.4) or (1.4.5) depending on the problem, to determine the streamfunction. Once ψ is known, the velocity fields can then be computed through differentiation. Now that the four state variables are known, q can be evolved to the next time-step.

Four useful diagnostic variables in QG are kinetic energy (KE), potential energy (PE), enstrophy, and circulation. These variables are defined in equations (1.4.6) - (1.4.9).

$$\text{KE density} = \frac{1}{2}\rho_0\left(u^2+v^2\right) = \frac{1}{2}\rho_0\left|\nabla_H\psi\right|^2, \tag{1.4.6}$$

$$\text{PE density} = \begin{cases} \frac{1}{2}\rho_0 L_D^{-2}\psi^2; & \text{2D} \\ \frac{1}{2}\rho_0\left(\frac{f_0}{N_0}\partial_z\psi\right)^2; & \text{3D} \end{cases}, \tag{1.4.7}$$

$$\text{Enstrophy density} = q^2, \tag{1.4.8}$$

$$\text{Circulation} = \oint_{\partial\Omega} \vec{u}\cdot d\vec{t}. \tag{1.4.9}$$

Under QG dynamics, domain-integrated enstrophy and total energy densities (equal to the sum of KE and PE) are conserved, as is circulation.

Quasi-geostrophy also presents the interesting property of having an inverse energy cascade in which energy is consecutively passed to larger and larger scales through vortex interaction. Simultaneously, QG presents a direct enstrophy cascade, which causes enstrophy to be transferred to smaller and smaller scales. This is in contrast to the direct energy cascade that is present in smaller scale dynamics.

1.4.2 Spectral Methods

Pseudo-spectral Methods are a class of tools used to numerically evaluate partial differential equations that combine traditional spectral methods by computing derivatives in spectral space while performing arithmetic operations, such as adding and multiplying fields, in physical space. This combines the accuracy of spectral derivatives, which, by using all of the information available, maintain the highest-possible accuracy, while avoiding the need for computing convolutions. At their core, spectral methods utilize transforms, most commonly Fourier transforms, to convert the physical-space fields into spectral-space fields. Once in spectral space, the choice of transform basis determines the method of differentiation.

Consider a physical domain of length L_x, which is discretized onto N_x cell-centred points with uniform spacing $\Delta x = L_x/N_x$. The wavenumbers k_x arising from a discrete Fourier transform can be taken to be

$$k_x \in \{0, \Delta k, 2\Delta k, \dots, k_{\text{Nyq}} - \Delta k, -k_{\text{Nyq}}, \Delta k - k_{\text{Nyq}}, \dots, -\Delta k\},$$

where $\Delta k = 2\pi/L_x$ is the spacing in spectral-space, and $k_{\text{Nyq}} = \pi/\Delta x$ is the highest-resolvable wavenumber, called the Nyquist frequency, which corresponds to a signal that contains two grid points per period. This is not a unique choice, but is common; note also that the middle wavenumber can be viewed as $\pm k_{\text{Nyq}}$, since it represents both (Press et al., 1986, p. 497).

As a side note, since k_{Nyq} is the largest wavenumber, it can be thought of as the length of the spectral domain, or L_k. We would then have that $\Delta k \sim L_x^{-1}$ and $L_k \sim \Delta x^{-1}$, so that higher resolution in spectral space can be achieved by taking a larger physical domain, while higher resolution in physical space corresponds to a larger spectral domain.

The discrete Fourier transform computes the spectral coefficients c_k for each wavenumber such that

$$f(x) = \sum_{k \in k_x} c_k e^{ikx}. \tag{1.4.10}$$

From this, it can be readily seen that the spatial derivative could then be expressed as

$$\frac{\partial}{\partial x} f(x) = \sum_{k \in k_x} ikc_k e^{ikx}, \tag{1.4.11}$$

That is, differentiation is performed by simply multiplying the coefficient vector c_k by the appropriate wavenumber vector k_x. Figure 1.5 outlines the general procedure when applied to one of the advection terms: $u\partial_x u$.

Filtering As a result of their high accuracy, spectral schemes introduce very little numerical dissipation. While this is generally beneficial, it does mean that inviscid systems will have no means of removing small-scale energy, which, when combined with physical mechanisms that cascade energy to smaller scales, can lead to an unphysical build-up of small-scale energy. This leads to a common practice in spectral methods called filtering, in which energy is explicitly extracted at small scales by scaling the spectral coefficients appropriately: $c_k \mapsto \mathfrak{f}(k) \cdot c_k$, where $\mathfrak{f}(k) \in [0, 1]$ is called the spectral filter. Constructing a filter is typically context dependent, but the general goal is to minimally damp the system while maintaining numerical stability. In the case of powerful cascades towards small-scales, abrupt filters can often introduce spectral ringing, and so broader and weaker filters may be more desirable.

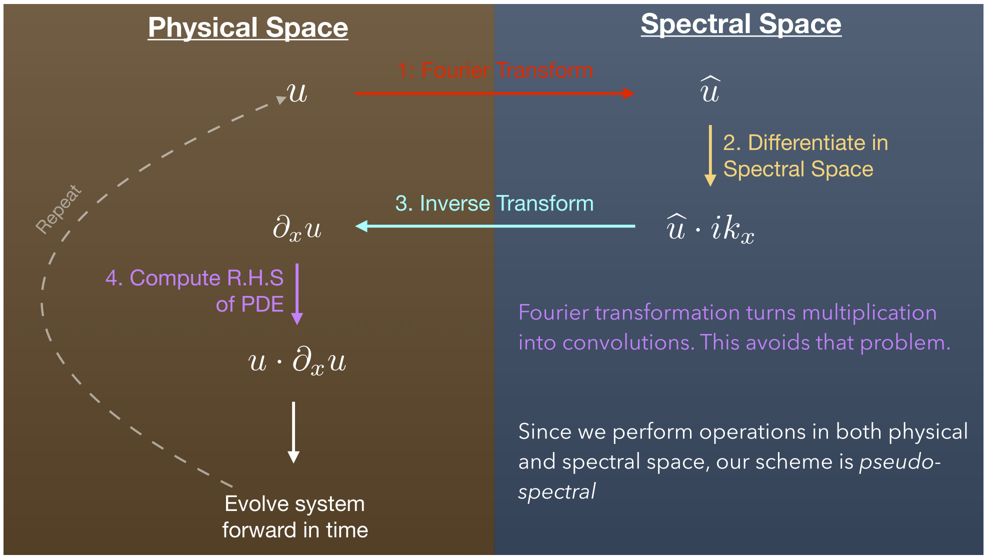

Fourier transformation turns multiplication into convolutions. This avoids that problem.

Since we perform operations in both physical and spectral space, our scheme is *pseudo-spectral*

Figure 1.5: The basic procedure for pseudo-spectral methods, outlined for one part of the advection: $u\partial_x u$.

The numerical model presented in chapter 2 uses the spectral filter provided in Subich et al. (2013), namely that

$$\mathfrak{f}(k) = \begin{cases} 1; & |k| \leq k_{\text{cut}} \\ \exp\left(-\alpha \left[\frac{|k|-k_{\text{cut}}}{k_{\text{Nyq}}-k_{\text{cut}}}\right]^{\beta}\right); & |k| > k_{\text{cut}} \end{cases}, \tag{1.4.12}$$

where α, β, and k_{cut} are parameters that determine the specific shape and strength of the filter.

Aliasing An additional concern that arises in pseudo-spectral methods results from the use of a discretized domain. High frequency signals, when sampled down to a discrete domain, can project onto lower frequencies: specifically, frequencies exceeding the Nyquist frequency appear as lower frequency signals. One method for removing aliasing is to remove energy from all wavenumbers exceeding two-thirds of the Nyquist frequency (Trefethen, 2000). The only aliasing-susceptible frequencies would then fall in $k_{\text{Nyq}} \leq k_{\text{susceptible}} \leq \frac{4}{3}k_{\text{Nyq}}$, which are in turn aliased onto $\frac{2}{3}k_{\text{Nyq}} \leq k_{\text{aliased}} \leq k_{\text{Nyq}}$, and removed by the filter. It is important to recognize, however, that two thirds of the Nyquist frequency corresponds to a wavelength of three grid points, so this does not strongly prohibit the formation of small scale features.

Boundary Conditions Fourier transforms implicitly assume that the transformed signal is periodic. While this means that periodic boundary conditions are free to implement, it does mean that some care needs to be taken to impose non-periodic boundary conditions. Two common alternatives in spectral methods include the use of discrete sine and discrete cosine transforms, which respectively represent zero Dirichlet and zero Neumann conditions. Another common alternative for implementing more general boundary conditions is to utilize Chebyschev grids, which uses a specific grid-point arrangement and differentiation matrix to maintain spectral accuracy (Trefethen, 2000). However, Chebyschev grids necessarily cluster grid points near the boundary, which, depending on the context in consideration, may be undesirable, since it often places a greater constraint on the time step in addition to reducing the resolution of interior features.

It is important to note that the choice of decomposition for each field is not independent. Consider the x-decompositions for q, ψ, and v. Equations (1.4.4) and (1.4.5) state the relationship between q and ψ. q appears undifferentiated, while ψ appears both undifferentiated (with respect to x) and with a second derivative. As a result, if q were decomposed with a sine basis, then ψ would also need to be decomposed with a sine basis. However, since $v = \partial_x \psi$, a sine basis in ψ would require a cosine basis in v.

Meanwhile, unless a costly spectral interpolation scheme is used, choosing a Chebyshev basis for one field would require the use of a Chebyshev basis for all fields. Similarly, using a Fourier basis for one field requires using a Fourier basis for all fields. The correct choice of decomposition for a spectral quasi-geostrophic model is discussed in more depth in the following chapter.

1.4.3 Discussion

Quasi-geostrophy and spectral methods both make fairly strong assumptions about the type of problem being considered. As a result, they are not as broadly applicable as other tools. The primitive equations, hydrostatic or otherwise, can encompass a broader range of dynamic features that are not permitted within the more restrictive QG framework. In contrast to spectral methods, local numerical schemes such as finite volumes or finite elements would allow substantially broader applicability as regards domain geometry, while simultaneously reducing the communication costs associated with parallelization. However, quasi-geostropy and spectral methods each provide very powerful tools for studying the subset of problems to which they apply. The reduced dynamical complexity of QG also provides a strong reduction in numerical complexity, which greatly facilitates the study of fluid flows in this regime. The geometric and functional constraints imposed by spectral methods ultimately provide access to a numerical scheme that maintains the highest-possible accuracy in spatial differentiation, nearly eliminating the influence of artificial numerical dissipation.

Chapter 2

SPIQG: Spectral Parallel (Incompressible) Quasi-Geostrophy with Channel Geometries; a SPINS extension

The quasi-geostrophic (QG) model, first presented in Charney (1948), provides a simplification of the Navier-Stokes equations by making simplifying assumptions that are appropriate to describe the dynamics of some geophysical flows at large-scales. In particular, the QG model assumes that the timescale of the motion is much longer than the rotational period and that isopycnal displacements are small (Vallis, 2006). QG describes flows that are nearly in geostrophic and exactly in hydrostatic balance, and typically govern large-scale oceanic and atmospheric dynamics. Provided that the underlying assumptions are satisfied, the QG model is very attractive because of its relative simplicity in comparison to the Boussinesq Primitive Equation model (p. 124 - 128 of Kundu and Cohen, 2008). The numerical advantages are threefold: 1) there is only one temporal equation to evolve; 2) the Poisson equation for pressure is much simpler than the non-hydrostatic version, and 3) gravity waves are completely filtered out, which allows for significantly larger time steps.

When constructing a numerical method, care should be taken in choosing a particular spatial discretization. For mildly idealized settings: rectangular domains, simple boundary conditions, and essentially smooth systems, pseudo-spectral methods provide the highest-possible order of convergence for computing spatial derivatives (Trefethen, 2000; Durran, 2010). While it is possible to extend spectral methods to consider more complex geometries (cf. mapped domains in Subich et al., 2013), this chapter focuses on the simpler case of rectangular geometries. Pseudo-spectral models rely on using operators, traditionally

Fourier transforms, to transform the relevant fields from physical-space into spectral-space, in which derivatives can be readily computed with great accuracy given that the features are sufficiently well resolved. Spatial derivatives are easily computed in Fourier space, with multiplication, addition, and time-evolution performed in physical space after an inverse transform is applied. Since operations are performed in both physical- and spectral-space, these methods are known as pseudo-spectral, but are often simply referred to as spectral methods.

However, the requirement of transforming between physical- and spectral-space imposes restrictions on the type of numerical simulations to which pseudo-spectral methods can be applied. Shocks, discontinuities, and under-resolved features can produce numerical errors that manifest themselves as spectral ringing and aliasing. Two popular techniques for mitigating these features are artificial viscosity and spectral filtering. Artificial viscosity simply adds a viscosity term to the modelled system of partial differential equations. Spectral filtering directly modifies the coefficients in spectral-space in order to stabilize the system by removing energy from small scales, while having a minimal impact on the evolution of the system. Moreover, the nature of physical-spectral transformations requires global information, which can impede the ability to efficiently parallelize numerical schemes. However, since spectral methods produce the highest-possible accuracy when computing derivatives, they provide an optimal methodology for the simulations to which they apply.

It is important to recognize that there are many QG models available in the literature. Flierl and Pedlosky (2007) used a one-layer pseudo-spectral model to simulate double-periodic QG systems with hyperviscosity, with application to the destabilization of jets. Poulin et al. (2010) then used a two-layer pseudo-spectral model to study the stability of forced shear flow in a channel. However, these models do not permit mean zonal transport to evolve and only considered spatially-uniform forcing fields. Nadeau and Straub (2009) simulated the two-layer QG system with a third order Adams-Bashforth time-stepping scheme, which is the same as used in *SPIQG*, with a multigrid method to solve the inversion problem. Aside from the restriction to rectangular domains, the boundary conditions are fairly relaxed, permitting channels, basins, and channels with peninsula-like protrusions. Tulloch and Shafer Smith (2006, 2009) use a finite-depth surface QG model that modifies the stratified surface QG system by replacing the condition that the streamfunction vanishes at infinity with the requirement that the buoyancy anomaly vanishes at finite depth. The QUAGMIRE model (Williams et al., 2009) uses a hybridized finite difference / spectral model to simulate the QG system on an annulus in two-layer cylindrical coordinates. The hybridization comes from taking a normal mode decomposition in the azimuthal direction while using finite differencing in the radial direction to compute spatial derivatives. The model presented in this manuscript, *SPIQG*, builds upon the work of Flierl and Pedlosky (2007); Poulin et al. (2010) and provides a novel and significant extension by: a) allowing for the evolution of net zonal transport and circulation, b) greatly relaxing the restriction on forcing fields by only requiring the third derivative and higher vanish at the channel walls, c) being able to solve both the one-layer and vertically stratified QG equations, and d) building on the powerful parallel framework provided by SPINS.

2.1 Physical Model

The quasi-geostrophic model (Charney, 1948) is an approximation to the Navier-Stokes system that is appropraite for the study of large-scale, rotation-dominant fluid systems. Flows that evolve under the QG system are heavily influenced by Coriolis deflections, and the governing equation states that, in the absence of forcing and dissipation, potential vorticity is conserved following the flow (Vallis, 2006). A primary force balance in QG systems is between those of pressure gradients and Coriolis deflections. The evolution equation for the quasi-geostrophic model can be expressed as:

$$\frac{\partial}{\partial t}q + J(\psi, q + \beta y) = \mathcal{F} + \mathcal{D}, \tag{2.1.1}$$

where $\psi(x, y[, z], t)$ is the stream function, $q(x, y[, z], t)$ is the potential vorticity (PV), and $[, z]$ denotes the optional dependence on z. $\mathcal{F}$ and $\mathcal{D}$ denote the forcing and dissipation respectively, J denotes the Jacobian operator ($J(f, g) = \partial_x f \partial_y g - \partial_y f \partial_x g$), and β is the Coriolis β-plane parameter.

The relationship between the potential vorticity and the streamfunction depends on the dimensionality of the problem. The streamfunction always relates to the horizontal velocity components via $(u, v) = (-\partial_y \psi, \partial_x \psi)$. For the purposes of this manuscript, the system is restricted to being either one-layer or three-dimensional with linear stratification. In a one-layer system, $q = \left[\nabla_H^2 - L_D^{-2}\right]\psi$, where $L_D^2 = gH/f_0^2$ is the squared external Rossby deformation radius, while in the case of linear stratification, the potential vorticity is defined as $q = \left[\nabla_H^2 - (f_0/N_0)^2 \frac{\partial^2}{\partial z^2}\right]\psi$, where f_0 and N_0 are the constant f-plane Coriolis and buoyancy frequencies, respectively. The one-layer system can be extended to a multi-layer scheme, as in Pedlosky (section 6.16 of 1987), but this particular extension is not yet implemented and will not be discussed here.

Under QG dynamics, both mass and circulation are conserved, which can be expressed as

$$\frac{d}{dt}\iint_{\Omega} \psi \, dA = 0 \quad \text{and} \quad \frac{d}{dt}\oint_{\partial\Omega} \vec{\nabla}_H \psi \cdot \widehat{n} \, ds = 0 \tag{2.1.2}$$

respectively, where Ω denotes the computational domain.

Since the presented model uses a novel decomposition of the physical fields, the derivation of quasi-geostrophy is revisited. These equations will be used later to rigorously derive the model equations. Following Vallis (p. 215 of 2006), the non-dimensional momentum, thermodynamic, hydrostatic, and Boussinesq mass conservation equations are given by:

$$
\begin{aligned}
\mathrm{Ro}\left(\frac{\partial}{\partial t}+u\frac{\partial}{\partial x}+v\frac{\partial}{\partial y}+w\frac{\partial}{\partial z}\right)u-v &= -\frac{\partial}{\partial x}\phi+\mathrm{Ro}\mathcal{F}_{m,x} && (2.1.3)\\
\mathrm{Ro}\left(\frac{\partial}{\partial t}+u\frac{\partial}{\partial x}+v\frac{\partial}{\partial y}+w\frac{\partial}{\partial z}\right)v+u &= -\frac{\partial}{\partial y}\phi+\mathrm{Ro}\mathcal{F}_{m,y} && (2.1.4)\\
\mathrm{Ro}\left(\frac{\partial}{\partial t}b+u\frac{\partial}{\partial x}b+v\frac{\partial}{\partial y}b\right)+\mathrm{Bu}\cdot w &= \mathrm{Ro}\mathcal{F}_b && (2.1.5)\\
\frac{\partial}{\partial z}\psi &= b && (2.1.6)\\
\frac{\partial}{\partial x}u+\frac{\partial}{\partial y}v+\frac{\partial}{\partial z}w &= 0, && (2.1.7)
\end{aligned}
$$

where the context-dependent forcing fields $\mathcal{F}_{m,x}$ and $\mathcal{F}_{m,y}$, which denote the momentum forcing in the x- and y-momentum equations respectively, are assumed to not influence the $\mathcal{O}(1)$ balance. The non-dimensional parameters, Ro and Bu, respectively the Rossby and Burger numbers, are defined as

$$
\mathrm{Ro}=\frac{U}{f_0L} \qquad \mathrm{Bu}=\left(\frac{N_0H}{f_0L}\right)^2, \tag{2.1.8}
$$

where U, L, and H are respectively characteristic velocity, horizontal length, and height scales for the system. u, v, and w denote the zonal, meridional, and vertical velocities respectively, b indicates the buoyancy field, and ϕ the non-dimensional pressure.

The geostrophic relations are obtained by taking the $\mathcal{O}(1)$ balance in the horizontal momentum equations and hydrostatic balance:

$$
u_g=-\frac{\partial}{\partial y}\psi_g, \qquad v_g=\frac{\partial}{\partial x}\psi_g, \qquad b_h=\frac{\partial}{\partial z}\psi_g, \tag{2.1.9}
$$

where subscripts g and h denote geostrophic and hydrostratic balance respectively, while the elliptic equation that defines the PV in terms of the streamfunction is

$$
q=\left(\frac{\partial^2}{\partial x^2}+\frac{\partial^2}{\partial y^2}+\frac{1}{\mathrm{Bu}}\frac{\partial^2}{\partial z^2}\right)\psi. \tag{2.1.10}
$$

2.1.1 Physical Decomposition

A meaningful physical decomposition is to express the physical fields as the sum of a term with zero zonal mean (ZZM) and a zonally-independent (ZI) term. The decompositions are written as:

$$q = \widehat{q} + \langle q \rangle\,, \quad \psi = \widehat{\psi} + \langle \psi \rangle\,, \quad u = \widehat{u} + \langle u \rangle\,, \quad v = \widehat{v} + \langle v \rangle\,, \tag{2.1.11}$$

where $\widehat{\cdot}$ terms have ZZM, $\langle \cdot \rangle$ terms are ZI, and the $\langle \cdot \rangle$ operator computes the zonal average.

Following Vallis (2006), the evolution equation for the full PV that incorporates the momentum forcing in equations 2.1.3 and 2.1.4 can be expressed as

$$\left(\frac{\partial}{\partial t} + u\frac{\partial}{\partial x} + v\frac{\partial}{\partial y}\right) q = \frac{1}{\mathrm{Bu}}\frac{\partial}{\partial z}\mathcal{F}_b + \frac{\partial}{\partial x}\mathcal{F}_{m,y} - \frac{\partial}{\partial y}\mathcal{F}_{m,x}. \tag{2.1.12}$$

However, after decomposing $q = \widehat{q} + \langle q \rangle$, it is necessary to derive the evolution equation for each component. The evolution equation for $\langle q \rangle$ can be obtained by combining the zonally averaged equations appropriately, which is outlined in appendices A.3–A.4 for both the two- and three-dimensional cases. Ultimately, the evolution equation for the zonally averaged potential vorticity can be expressed as:

$$\frac{\partial}{\partial t}\langle q \rangle + \frac{\partial}{\partial y}\langle v_g q \rangle = 0. \tag{2.1.13}$$

Physically, this states that the zonal average of PV evolves due to the meridional gradient of the zonal average of the meridional flux of the PV. The evolution for the ZZM component can then be determined via $\frac{\partial}{\partial t}\widehat{q} = \frac{\partial}{\partial t}q - \frac{\partial}{\partial t}\langle q \rangle$, which is given in equation (2.2.15).

2.2 Boundary Conditions and Numerical Decomposition

The physical decomposition of $\psi = \widehat{\psi} + \langle \psi \rangle$ makes no assumptions about the numerical methodology, and instead only decomposes the physical equations. We now proceed to consider the physical system from within a pseudo-spectral framework: namely that we will seek to use spectral differentiation for spatial derivatives. However, the details of implementation will depend heavily on the nature of the boundary conditions (BCs). In the absence of viscosity, the physical boundary condition is no normal flow, which, when restricted to a zonal channel, reduces to $v = 0$ along the north and south walls. Under quasi-geostrophy, this gives that $\frac{\partial}{\partial x}\psi = 0$ at the boundaries so that the stream-function is constant on the channel walls, where it is important to note that the constant can be non-zero and time-varying.

In pseudo-spectral models, periodic BCs, as would occur in the zonal direction, can be easily implemented using discrete Fourier transforms (DFTs). Generally, Dirichlet and

Neumann conditions can be implemented using discrete cosine and discrete sine transforms (DCTs and DSTs respectively): fields projected onto a cosine basis (DCTs) will automatically satisfy zero Neumann conditions, whereas those projected onto a sine basis (DSTs) will automatically satisfy zero Dirichlet conditions.

As regards the streamfunction, DCTs (Neumann conditions) would not ensure that ψ is constant along the walls, whereas DSTs (Dirichlet conditions) would too strictly enforce $\psi = 0$ on the walls. Moreover, since the meridionally-integrated zonal transport, $\int_0^{L_y} u \, \mathrm{d}y$, is proportional to the difference of the streamfunction between the north and south walls, DSTs would then remove the possibility for non-zero net zonal transport.

Consequences for ZI Fields

Since the zonal average of a field is by definition ZI (independent of x), $\langle v \rangle = \frac{\partial}{\partial x} \langle \psi \rangle \equiv 0$, so that the zonal mean fields necessarily satisfy the physical boundary conditions, regardless of the choice of decomposition. This permits the use of DCTs for $\langle \psi \rangle$, which would permit a non-zero mean streamfunction at either wall, allowing for the formation of net zonal transport. However, since DCTs correspond to Neumann boundary conditions, this would imply that $\langle u \rangle = -\frac{\partial}{\partial y} \langle \psi \rangle = 0$ on the walls, so that the ZI fields satisfy both no-slip and no-flux conditions. As a result, using DCTs for $\langle \psi \rangle$ would permit the evolution of net zonal flow, but would forbid non-zero circulation.

Consequences for ZZM Fields

The ZZM streamfunction, $\widehat{\psi}$, provides the zonal structure of the flow. Since the mean zonal transport can be incorporated in the ZI fields, this can be viewed as the deviation from the background moving frame, permitting the use of DSTs (Dirichlet conditions) for the meridional transform of $\widehat{\psi}$. As a result, the ZZM fields will be unable to express non-zero net zonal transport, which is introduced by the ZI fields. Additionally, by definition $\langle \widehat{u} \rangle \equiv 0$, so that the ZZM fields cannot support non-zero circulation along the walls.

2.2.1 Incorporating Circulation

In order to permit non-zero circulation, consider a further decomposition, this time applied to the zonally-averaged fields.

$$q = \widehat{q} + \underbrace{\overline{q} + \ddot{q}}_{:=\langle q \rangle}; \quad \psi = \widehat{\psi} + \underbrace{\overline{\psi} + \ddot{\psi}}_{:=\langle \psi \rangle}; \quad u = \widehat{u} + \underbrace{\overline{u} + \ddot{u}}_{:=\langle u \rangle}; \quad v = \widehat{v} + \underbrace{\overline{v} + \ddot{v}}_{:=\langle v \rangle}, \tag{2.2.1}$$

where $\overline{\psi}$ (ψ-bar) satisfies Neumann BCs (DCTs) and $\ddot{\psi}$ (ψ-laut) produces non-zero circulation. Further, let u_S and u_N denote the mean zonal velocity along the south and north walls respectively and assume a zonally-periodic channel. The circulation is then given by

$$C = \int_0^{L_x} u|_{\text{south wall}} - u|_{\text{north wall}}\, dx = L_x \left(u_S - u_N\right), \tag{2.2.2}$$

since the circulation along the eastern and western 'walls' cancel out by periodicity. An evolution equation for the circulation can then be derived by applying the circulation calculation to equation (2.1.1), yielding

$$\frac{\partial}{\partial t} C = \int_{L_x}^{0} \mathcal{F}_{m,x}|_{y=L_y}\, dx + \int_0^{L_x} \mathcal{F}_{m,x}|_{y=0}\, dx, \tag{2.2.3}$$

where again the east and west 'wall' integral terms cancel by periodicity. In the absence of forcing and dissipation the global circulation is conserved. Otherwise, the evolution is governed by a boundary-integral of the forcing and dissipation terms. Since the circulation along each wall is independent, the circulation evolution can be restricted to each boundary to give separate equations for u_S and u_N (Fierl, 1977).

$$\frac{\partial}{\partial t} u_S = \left.\langle \mathcal{F}_{m,x} \rangle\right|_{y=0} \tag{2.2.4}$$

$$\frac{\partial}{\partial t} u_N = \left.\langle \mathcal{F}_{m,x} \rangle\right|_{y=L_y}. \tag{2.2.5}$$

Now define a forcing field $\ddot{\mathcal{F}}_{m,x}$ that serves as the zonal momentum forcing component for $\ddot{u}$. There are four conditions that are imposed on $\ddot{\mathcal{F}}_{m,x}$. The south- and north-wall circulations must be fully contained in $\ddot{u}$, and $\ddot{\mathcal{F}}_{m,x}$ must incorporate the second derivative components of $\langle \mathcal{F} \rangle$ to satisfy the DST conditions. It will be assumed that higher derivatives vanish naturally. Combined, the conditions can be expressed as:

$$\left.\ddot{\mathcal{F}}_{m,x}\right|_{y=0} = \frac{\partial}{\partial t} u_S \tag{2.2.6}$$

$$\left.\ddot{\mathcal{F}}_{m,x}\right|_{y=L_y} = \frac{\partial}{\partial t} u_N, \tag{2.2.7}$$

$$\left.\frac{\partial^2}{\partial y^2} \ddot{\mathcal{F}}_{m,x}\right|_{y=0} = \left\langle \frac{\partial^2}{\partial y^2} \mathcal{F}_{m,x} \right\rangle (y=0), \tag{2.2.8}$$

$$\left.\frac{\partial^2}{\partial y^2} \ddot{\mathcal{F}}_{m,x}\right|_{(y=L_y} = \left\langle \frac{\partial^2}{\partial y^2} \mathcal{F}_{m,x} \right\rangle (y=L_y), \tag{2.2.9}$$

and they can be satisfied with the cubic polynomial

$$\ddot{\mathcal{F}}_{m,x} = ay^3 + by^2 + cy + d, \tag{2.2.10}$$

where the coefficients a, b, c, and d are functions of time and are given in Appendix A.5.

For notational ease, define $\ddot{a} = \int_0^t a d\tau$, with similar definitions for $\ddot{b}$, $\ddot{c}$, and $\ddot{d}$. Since $\frac{\partial}{\partial t}\ddot{u}(y, z, t) = \ddot{\mathcal{F}}_{m,x}$, the corresponding laut fields can be computed via:

$$\begin{aligned} \ddot{u} &= \ddot{a}y^3 + \ddot{b}y^2 + \ddot{c}y + \ddot{d}, && (2.2.11) \\ \ddot{v} &\equiv 0, && (2.2.12) \\ \ddot{\psi} &= -\left(\frac{1}{4}\ddot{a}y^4 + \frac{1}{3}\ddot{b}y^3 + \frac{1}{2}\ddot{c}y^2 + \ddot{d}y\right), \text{ and} && (2.2.13) \\ \ddot{q} &= -\left(3\ddot{a}y^2 + 2\ddot{b}y + c\right) - L_r^{-2}\ddot{\psi}. && (2.2.14) \end{aligned}$$

2.2.1.1 Forcing Limitations

The current implementation imposes some restrictions on the type of forcing functions that can be applied. First, the forcing function must be given analytically for all points in the domain and all times. Second, the forcing is currently restricted to momentum forcing ($\mathcal{F}_m$), and excludes buoyancy forcing ($\mathcal{F}_b$). Buoyancy forcing, which can modify the surface boundary conditions, would be very useful, but is beyond the scope of the current implementation.

Further, $\ddot{\psi}$ was designed to include the second derivative of the momentum forcing field. It is assumed that third derivatives and higher vanish at the boundaries. This is perhaps the largest restriction of the present model, but it is none-the-less a significant extension of previous works (Poulin et al., 2010; Flierl and Pedlosky, 2007), which only allowed spatially uniform forcing. The structure of the forcing fields in the interior of the domain is not restricted, which aligns well with popular QG problems, in which interior forcing is likely the primary focus.

2.2.2 Methodology

The full fields (q, u, v, ψ) are decomposed into three parts: hats $(\hat{\cdot})$, bars $(\bar{\cdot})$, and lauts $(\ddot{\cdot})$. Combined, the bar and laut fields represent the zonal mean and encompass the zonal transport and circulation, while the hat fields incorporate the deviation from the mean and give zonal structure. In the absence of forcing, the laut fields do not evolve.

Dimensionally, the hat fields are functions of $(x, y[, z])$, and the bar fields of $(y[, z])$, where $[, z]$ denotes optional dependence on the vertical coordinate for three-dimensional simulations. The laut fields are fully specified by two values at each z-level: u_S and u_N.

Step 0: Initialization Suppose that we know all of the hat, bar, and laut fields at a given time. We also suppose that we know the forcing functions. Further suppose that we know u_S, u_N.

Step 1: Evolution equations for PV fields The potential vorticity fields are evolved to the next timestep via the following evolution equations.

$$\frac{\partial}{\partial t}\hat{q} + u\frac{\partial}{\partial x}q + v\frac{\partial}{\partial y}q - \frac{\partial}{\partial y}\left\langle \hat{v}\hat{q}\right\rangle = \begin{cases} \frac{\partial}{\partial x}\mathcal{F}_{m,y} - \frac{\partial}{\partial y}\left(\mathcal{F}_{m,x} - \left\langle \mathcal{F}_{m,x}\right\rangle\right) - \left(\mathcal{F}_b - \left\langle \mathcal{F}_b\right\rangle\right) & \text{2D} \\ \frac{1}{\mathrm{Bu}}\frac{\partial}{\partial z}\left(\mathcal{F}_b - \left\langle \mathcal{F}_b\right\rangle\right) + \frac{\partial}{\partial x}\mathcal{F}_{m,y} - \frac{\partial}{\partial y}\left(\mathcal{F}_{m,x} - \left\langle \mathcal{F}_{m,x}\right\rangle\right) & \text{3D} \end{cases} \tag{2.2.15}$$

$$\frac{\partial}{\partial t}\bar{q} + \frac{\partial}{\partial y}\left\langle \hat{v}\hat{q}\right\rangle = \begin{cases} -\left\langle \mathcal{F}_b\right\rangle - \frac{\partial}{\partial y}\left\langle \mathcal{F}_{m,x}\right\rangle - \frac{\partial}{\partial y}\ddot{\mathcal{F}}_{m,x} & \text{2D} \\ \frac{1}{\mathrm{Bu}}\frac{\partial}{\partial z}\left\langle \mathcal{F}_b\right\rangle - \frac{\partial}{\partial y}\left\langle \mathcal{F}_{m,x}\right\rangle - \frac{\partial}{\partial y}\ddot{\mathcal{F}}_{m,x} & \text{3D} \end{cases} \tag{2.2.16}$$

$$\frac{\partial}{\partial t}\ddot{q} = \frac{\partial}{\partial y}\ddot{\mathcal{F}}_{m,x} \tag{2.2.17}$$

Note that summing the three equations returns the evolution equation for the full forced potential vorticity. Further, $\ddot{q}$ is not directly evolved; instead, $\ddot{a}, \ddot{b}$, and $\ddot{c}$ are evolved following equations (A.5.1), (A.5.2), and (A.5.3), from which $\ddot{q}$ is directly computed.

Step 2: Inversions To determine the streamfunctions, two inversions must be performed. The first is a full $(x, y[, z])$ inversion. Since both $\hat{q}$ and $\hat{\psi}$ satisfy zero-Dirichlet conditions in y, DSTs are used for the y-transforms, FFTs are used for the x-transforms, and, in the case of a three-dimensional simulation, DCTs are used for the z-transforms.

$$\hat{q} = \begin{cases} \left[\frac{\partial^2}{\partial x^2} + \frac{\partial^2}{\partial y^2} - L_r^{-2}\right]\hat{\psi} & \text{2D} \\ \left[\frac{\partial^2}{\partial x^2} + \frac{\partial^2}{\partial y^2} + \frac{f^2}{N^2}\frac{\partial^2}{\partial z^2}\right]\hat{\psi} & \text{3D} \end{cases} \tag{2.2.18}$$

Since the bar terms have no zonal dependence, the next inversion is only performed in $(y[, z])$, and so is significantly cheaper. Since both $\bar{q}$ and $\bar{\psi}$ satisfy zero-Neumann conditions in y, DCTs are used for both the y- and z-transforms.

$$\bar{q} = \begin{cases} \left[\frac{\partial^2}{\partial y^2} - L_r^{-2}\right]\bar{\psi} & \text{2D} \\ \left[\frac{\partial^2}{\partial y^2} + \frac{f^2}{N^2}\frac{\partial^2}{\partial z^2}\right]\bar{\psi} & \text{3D} \end{cases} \tag{2.2.19}$$

Step 3: Computing velocities The velocity components are computed in the usual way, with the exception of the lauts, which are again given analytically.

$$\hat{u} = -\frac{\partial}{\partial y}\hat{\psi} \qquad \bar{u} = -\frac{\partial}{\partial y}\bar{\psi} \qquad \ddot{u} = \ddot{a}y^3 + \ddot{b}y^2 + \ddot{c}y + \ddot{d} \tag{2.2.20}$$

$$\hat{v} = \frac{\partial}{\partial x}\hat{\psi} \qquad \bar{v} = 0 \qquad \ddot{v} = 0 \tag{2.2.21}$$

$$\tag{2.2.22}$$

Step 4/0: Reconstruct full fields The full fields can be reconstructed by combining the respective hat, bar, and laut components. There is now sufficient information to proceed to the next time-step.

2.3 Implementation

Many of the specific implementation details are inherited from the full SPINS model and can be reviewed in Subich et al. (2013). A brief summary of the method is provided, with more attention given to the diagnostics and additional features that were part of the *SPIQG* project and not in the original SPINS implementation. The model is parallelized using OpenMPI and uses spectral transforms to compute spatial derivatives. An adaptive third-order Adams-Bashforth scheme is applied to discretize the time derivatives.

The *SPIQG* model includes two options for computing the flux term, $\frac{\partial}{\partial t}q$. The first is the standard non-linear flux calculator and uses the ZZM and ZI decomposition. The second is the linear flux calculator, which allows the user to specify a background state to determine the linear evolution of the perturbation fields. By using the linear flux option, the user is able to use *SPIQG* to compute linear stability characteristics of three-dimensional systems.

2.3.1 Spectral Diagnostics

If the primary purpose of using spectral methods is spectral accuracy, then an auxiliary benefit is that the implementation provides almost immediate access to spectral representations of the physical fields. As the spectral diagnostics are a contribution from the *SPIQG* project, their purpose and implementations are discussed here.

When the flag for spectral diagnostics is set, the simulation outputs include: three one-dimensional power spectra (k_x-dependent, k_y-dependent, and azimuthally integrated) for kinetic energy, potential energy, and enstrophy; as well as a global and wavenumber-dependent metric of anisotropy.

2.3.1.1 Power Spectra

As mentioned, by stint of using a spectral method the machinery to transform the physical fields into spectral space is already in place. All that remains to provide spectral diagnostics is some careful book-keeping. There are two primary impediments to the spectral analysis. First, in the case of a channel, u and v use different meridional transforms, and so care needs to be taken to align the wavenumber vectors. Second, the ZZM-ZI decomposition of $u = \hat{u} + \overline{u}$ means that within u both DCTs and DSTs are needed[1]. Note that, by construction, the laut fields do not satisfy spectral transforms, and so only hat and bar fields are considered here. As a result, the spectra are only accurate if the laut fields are not significant.

The solution to the second impediment comes from Parceval's theorem and the linearity of analytic Fourier, cosine, and sine transforms. In particular, if $\mathcal{T}\left[u\right] = \mathcal{U}$ represents the transformed velocity field, then

$$\iint_{\Omega} u^2 dA = \sum_{\vec{k}} \left| \mathcal{T}\left[u\right](\vec{k}) \right|^2 = \sum_{\vec{k}} \left| \mathcal{T}\left[\hat{u}\right](\vec{k}) + \mathcal{T}\left[\overline{u}\right](\vec{k}) \right|^2 . \tag{2.3.1}$$

That is, the ZZM and ZI components of u can be transformed separately and re-combined in spectral space. Again, care must be taken in the case of a channel to combine cosine and sine transformed fields appropriately. However, since $\overline{u}$ has no zonal dependence, its transformed field is only non-zero for $k_x = 0$. In contrast, since $\hat{u}$ has zero-zonal mean, it is necessarily zero for $k_x = 0$, so the spectra are disjoint by construction. This removes any concern regarding phase when adding separate sine and cosine series in spectral space.

Once the spectra of u and v are computed, it is possible to compute the azimuthally-integrated spectra (Waite and Bartello, 2004). That is, integrate the power spectrum over horizontal wavenumbers of the same magnitude to return a power spectrum that depends only on a generic horizontal wavenumber k_h instead of the horizontal wavenumber vector $\vec{k}$. This is performed by simply binning the spectra using concentric cylindrical shells. Specifically, given a power spectrum $P(\vec{k}, z)$, the integrated power spectrum $P_I(k_h, z)$ can be computed as

$$P_I(k_h, z) = \sum_{\left|\vec{k}\right| \in k_h \pm \Delta k} P(\vec{k}, z). \tag{2.3.2}$$

---

[1] Recall that $\hat{u}$ is the ZZM component of u, not the FFT/DCT/DST representation of u.

By construction, the laut-fields do not satisfy any of the conditions for DFTs, DCTs, or DSTs. As a result, the spectral diagnostics are only valid in simulations without significant circulation.

2.3.1.2 Anisotropy

Having computed the azimuthally integrated power spectra, it is now possible to provide metrics of anisotropy. These metrics are discussed in greater depth in chapter 3, but a brief outline is provided here. Broadly speaking, a system is said to be isotropic if there's no preferred orientation for physical features and anisotropic otherwise (p. 89 of Davidson, 2004). Let $P(k_x, k_y, z)$ represent the power spectrum as a function of the two horizontal wavenumbers k_x and k_y and the depth coordinate z. Further, let $P_I(k_h, z)$ represent the integrated power spectrum as a function of k_h, the horizontal wavenumber, and z, the vertical coordinate. Define the isotropy metric $\Theta(k_h)$, a function of horizontal wavenumber:

$$\Theta(k_h) = \frac{||P - P_I||_2}{||P||_2 + ||P_I||_2} \quad = \frac{1}{N_z} \sum_z \frac{\sqrt{\sum_{|\vec{k}|=k_h} \left[P\left(k_x, k_y, z\right) - P_I\left(k_h, z\right)\right]^2}}{\sqrt{\sum_{|\vec{k}|=k_h} P\left(k_x, k_y, z\right)^2} + \sqrt{\sum_{|\vec{k}|=k_h} P_I\left(k_h, z\right)^2}}. \tag{2.3.3}$$

That is, $\Theta(k_h)$ is the norm of the difference between P and P_I over each wavenumber band, normalized by the triangle inequality so that $\Theta(k_h) \in [0, 1]$, and depth-averaged. This choice provides a metric that will necessarily identify variations of power within a wavenumber band, since the azimuthally integrated spectrum, P_I, is free of such variations by construction. The properties of this metric will be further explored in chapter 3.

A global measure of anisotropy can be found by taking the norm of the difference between P and P_I over the entire spectral domain. However, because of the nature of the spectral domain, there are more points in a large wavenumber band, $k_{\text{large}} \pm \Delta k$, than a small wavenumber band, $k_{\text{small}} \pm \Delta k$, for $k_{\text{large}} > k_{\text{small}}$. This will bias the global anisotropy metric towards the small-scale anisotropy. In order to account for this, the spectra are scaled by k_h, making the global isotropy metric:

$$\Theta = \frac{\left|\left|\frac{P}{k_h} - \frac{P_I}{k_h}\right|\right|}{\left|\left|\frac{P}{k_h}\right|\right| + \left|\left|\frac{P_I}{k_h}\right|\right|} \tag{2.3.4}$$

2.4 Demonstrations and Sample Cases

The following subsections each present a specific test case that is used to demonstrate various features of the presented quasi-geostrophic model. Section 2.4.1 presents a two-dimensional turbulence simulation that is used to demonstrate the anisotropy metrics. Section 2.4.2 demonstrates the interior forcing functionality with a case in which eastward flow is constantly forced over a small region. Section 2.4.3 then considers the destabilization of a traditional two-dimensional (barotropic) jet. The instability process is compared between a case with a very large across-jet domain and a case with a heavily restricted across-jet extent. Chapter 4 applies the *SPIQG* model to study the stability and non-linear evolution of interior vortices. Section 2.4.5 then forces shear flow with non-zero circulation to demonstrate the capacity for evolving circulation.

2.4.1 Two-Dimensional Turbulence

A classical validation case for a quasi-geostrophic model is two-dimensional turbulence. This sample case is used to demonstrate the anisotropy metric discussed in section 2.3.1.2. Starting with a noisy field under an f-plane assumption, an inverse cascade will cause energy to transfer to larger and larger scales until the system is dominated by two large vortices of opposing polarity (section 8.3 of Vallis, 2006). In contrast, under a β-plane assumption, the meridional variation in the Coriolis parameter constrains the meridional length scales, causing the formation of zonal jets through mean zonal transport at each latitude (Rhines, 1975). Figure 2.1 presents the temporal evolution of the zonally averaged potential vorticity for both turbulence cases. The f-plane case shows a general increase in scales, but not strongly coherent features, such as the alternating bands of vorticity that develop in the β-plane case. Both simulations start with identical initial conditions so that their initial anisotropies agree. In either case, a channel geometry is dynamically comparable to a doubly-periodic geometry since the dominant characteristics are vortex mergers and zonal advection.

Figure 2.2 compares the wavenumber-dependent kinetic energy isotropy metric for the f-plane (upper panel) and β-plane (lower panel) cases. The horizontal yellow and magenta lines indicate the filter and Rhines scales respectively. The f-plane simulation shows no significant development of anisotropy. In contrast, the β-plane simulation shows significant anisotropization at scales larger then the Rhines scale corresponding to the formation of zonal jets. The potential energy and enstrophy anisotropy metrics show similar behaviour.

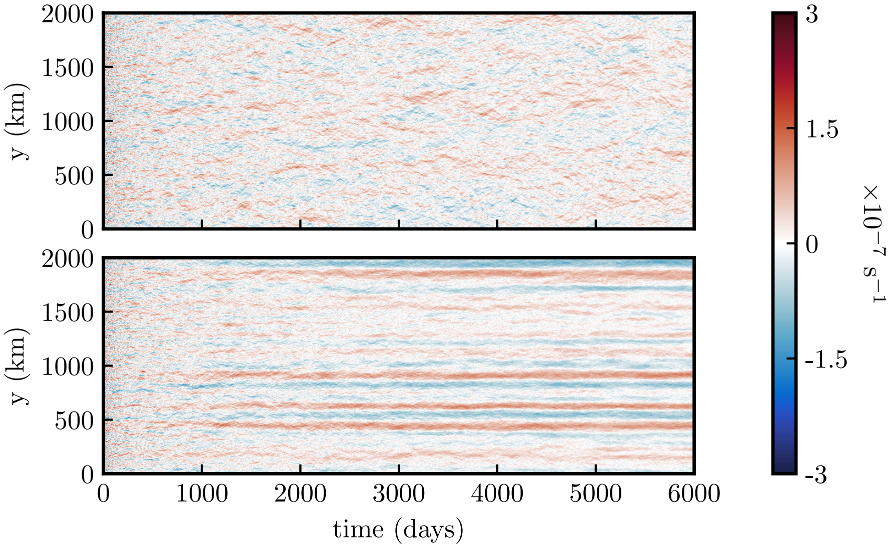

Figure 2.1: Zonal mean potential vorticity for f-plane (upper) and β-plane (lower). Horizontal axis is time and vertical axis is meridional coordinate. (cf. Figure 9.5 of Vallis, 2006)

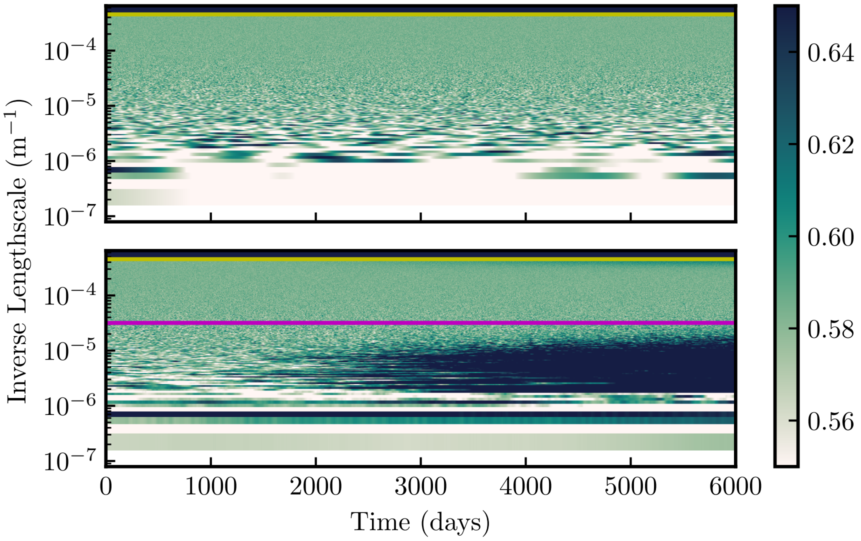

Figure 2.2: Comparison of the wavenumber-dependent KE anisotropy metric for f-plane (upper) and β-plane (lower) turbulence. Recall that larger values indicate higher anisotropy. The yellow and magenta horizontal lines indicate the filter cut-off and Rhines scale respectively.

2.4.2 Interior Forcing

This example forces eastward flow in a small region to illustrate the forcing functionality by driving a zonal jet/dipole structure under Rayleigh damping. The zonal momentum forcing and corresponding terms for the evolution equations are given by equations (2.4.1) - (2.4.4). The parameters are $r = (200\,\mathrm{day})^{-1}$, $L = 10\,\mathrm{km}$, and $u_* = 5r$.

$$\mathcal{F}_{m,x} = u_* \exp\left(-(y/L)^2 - (x/L)^2\right) - ru \tag{2.4.1}$$

$$\frac{\partial}{\partial y}\mathcal{F}_{m,x} = -u_* \frac{2y}{L^2} \exp\left(-(y/L)^2 - (x/L)^2\right) - r\frac{\partial}{\partial y}\left(\hat{u} + \bar{u} + \ddot{u}\right) \tag{2.4.2}$$

$$\frac{\partial}{\partial y}\left\langle \mathcal{F}_{m,x}\right\rangle = -u_* \frac{2y}{L^2}\frac{\sqrt{\pi}L}{L_x} \operatorname{erf}\left(\frac{L_x}{2L}\right) \exp\left(-(y/L)^2\right) - r\frac{\partial}{\partial y}\left(\bar{u} + \ddot{u}\right) \tag{2.4.3}$$

$$\frac{\partial}{\partial y}\ddot{\mathcal{F}}_{m,x} = 0 \tag{2.4.4}$$

Figure 2.3 shows the potential vorticity q of the simulation at four selected times. The forcing generates an eastward propagating dipole which leaves a jet-like structure in its wake. Additional dipoles are generated in the forcing region and are advected along by the jet-like tail of the leading dipole. These trailing dipoles result in the pulsing pattern throughout the jet. Eventually, the leading dipole enters the forcing region, closing, and eventually destabilizing, the jet (not shown). The vertical dashed lines correspond to the subsets chosen for figure 2.4. Figure 2.4 focuses on the leading dipole structure for times corresponding to the upper three panels of Figure 2.3. These subsets show the complex evolution as the dipole continues to twist, thinning the vorticity bands as time advances. Eventually, a secondary dipole advects into the aft of the main dipole, destabilizing the structure and causing more complex features to form.

2.4.3 Constrained Barotropic Jet

This example further demonstrates the channel configuration by considering the evolution of a barotropic jet (Flierl et al., 1987), given by equation (2.4.5), under two different geometric constraints. The jet has a width of 28.8 km ($L = 14.4$km) and vanishes identically on $|y| \geq L$. It is also important to note that the initial conditions vanish smoothly and so are appropriate for a spectral method. In the first case the channel is 80 km wide, while in the second case the channel is 30 km wide, which leaves only 600m between the jet edge and the channel walls. For both cases, the channel length and initial velocities are 150 km and 8cm/s respectively. The 80km case used an 8192×4096 numerical grid, while the

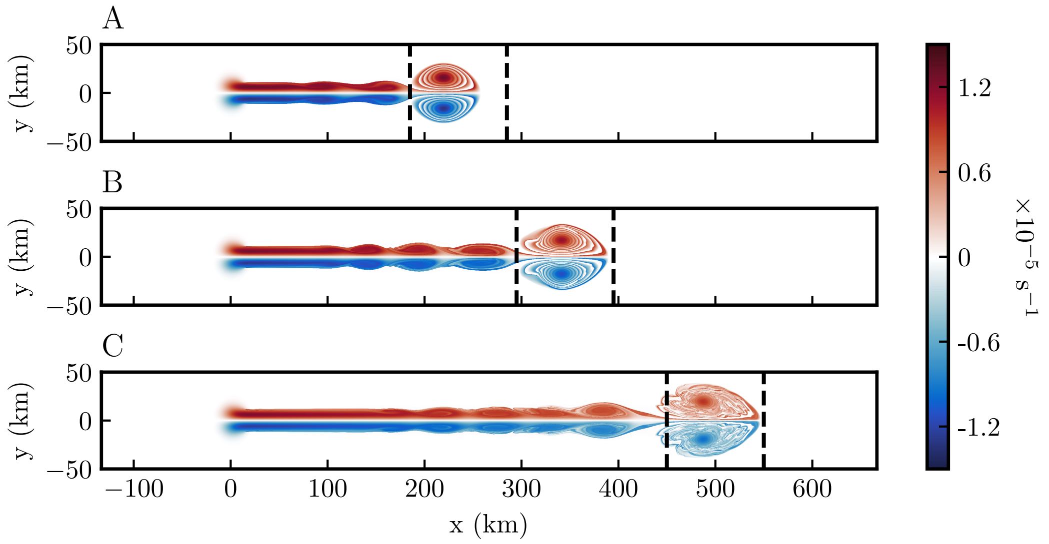

Figure 2.3: Potential vorticity q of the forced simulation at A) 75 days, B) 114 days, and C) 165 days. Dashed lines indicate the subsets chosen for figure 2.4. Horizontal and vertical axes are the zonal and meridional coordinate in km. Note that the full meridional domain extends to $[-100\text{km}, 100\text{km}]$.

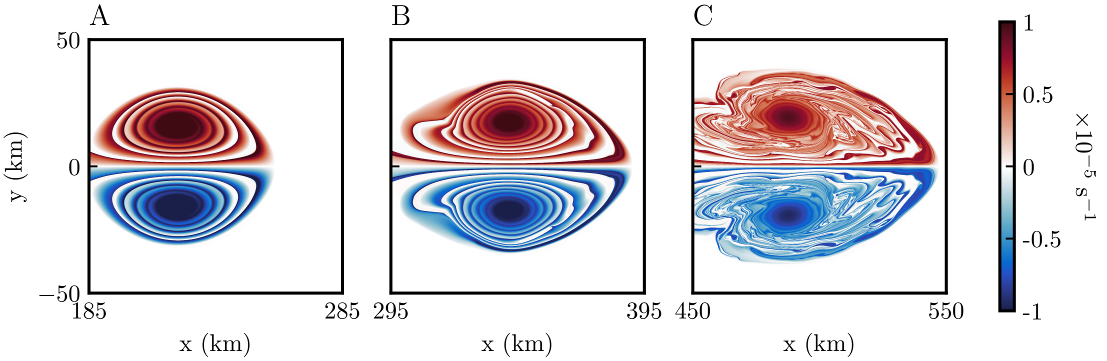

Figure 2.4: Plots focusing on the leading dipole in the first three frames of Figure 2.3. Horizontal and vertical axes are the zonal and meridional coordinate in km. Note that the full meridional domain extends to $[-100\text{km}, 100\text{km}]$.

30km case used an 8192 × 2048 numerical grid.

$$u = \begin{cases} U_0 \exp\left(1 - \frac{1}{1-(y/L)^2}\right) & |y| < L \\ 0 & |y| \geq L \end{cases} \tag{2.4.5}$$

Since equation (2.4.5) defines a positive semi-definite eastward velocity, the system demonstrates non-trivial net eastward transport. As a result, the streamfunction changes value across the jet, which would produce a discontinuity in a doubly-periodic setting. While the use of a double-jet, which adds a counter-propagating jet sufficiently far away so as to avoid interaction, removes the net-transport problem, it is computationally inefficient and not feasible for geometrically constrained systems. The addition of walls along the north and south ends of the domain removes the need for counter-propagating jets, thereby permitting the simulation to have a much more constrained across-jet extent.

Figure 2.5 shows the potential vorticity q at three times for the two simulations: 80 km domain (left column) and the 30 km domain (right column). Note that the figures respect the true aspect ratio of the simulations. These simulations begin highly anisotropic and isotropize through the instability mechanism. However, while the 80km case undergoes strong isotropization as the jet breaks down into vortical features, the 30km case retains strong anisotropies because of the inhibited vortex generation.

As discussed, *SPIQG* has options to produce many diagnostics during the simulation, thereby providing very high temporal resolution, if desired. This simulation, for example, produced 100 full outputs but 10,000 diagnostic outputs. One of these options is to measure the deviation from a specified reference state. In this example, the reference state is the background jet profile. At each time-step, the 2-norm of the perturbation in q is computed and recorded in an output file. These are presented in blue in figure 2.6 for the two cases. Using low order finite differencing, the derivative, or growth rate, is then computed and presented in orange. These diagnostics reveal that the constrained geometry reduces the growth rate by roughly 40%.

2.4.4 Interior Vortices

Storer et al. (2018) (chapter 4 of this thesis) uses the *SPIQG* model to simulate the nonlinear evolution of large-scale interior vortices. In their application, the spectral diagnostics provided a means of diagnosing the generation of small-scale energy. Further, since the power spectra can be generated with very high temporal resolution, they could reasonably compute temporal derivatives of the power spectra to compute the time rate of change of power at each wavenumber, which provided a tool for diagnosing the instability mechanisms in their simulations.

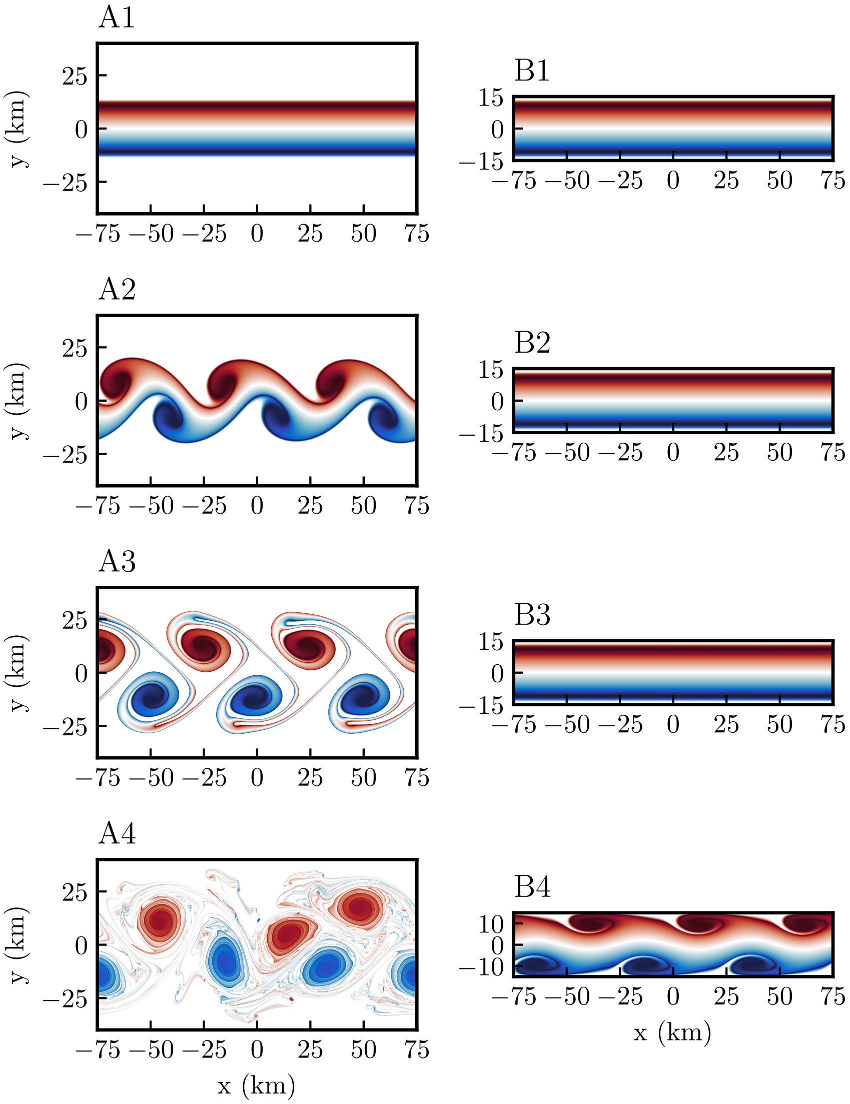

Figure 2.5: Plots of the potential vorticity q for the 80km channel (left) and 30km channel (right). First row: initial condition. Second row: 216 days. Third row: 250 days. Fourth row: 350 days. The aspect ratio is accurate and kept consistent across all frames.

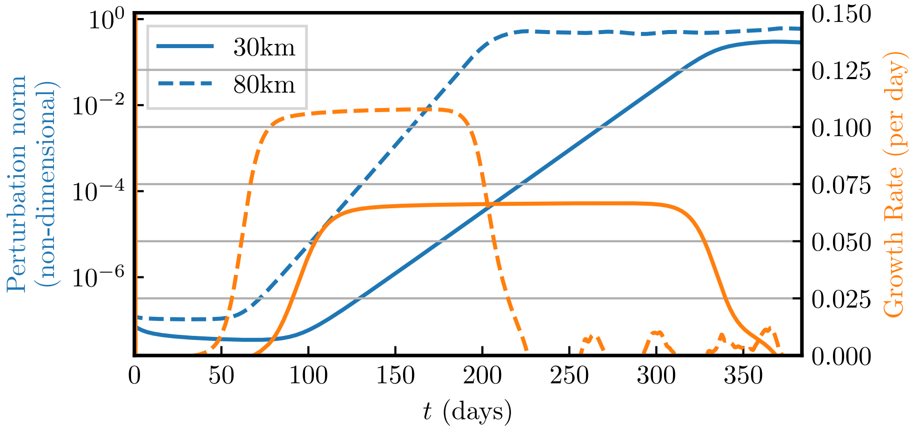

Figure 2.6: Comparison of the growth rates (right axis, orange lines) and perturbation norms (left axis, blue lines) for the constrained case (30km, solid lines) and large domain case (80km, dashed lines).

2.4.5 Forced Shear Flow

This demonstration forces shear flow through the domain using a tanh profile (see equation (2.4.6)) so that non-zero velocity is forced along the walls and a non-zero net transport is established. The forcing parameters are $u_N^* = -0.08$ m/day, $u_S^* = 0.02$ m/day, $L_h = 10$ km, $t_{\text{cut}} = 10$ day, and $t_{\text{width}} = 5$ day. Note that this simulation is undamped and that the forcing is gradually turned off so that there is essentially no forcing after 20 simulation days. The simulation is seeded with Gaussian white noise in order to facilitate destabilization. Figure 2.7 presents the zonal and time-zonal averages of u, q, and ψ. The early stage of the simulation (approximately first 30 days) sees the establishment of the shear flow with weak eastward flow in the south and strong westward flow in the north. Beyond this time, the perturbation has extracted sufficient energy from the shear flow to destabilize the flow. The time- and zonally- averaged streamfunction demonstrates both non-zero Neumann and Dirichlet conditions at each wall. By definition, $\left\langle \widehat{\psi} \right\rangle = 0$, so this must be a combination of $\overline{\psi}$ and $\ddot{\psi}$. The former satisfies zero Dirichlet conditions, and so the non-zero slope at the boundaries must arise from the latter. The circulation along each wall grows according to the proscribed boundary velocities given in equation (2.4.6).

$$\ddot{\mathcal{F}}_{m,x} = \left(\frac{(u_N^* - u_S^*)}{2} \left(1 + \tanh\left(\frac{y}{L_h}\right)\right) + u_S^* \right) \cdot \frac{1}{2} \left(1 - \tanh\left(\frac{t - t_{\text{cut}}}{t_{\text{width}}}\right)\right) \tag{2.4.6}$$

Up until the onset of the instability at approximately 30 days, the mean velocity field agrees very well with the form of the forcing field.

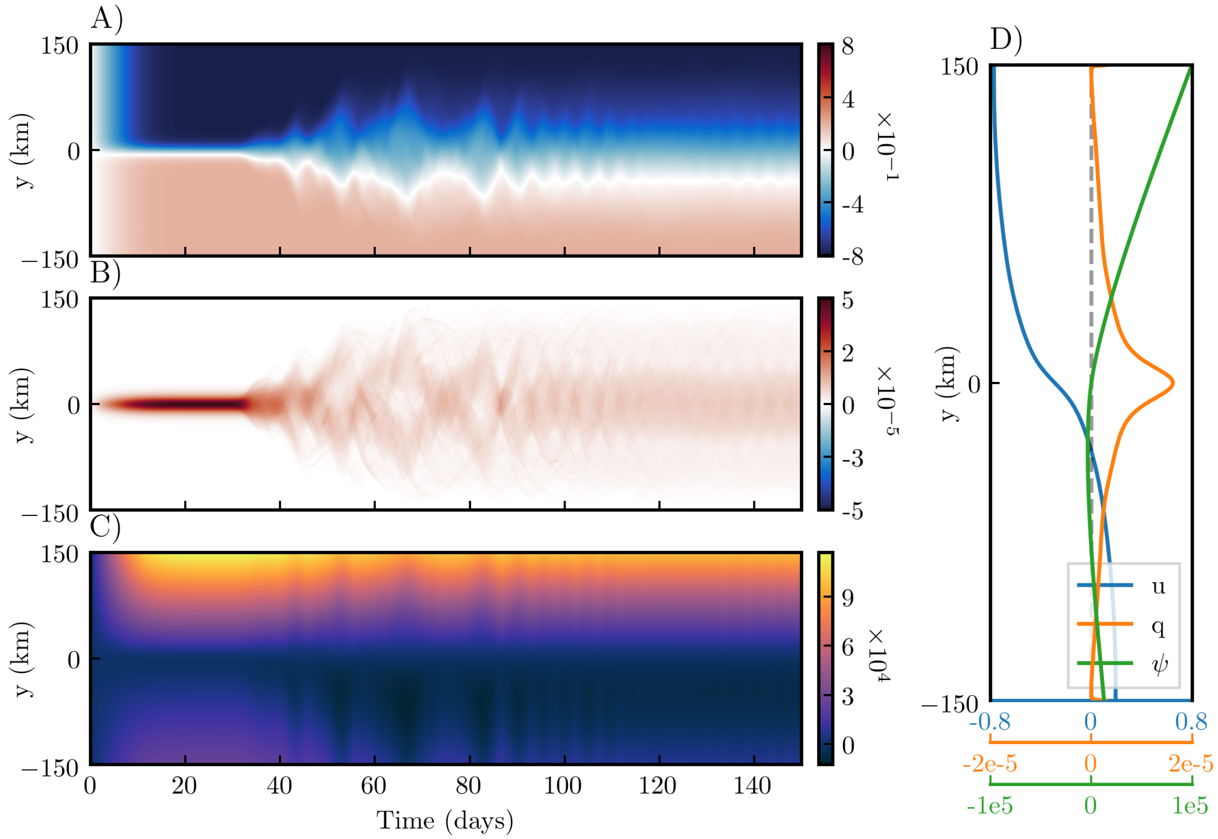

Figure 2.7: Panels A) - C) respectively show the temporal evolution of $\langle u \rangle$, $\langle q \rangle$, and $\langle \psi \rangle$. D) Time-averaged $\langle u \rangle$ (blue), $\langle q \rangle$ (orange), and $\langle \psi \rangle$ (green).

2.5 Conclusions

By implementing a decomposition into zonal mean and deviations therefrom, it is possible to formulate a spectral method for simulating quasi-geostrophic systems in channel geometries. As a result, the method is able to maintain spectral accuracy, avoid grid clustering, allow the formation and evolution of zonal mean flow, as well as permitting the evolution of circulation, provided that an appropriate forcing field is supplied.

Several cases were used to present the various strengths and features of the model. The first case, 2.4.1, a traditional two-dimensional turbulence problem, is used as a demonstration of validation as well as the anisotropy diagnostic, which readily identifies the formation of the zonal jets. Cases 2.4.2 and 2.4.5 then present the utility of the forcing feature. The former case applied forcing within the interior of the domain to drive eastward flow, producing a leading dipole that demonstrated intricate structures as the trailing jet advected perturbations into its aft. The latter case generates circulation by driving a shear flow throughout the domain. The initial quasi-steady flow demonstrates a velocity profile matching the specified forcing that gives non-zero circulation along each wall. The shear profile eventually destabilizes, producing a series of vortices which steadily combine, giving a domain-scale vortex that is advected along by the mean flow. Case 2.4.3 then compared the evolution of a barotropic jet in the case of a large and a constrained domain, in which it was seen that the growth rate of the dominant instability is reduced by approximately 40%. Chapter 4 then applies the *SPIQG* model to study the non-linear evolution of three-dimensional vortices.

In each of cases 2.4.2, 2.4.3, and 2.4.5, the ability to use channel geometry played an important role. In the jet cases, a doubly periodic setting would require using a double jet to avoid a non-periodic streamfunction, which can be costly and, in the constrained geometry case, inconsistent with the desired set-up. Similarly, the wall forcing case would otherwise require a periodic forcing function as well as a doubled domain, both of which are mitigated by the use of a channel geometry.

2.6 Summary of Features

- Based on the powerful SPINS model (Subich et al., 2013).
    - Parallelized using MPI
    - Third-order Adams-Bashforth scheme for temporal discretization with adaptive time-stepping
    - Spectral accuracy for spatial derivatives

  - Spectral filter maintains stability of the system by removing energy from small scales

- Accurately handles channel geometries to evolve mean zonal flow
- Solve both the one-layer and three-dimensional quasi-geostrophic equations
- Built-in diagnostics, which can be output at a different frequency than full fields, allowing high temporal resolution
  - perturbation norms, if a reference field is provided at run-time, which can then yield perturbation growth rates
  - domain-integrated kinetic energy, potential energy, and enstrophy
  - x, y, and azimuthally-integrated spectra of kinetic energy, potential energy, and enstrophy
  - global and wavenumber-dependent anisotropy metrics for kinetic energy, potential energy, and enstrophy
  - computation diagnostics, including Δt, clock-time per simulation step, and the ratio of simulation time to clock time
- Python drivers for initializing simulations provides a user-friendly interface and avoids the need to repeatedly re-compile the program
- Python package for reading and post-processing results

2.6.1 Summary of Limitations

- Number of processors cannot exceed Nx or Ny.
- Spectral diagnostics do not apply in the case of circulation-enducing forcing.
- Can only use rectangular geometries.
- The x and z boundary conditions are limits to being periodic and free-slip respectively. The y boundary conditions can be either periodic or free-slip.

Chapter 3

Spectral Quantification of Anisotropy

Consider the horizontal kinetic energy density of a system, given by $\mathrm{KE} = \rho_0\,(u^2+v^2)$, where u and v denote the westward and northward velocities respectively and ρ_0 is the reference density. By merit of Parseval's theorem, it is not only possible to compute the total kinetic energy from the Fourier components, but it is also possible to compute the kinetic energy within a wavenumber band. Doing so is common practice in many fields of fluid dynamics, and the result is termed the kinetic energy power spectrum (p. 492-494 of Press et al., 1986).

Computing the power spectrum of a two-dimensional (x, y) field produces a two-dimensional (k_x, k_y) spectrum, where k_x and k_y denote the wavenumbers corresponding to the x and y dimensions, respectively. Since visualizing datasets is easier with fewer dimensions, there are common practices for reducing the two-dimensional spectrum into a one-dimensional spectrum, the validity of which will depend on the context of the data. One option is to simply produce k_x and k_y spectra separately by integrating out the dependence on the undesired dimension. Another common option is to azimuthally integrate the power spectra by creating concentric rings in spectral space, $(i \pm 0.5) \cdot \Delta k_h, i \in \mathbb{Z}_N$, where now k_h refers to a generic horizontal wavenumber (e. g. Waite and Bartello, 2004). By applying Parseval's theorem over the concentric rings, the two-dimensional horizontal power spectrum can be reduced to a generic horizontal power spectrum.

However, both of these reduction techniques lose important information. In particular, comparing k_x and k_y spectra can misrepresent features that are not aligned along the coordinate axes. Meanwhile, the azimuthally integrated spectrum accounts for all features of a given length scale, but provides no information regarding whether or not features of a particular length scale have a preferred orientation, or the extent to which power at a given lengthscale varies with orientation. Comparing the three spectra can provide some insight, but does not directly provide a quantification for the extent to which length scales have a preferred orientation. While the full two-dimensional spectrum does provide this information, visualizing the full spectrum across a time-series is non-trivial and, moreover, also does not immediately quantify preferential orientations.

In fluid dynamics, preferred orientations for length scales is often called *anisotropy* (p. 89 of Davidson, 2004). A system is called *isotropic* if it does not distinguish between different directions and *anisotropic* otherwise. This chapter proposes spectrally-computed metrics of anisotropy. In particular, a global metric and wavenumber-dependent metric are presented, which quantify the over-all anisotropy as well as the anisotropy for each length scale. It is important to note that the presented metrics do not give information about which orientations are preferred, but simply seeks to determine to what extent there is a preferential bias.

Waite and Bartello (2004) qualitatively diagnoses anisotropy by observing the structure of power contours in spectral space. This methodology can provide length-scale dependent information, but is necessarily limited in temporal resolution, since it requires the investigator to manually inspect and compare the spectra.

Lumley (1979) presents the normalized anisotropy tensor b_{ij} and two invariants η and ζ, which are given by

$$b_{ij} = \frac{\langle u_i u_j \rangle}{\langle u_k u_k \rangle} - \frac{1}{3}\delta_{ij}, \qquad \eta = \left(\frac{1}{6} b_{ij} b_{ji}\right)^{1/2}, \text{ and } \qquad \zeta = \left(\frac{1}{6} b_{ij} b_{jk} b_{ki}\right)^{1/3}. \tag{3.0.1}$$

These metrics provide information about the structure of the flow through the Lumley triangle (p. 138 of Lumley, 1979), ($\zeta - \eta$ version in Pope (p. 395 of 2000)). For example, $\zeta = \eta = 0$ implies isotropy, while $\zeta = \eta = 1/3$ implies ostensibly one-dimensional flow. In the case of two-dimensional simulations, the invariants collapse to the upper edge of the Lumley triangle so that the Lumley anisotropy could be represented by a single value. However, these metrics do not provide information on length-scale dependent anisotropy. Moreover, computing them requires a known reference state about which perturbations can be extracted, or more specifically that the Reynolds stress tensor can be produced. While this may generally be true of turbulence simulations, it need not be true of fluid simulations in general.

Wyngaard (p. 326 of 2010) uses the skewness S and flatness (or kurtosis) F factors to propose a criterion for local anisotropy: $|S| \ll (F + 1)/2$, where S and F are the third and fourth moments of the velocity field. Thoroddsen and Van Atta (1992) uses ratios of the mean-square strain rates of the various velocity components as a measurement of anisotropy. In the isotropic limit, the expected ratio is 2, and so significant deviation therefrom would indicate anisotropy.

McWilliams et al. (1994) uses directionally-weighted decompositions of the power spectra in order to measure anisotropy. This metric is hereafter referred to as the McWilliams metric. For a wavenumber κ, they define the anisotropy $A(\kappa)$ as

$$A(\kappa) = \frac{3S_{z'}(\kappa)}{S(\kappa)}, \tag{3.0.2}$$

where $z' = (N/f)z$, N is the buoyancy frequency, f is the Coriolis frequency,

$$S(\kappa) = \int_{|\mathbf{k}|=\kappa} |\widehat{q}(\mathbf{k})|^2 \, \mathrm{d}\mathbf{k}, \text{ and} \qquad S_{z'}(\kappa) = \int_{|\mathbf{k}|=\kappa} \left(\frac{\kappa_{z'}}{\kappa}\right) |\widehat{q}(\mathbf{k})|^2 \, \mathrm{d}\mathbf{k}. \tag{3.0.3}$$

That is, $S(\kappa)$ integrates specral power over spherical shells, while $S_{z'}(\kappa)$ first directionally-weights the spectra to emphasize vertical scales before integrating over spherical shells. This method provides wavenumber-dependent anisotropy information. A two-dimensional $x - y$ variation can be easily obtained by instead writing

$$A(\kappa) = \frac{2S_x(\kappa)}{S(\kappa)}, \tag{3.0.4}$$

where S_x is defined analagously to $S_{z'}$. As will be seen, this metric is closely related to the presented metric. However, this metric is limited in that if given a spectrum that is symmetric about $k_x = k_y$, it would identify such a system as being isotropic. A physical interpretation of this is that the McWilliams et al. (1994) metric is unable to detect diagonal anisotropies, such as NE-SW bands, but rather optimally detects anisotropies that are aligned with the coordinate axes.

3.1 Proposed Quantification

Again consider kinetic energy density, given by $\mathrm{KE} = \rho_0 \left(u^2 + v^2\right)$, and let $\widehat{u}$ and $\widehat{v}$ represent the spectral representation of u and v respectively. For periodic domains, $\widehat{u}$ and $\widehat{v}$ are obtained through discrete Fourier transforms. For non-periodic domains, discrete sine and cosine transforms can be used, although care must be taken during implementation to handle the wavenumber vectors and scaling factors appropriately.

Let $\Theta(k_h)$ and Θ represent the wavenumber-dependent and global anisotropy metrics respectively. These terms will be defined in the proceeding sections by equations (3.1.1) and (3.1.3). Let $P(\mathbf{k})$ denote the spectral power density and $P_I(k_h)$ denote that azimuthally averaged spectral power density, where $\mathbf{k} = (k_x, k_y)$ and $k_h = |\mathbf{k}|$.

Figure 3.1 provides a graphical illustration of some of the steps of the anisotropy calculation applied to a sample of noise that was constructed to obey a $k_h^{-3/4}$ power law. In each panel, only one quadrant is shown to avoid clutter. The first panel shows a sample spectral power density, $P(\mathbf{k})$, with the concentric black rings indicating the bins over which azimuthal averaging will be performed. The second panel, B, shows the result of the azimuthally averaged power spectrum, P_I. The third panel then shows the normalized difference between panels A and B: $(P - P_I)/\,|P_I|$, a proxy for the contribution to the numerator of the anisotropy metric. The following sections will outline how these components are combined to form the proposed wavenumber-dependent and global metrics of anisotropy.

3.1.1 Lengthscale-dependent Anisotropy

The wavenumber dependent anisotropy is defined as

$$\Theta(k_h) = \frac{||P - P_I||_2}{||P||_2 + ||P_I||_2}. \tag{3.1.1}$$

That is, for each concentric ring in spectral space, anisotropy is defined as the 2-norm of the difference between the full power spectrum and the azimuthally integrated power spectrum, normalized using the triangle inequality. Since the triangle inequality provides an upper bound for the norm of a difference, we are guaranteed that $0 \leq \Theta(k_h) \leq 1$.

3.1.1.1 Statistical Interpretation

In addition to the mathematical norm-based interpretation, there is a meaningful statistical interpretation of the wavenumber-dependent anisotropy. To see this, first make the following definitions. Let N_{k_h} denote the number of discrete wavenumbers within the concentric ring given by $k_h - \frac{\Delta k}{2} \leq |\mathbf{k}| < k_h + \frac{\Delta k}{2}$. Next, let $p_{k_h,i}$ denote the power at the i^{th} wavenumber in the ring centred on k_h, where the i-ordering is unimportant. We then have that $P_I(k_h)$ is the mean over i of $p_{k_h,i}$, which we can denote as $\overline{p_{k_h}}$. Finally, let $\mu(\cdot)$ and $\sigma(\cdot)$ respectively denote the mean and standard deviation of the set of points indicated by $\cdot$. Using these definitions, and by the definition of the norm, $\Theta(k_h)$ can then be written as

$$\Theta(k_h) = \frac{\sigma\left(p_{k_h,i}\right)}{\sqrt{\mu\left(p_{k_h,i}^2\right)} + \mu\left(p_{k_h,i}\right)} \tag{3.1.2}$$

That is, the anisotropy within a given wavenumber ring is the standard deviation of power within that ring, divided by the sum of the mean power and the root-mean-squared power. While the standard deviation alone provides a metric for anisotropy, the choice of denominator ensures that $\Theta(k_h) \leq 1$, providing a meaningful non-dimensionalization.

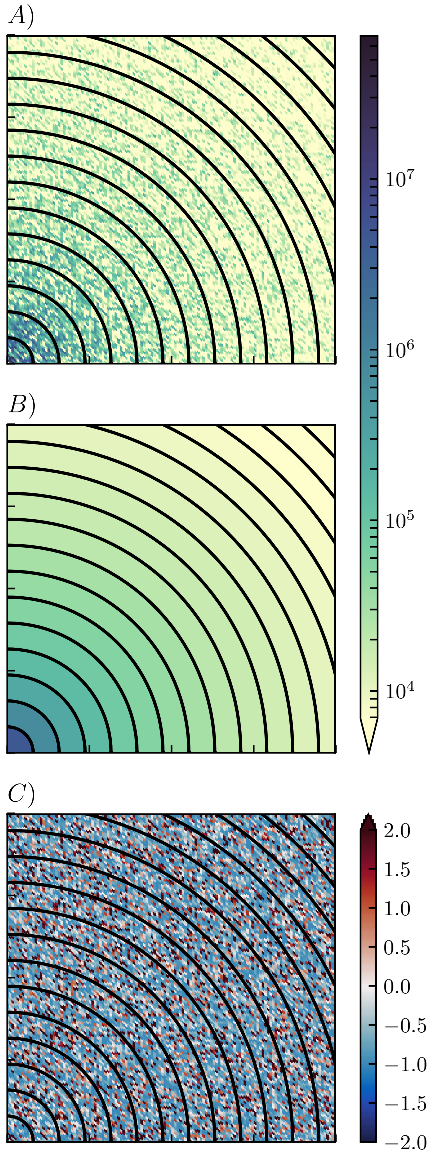

Figure 3.1: Each panel shows a two-dimensional spectral-space plot of a component used to compute anisotropy. The horizontal axis is k_x and the vertical axis is k_y. In each panel only one quadrant is shown to avoid clutter. The black lines illustrate spectral bands, which are significantly wider than are used in the metric. **A)** Power spectrum (P) of red noise with sample concentric rings overlain. **B)** Power spectrum averaged over each ring (P_I). **C)** Visualization of the local contributions to the anisotropy metric: $(P - P_I) \cdot |P_I|^{-1}$.

3.1.2 Global Metric

The global anisotropy metric provides a single scalar value that describes the over-all anisotropy of a field. In contrast to the wavenumber-dependent metric, the global metric considers all wavenumbers simultaneously. However, by the nature of spectral domains, for $k_{\text{large}} > k_{\text{small}}$ there are more wavenumbers in $k_{\text{large}} \pm \Delta k$ than in $k_{\text{small}} \pm \Delta k$, and so simply extending the norms in equation (3.1.1) would bias the metric in favour of the small-scale anisotropy. In order to counter the bias, and noting that the number of points in the band $k_h \pm \Delta k$ scales linearly with k_h, the contribution from each wavenumber is scaled by k_h. That is, the global anisotropy metric is defined as

$$\Theta = \frac{\left|\left|\frac{P-P_I}{k_h}\right|\right|_2}{\left|\left|\frac{P}{k_h}\right|\right|_2 + \left|\left|\frac{P_I}{k_h}\right|\right|_2}. \tag{3.1.3}$$

The same norm-based interpretation applies, but the wavenumber de-biasing means that the statistical interpretation from the wavenumber-dependent metric cannot be applied in this case.

3.1.3 Extension to Three-Dimensional Fields

There are many ways to extend the presented metric to three-dimensional fields. Three particular extensions of interested are discussed here. The first, and perhaps most canonical, is to use spherical shells when decomposing the spectral domain. This extension provides an over-all anisotropy metric that would be of interest in three-dimensional turbulence settings. Depending on the context of the problem, it may be appropriate to first scale the dimensions. For example, since McWilliams et al. (1994) considers a stratified quasi-geostrophic setting (Vallis, 2006), they scale the vertical coordinate by f_0/N_0, where f_0 and N_0 are the constant Coriolis and buoyancy frequencies.

The second approach is to simply depth-integrate to remove the dependence on the vertical coordinate. However, it is important to note that depth integration must be applied *after* computing the anisotropy, and not beforehand. Depth integrating a helical structure, for example, would yield an isotropic field, while the helical structure itself is anisotropic. This method provides a quantification of horizontal anisotropy while incorporating depth, which would be of use in predominantly two-dimensional systems. Indeed, omitting the depth-integration step would provide depth and wavenumber-dependent anisotropy information.

Finally, the two horizontal dimensions can be reduced down to a single horizontal dimension by integrating through k_x, k_y. Applying the metric to the resulting k_h, k_z spectrum would then provide a metric for quantifying the distinction between vertical and horizontal scales. This extension would be of most use in cases where there's no significant horizontal anisotropy, and distinctions between the vertical and horizontal are sought.

The choice of extension should be motivated by the physical understanding of the specific problem and context in consideration; which directions are most relevant and what underlying structures are present.

3.1.4 Limitations

The proposed quantification for anisotropy relies heavily on the ability to transform the appropriate field into spectral space. Moreover, there is an underlying connection to Parseval's theorem, and so the presented diagnostics is not applicable for non-quadratic fields, such as the cubic kinetic energy that arises in the shallow water model (p. 139 of Vallis, 2006).

Additionally, as will be seen with the demonstration in section 3.3, it may be necessary to compute the reference anisotropy for different physical contexts in order to determine the statistical significance of the observed anisotropies.

3.2 Anisotropy of Noise

In the context of physical systems, noise is ubiquitous in each of observation, experimentation, and simulation. It is then important to ask if an observed behaviour is significant, or if it is simply an artefact of the underlying noise. As regards anisotropy, it is necessary to understand the anisotropy inherent in noise fields, so that by comparison, it can be determined if the diagnosed field is more or less isotropic that a noisy field, or if the observed features are simply statistical manifestations of noise.

If the mean and standard deviation of anisotropy for a reference noise field are determined, then they would provide a statistically sound means of determining when the (an)isotropy of a system differs significantly from that of noise.

3.2.1 Theoretical Results

In the implementation considered in this chapter, the concentric wavenumber rings are taken to have width $\Delta k = \frac{2\pi}{L}$, so that along the principal axes there is exactly one wavenumber within each ring. For the reference noisy state, consider Gaussian white noise. That is, sampled from a normal distribution with mean of 0 and standard deviation of 1 and in which spatial points are uncorrelated. The real and complex components of the Fourier transform of such a field would themselves then be Gaussian random variables. As a result, the magnitude of the Fourier components would follow a Rayleigh distribution (equivalently a χ-distribution with two degrees of freedom) (Papoulis, 1965), with the spectral power of each velocity component then following an exponential distribution. For multi-component fields, such as velocity, it would be necessary to add multiple such exponential distributions to obtain the full power. Accordingly, the sum of n exponential distributions follows a Gamma distribution with shape parameter n.

Using the statistical interpretation of $\Theta(k_h)$ in equation (3.1.2), the wavenumber-dependent anisotropy can found by substituting the corresponding statistics for the Gamma distribution. Namely, for shape and rate parameters α and β, the mean, standard-deviation and root-mean-square of a Gamma-distributed random variable are: α/β, $\sqrt{\alpha}/\beta$, and $\sqrt{\alpha(\alpha+1)}/\beta$ respectively. Combining these, and recalling that the shape parameter is n, gives that the wavenumber-dependent anisotropy for white noise can be computed as

$$\Theta(k_h) = \frac{1}{\sqrt{n}+\sqrt{n+1}}. \tag{3.2.1}$$

That is, for a single component (i.e. scalar) field, such as enstrophy, the anticipated white-noise anisotropy would be $\left(1+\sqrt{2}\right)^{-1} \approx 0.414$. For a two-component field, such as the KE of horizontal velocity, the anticipated white-noise anisotropy would be $\left(\sqrt{2}+\sqrt{3}\right)^{-1} \approx 0.318$. For a three-component field, the anticipated white-noise anisotropy would be $\left(\sqrt{3}+\sqrt{4}\right)^{-1} \approx 0.268$. Unfortunately, determining the standard deviation of the wavenumber-dependent anisotropy is less trivial, and will instead be found empirically.

Similar analytic results were not found for the global anisotropy metric. The wavenumber weighting in equation (3.1.3) confounds such analytics, so results for global anisotropy are only found numerically.

3.2.2 Numerical Results

In order to produce statistically meaningful results, the anisotropy metrics for one-, two-, and three-component fields were computed for 10^5 random fields generated on a 2048×2048 computational domain. The results were obtained using the scipy.fftpack library in Python and parallelized with mpi4py.

Figure 3.2 presents the results of applying the anisotropy calculations to the noise fields. In each panel, blue corresponds to one-component, orange to two-components, and green to three-components. Panel A shows the wavenumber-dependent anisotropy, with the horizontal axis giving normalized wavenumber and the vertical axis the anisotropy.

The blue, orange, and green lines indicate the mean value anisotropy values, while the pale envelopes show one standard deviation. Panel B, which shares a vertical axis with the panel A, gives the corresponding distribution of the global anisotropy. In each of panels A and B, the horizontal black lines indicate the theoretical value of $(1+\sqrt{2})^{-1}$ (solid), $(\sqrt{2}+\sqrt{3})^{-1}$ (dashed), and $(\sqrt{3}+\sqrt{4})^{-1}$ (dash-dotted). Panel C shows the standard deviation of the wavenumber-dependent anisotropy (width of the envelopes in panel A). The corresponding fits from regression are provided in the figure legend and shown by the dashed lines.

3.2.3 Determining Statistical Significance

Panel A of figure 3.2 reveals that the wavenumber-dependent anisotropy quickly converges to the corresponding anticipated value. Features that are large relative to the domain are represented with few wavenumbers, and so it is not surprising that they demonstrate poor statistical agreement. Combined with the high correlation coefficients of the fits to the standard deviation, this suggests that a simple z-statistic for significance of anisotropy can be found via

$$z = \frac{\Theta(k_h) - \left(\sqrt{n} + \sqrt{n+1}\right)^{-1}}{\sigma_n(k_h)}, \tag{3.2.2}$$

where

$$\sigma_n(k_h) = \begin{cases} 10^{-0.85}(k_h/k_{\min})^{-0.48}; & n=1 \\ 10^{-0.93}(k_h/k_{\min})^{-0.49}; & n=2 \\ 10^{-1.0}(k_h/k_{\min})^{-0.49}; & n=3 \end{cases} \tag{3.2.3}$$

is the standard deviation at wavenumber k_h, $k_{\min}$ is the smallest non-zero wavenumber, $\Theta(k_h)$ is the computed anisotropy at wavenumber k_h, and n is the number of components. The standard deviation is directly related to the number of samples within each spectral ring, which is consistent between the three cases, which in turn explains the consistency between the slope coefficients. Standard z-score tables can then be used to choose the cut-off criterion for significance. For the purposes of the demonstration in this chapter, $|z| > 2$ is considered significant.

3.3 Sample Application

This section provides a demonstration of the anisotropy metric applied to a numerical simulation of quasi-geostrophic turbulence (p. 673-676 of Kundu and Cohen, 2008). Broadly speaking, there are two dynamical regimes that are of interest. The first, f-plane turbulence, is dynamically isotropic and has no inherent orientation preference. Energy simply

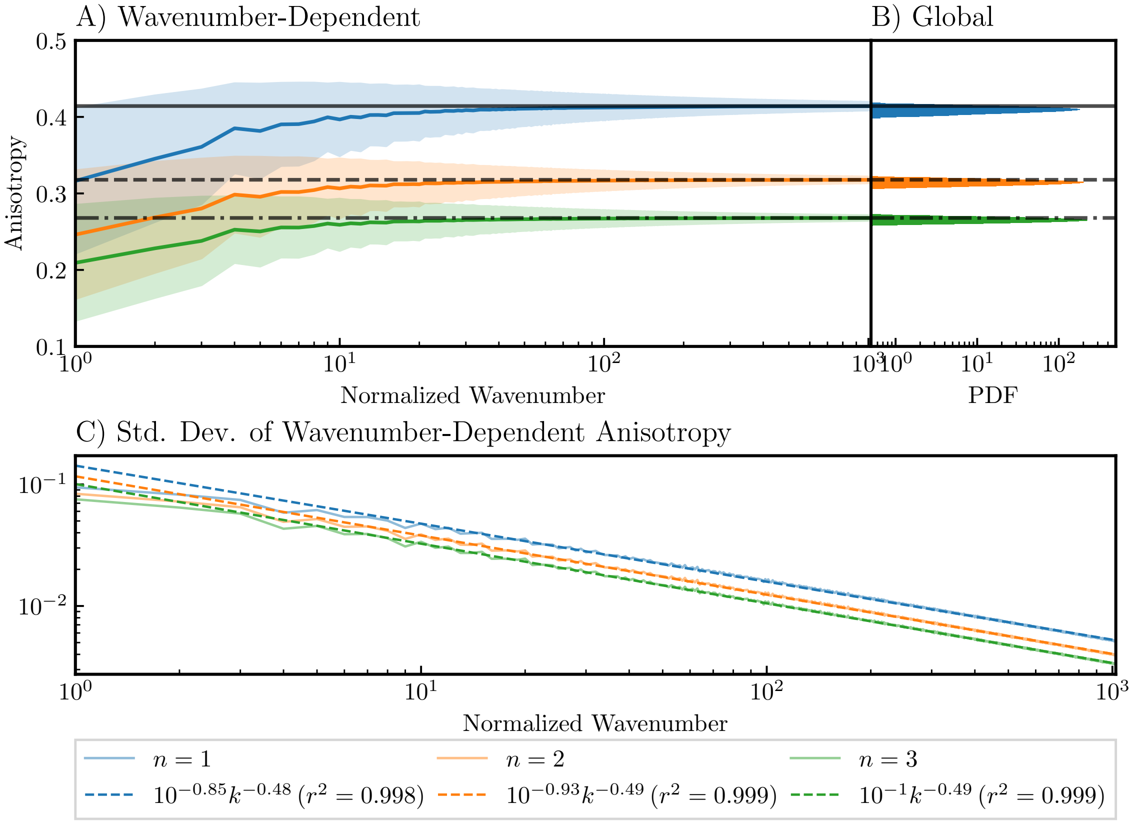

Figure 3.2: Anisotropy diagnostics for one- ($n = 1$, blue), two- ($n = 2$, orange), and three- ($n = 3$, green) component white noise fields. **A)** wavenumber-dependent anisotropy. Dark lines indicates mean anisotropy, while pale envelopes denote one standard deviation. The horizontal black lines indicate the theoretical mean value: $\left(\sqrt{n} + \sqrt{n+1}\right)^{-1}$. **B)** probability density of the global anisotropy metric for each component count. **C)** Standard deviation of the wavenumber-dependent anisotropy (solid lines) and fit (dashed lines).

transfers from small scales to large scales through vortex merging until the system is dominated by domain-scale vortices. The second, β-plane turbulence, is inherently anisotropic, since variation in the Coriolis parameter now distinguishes east-west motions from north-south motions. In this case, zonally (east-west) consistent features, called β-jets, form with a meridional (north-south) length-scale given by the Rhines scale (Rhines, 1975).

The specific dynamics are not important for our current considerations, only that, given the same initial conditions, the f-plane system would be nominally isotropic, while the β-plane system develops anisotropic features, the length-scale of which can be estimated a priori. In each simulation, the computational grid was 8192×8192, domain scales were $L_x = L_y = 6,300$ km, the deformation radius was set to 10^6 km, the initial root-mean-squared speed was 0.01 m/s, and the β-plane case used $\beta = 10^{-11}$.

3.3.1 Comparison with Reference Gaussian Noise

Figure 3.3 outlines the anisotropy metrics if the f-plane simulation using the same layout as figure 3.2. It is interesting to note that the mean wavenumber-dependent anisotropy is significantly higher, converging to approximately 0.5832 instead of $(\sqrt{2} + \sqrt{3})^{-1} \approx 0.318$. This suggests that the appropriate z-statistic for these cases is:

$$z = \frac{\Theta(k_h) - 0.5833}{\sigma(k_h)}, \tag{3.3.1}$$

where $\sigma(k_h) = 10^{-0.91}(k_h/k_{\min})^{-0.48}$. The discrepancy between Gaussian noise and f-plane turbulence highlights the importance of determining the appropriate reference anisotropy for the context in consideration; the underlying structures and physics of the one does not apply to the other, and so it would be inappropriate to apply the Gaussian noise statistics to a geostrophic turbulence problem. Obtaining the appropriate reference anisotropy for a case can likely be obtained by studying the relevant turbulence problem.

3.3.2 Anisotropy Results

The upper row of figure 3.4 presents the wavenumber-dependent anisotropy for the f-plane (left panel) and β-plane (right panel) simulations. The f-plane case demonstrates little to no temporal evolution in the anisotropy while, contrastingly, the β-plane developes considerable anisotropization at length-scales exceeding the Rhines scale. z-score significance testing, as in equation (3.3.1), is shown in the bottom row of figure 3.4, with z scores exceeding 2 (i.e. deviation greater than two standard deviations) coloured yellow for significant anisotropy and red for significant isotropy. It can be readily seen that the β-plane anisotropy is indeed statistically significant when compared with the reference f-plane statistics.

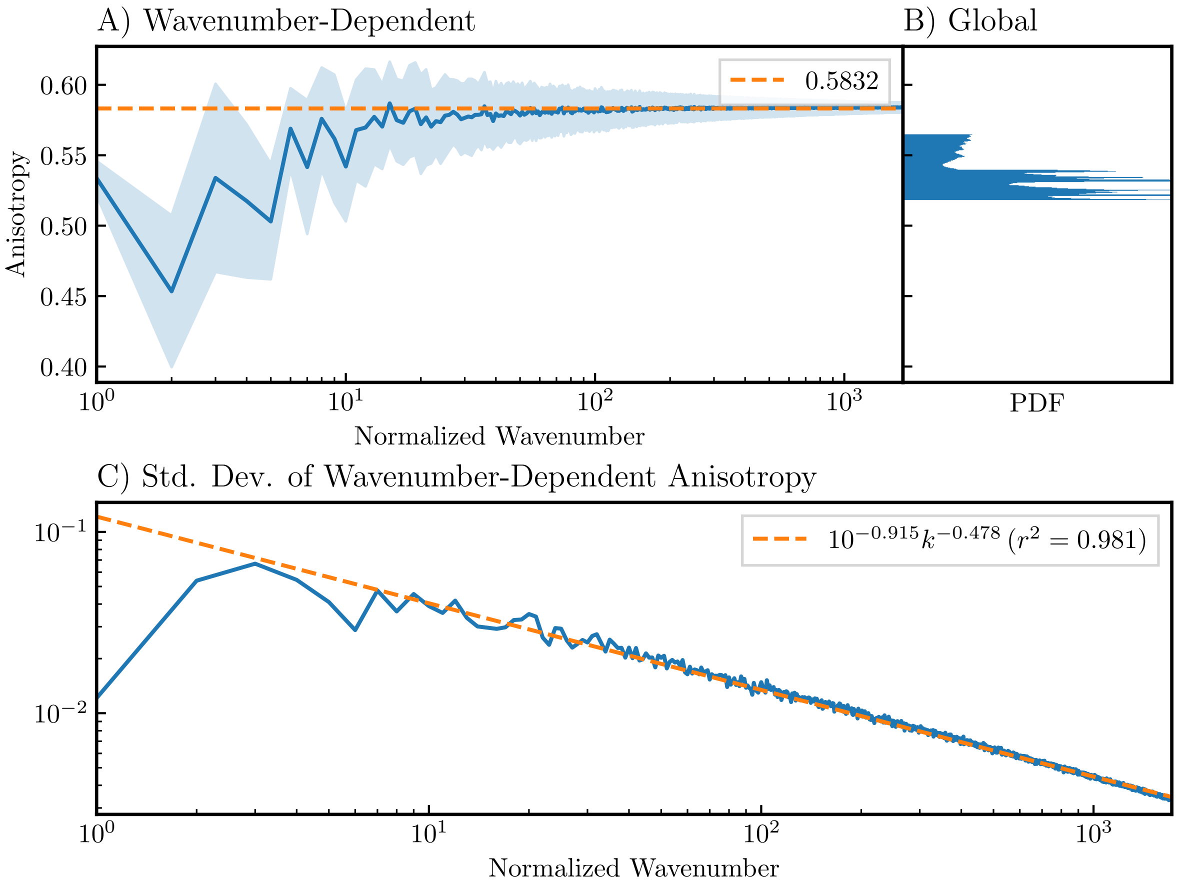

Figure 3.3: Anisotropy diagnostics for f-plane turbulence. Structure follows Figure 3.2. **A)** wavenumber-dependent anisotropy (independent of colour). Dark blue line indicates mean, light blue envelope denotes one standard deviation. **B)** probability density of the global anisotropy metric for each colour of noise. **C)** Standard deviation of the wavenumber-dependent anisotropy (solid blue) and fit (dashed orange).

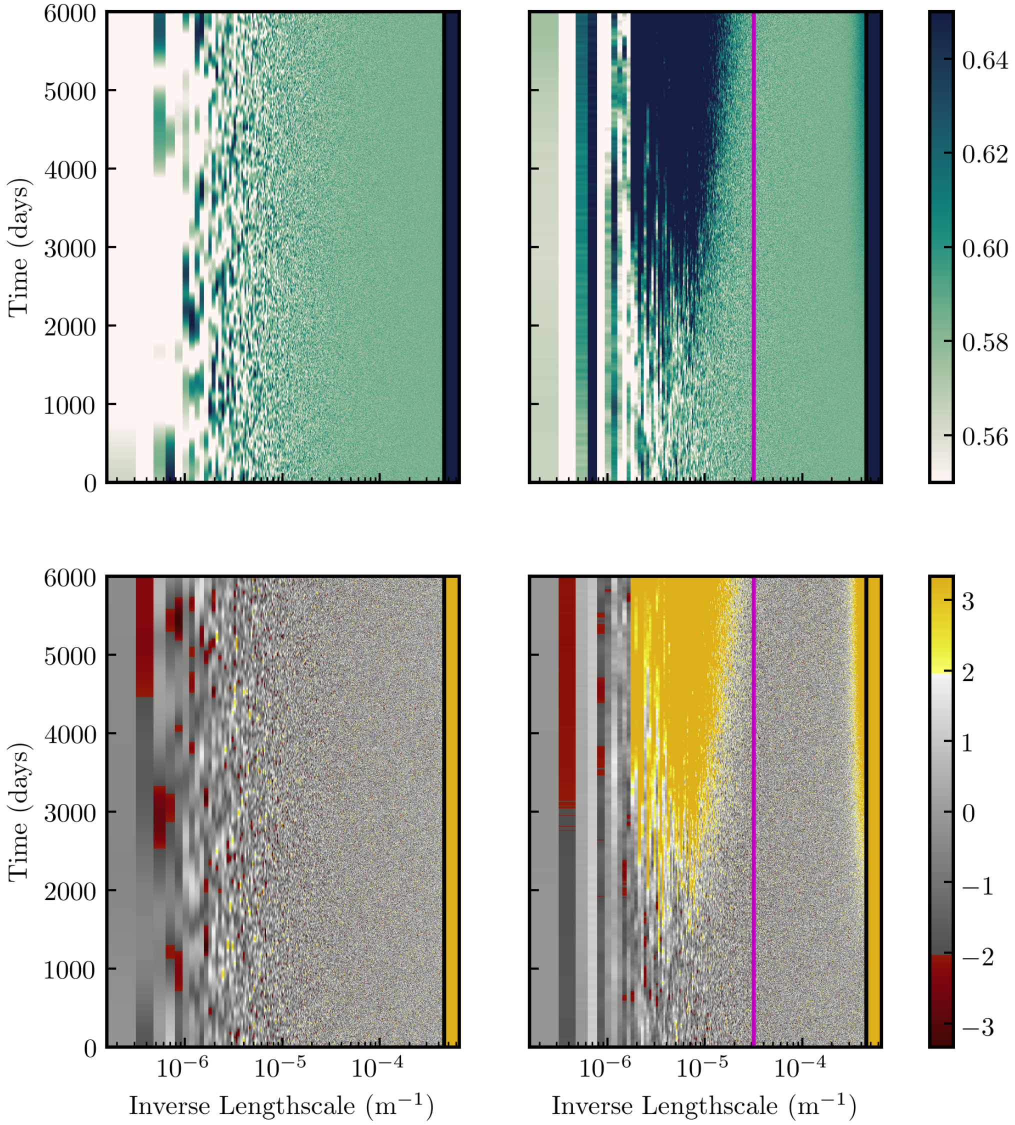

Figure 3.4: Local anisotropy for f-plane (left) and β-plane (right) QG turbulence. Top row: wavenumber dependent anisotropy metric. Bottom row: z-score of the wavenumber dependent metric computed with equation (3.3.1). Yellow (red) regions are significantly more (less) anisotropic than a statistical f-plane ($|z| > 2$). In each panel, the horizontal axis is inverse length-scale and the vertical axis is time. The vertical magenta lines indicate the Rhines scale.

3.3.3 Comparison with McWilliams Method

Recall that in the β-plane setting the predominant feature is the formation of zonal (east-west) jets. These features are not only a source of anisotropy, but they are also aligned along the coordinate axes. As a result, the McWilliams metric accurately identifies the wavenumber-dependent anisotropy and returns very similar features to figure 3.4.

However, as mentioned, the McWilliams metric does not see anisotropies that are symmetric about $k_x = k_y$. To highlight this, consider the case of a double jet centred on $y = -x$. Both the presented metric and McWilliams metric are presented in figure 3.5. This system begins with strong anisotropy but quickly isotropizes as the jet destabilizes. The presented metric captures this and shows isotropization across all scales, while the McWilliams metric shows the system to be initially isotropic and to anisotropize through the instability.

3.4 Summary and Discussion

This chapter presents a spectrally-defined method to quantify the spatial (an)isotropy of physical fields. Since the algorithm relies heavily on spectral transforms and implicitly on Parseval's theorem, the proposed diagnostic can only be applied to fields for which Parseval's theorem holds. The diagnostics provides both a global metric of anisotropy as well as a wavenumber-dependent metric which indicates the extent of anisotropy at each length-scale. A statistical interpretation of the wavenumber-dependent formulation reveals that the metric reduces to weighting the standard deviation of power in order to produce a $[0, 1]$ metric.

As mentioned, an anisotropy value in the abstract is essentially without meaning: that is, it is necessary to have a defined reference state to which comparison can be made. In order to determine such a reference state, the presented diagnostics were applied to a large suite of Gaussian white noise instantiations. This allows a statistical test for significance using a z-score defined by equations (3.2.2) and (3.2.3): giving a means to answer the question: *how anisotropic is anisotropy?*.

As a demonstration, the anisotropy diagnostics were applied to simulations of quasi-geostrophic turbulence, which highlighted the development of significant anisotropy above the Rhines scale. However, while the diagnostic is presented in the context of fluid dynamics, it is a sufficiently general diagnostic that can be applied to any physical fields, provided that spectral transforms and Parseval's theorem are applicable.

The f-plane turbulence case demonstrated baseline anisotropy that deviated significantly from that of Gaussian white noise. This deviation shows how the physical context

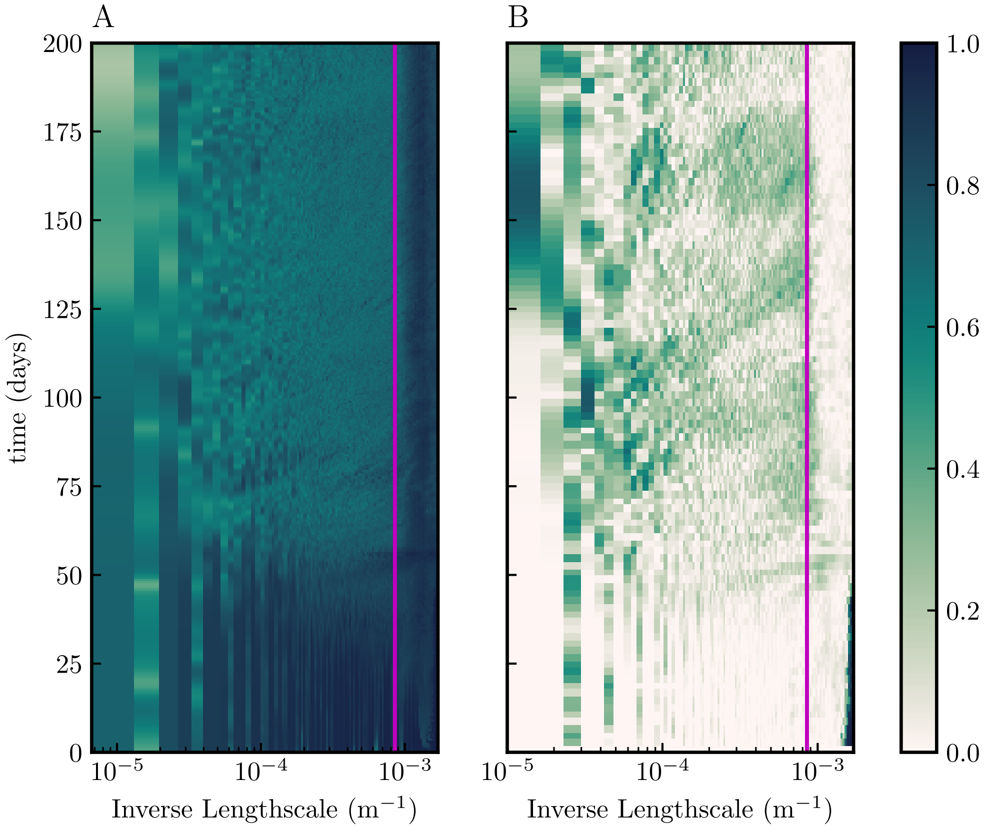

Figure 3.5: Comparison of the presented anisotropy metric (left panel) and the McWilliams et al. (1994) anisotropy metric (right panel) for a double jet aligned along $y = -x$.

sets the reference anisotropy that should be used when determine if a feature is significantly more or less isotropic than noise. Ideally, the baseline would be achieved by considering data from a corresponding isotropic configuration. These baseline statistics can then be applied to the case of interest in order to identify significant (in)coherence.

Chapter 4

Quasi-geostrophic Lens Vortices

The following chapter is a nearly verbatim reproduction of Storer et al. (2018). I was the primary author of the journal article and conducted the majority of the investigation and writing.

The dynamical importance of interior mesos-scale eddies in the oceanic energy budget and transport is well documented in the literature and excellent reviews can be found in McWilliams (1985) and Carton (2001). Examples of deep meso-scale eddies can be found west of the Strait of Gibraltar where a bottom-dwelling current detaches from the floor at a level of neutral buoyancy. The high speeds of this current leads to the formation of vortices, which are both warm and salty since the source water originates from the Mediterranean Sea (Serra et al., 2005; Aiki and Yamagata, 2004). These Mediterranean eddies are predominantly anti-cyclonic in nature and are referred to as Meddies. Other examples of subsurface meso-scale eddies can be found in the Arctic Canadian basin, recently investigated by Zhao and Timmermans (2015), the Red Sea (Reddies) and the Persian Gulf (Peddies), and others (see Ciani, 2016; Ciani et al., 2015, for a review of surface and interior meso-scale lens vortices).

Meddies are long lived features that may collapse on sea mounts or remain coherent and cross the Atlantic ocean (Serra et al., 2002; Serra and Ambar, 2002). Observations estimate the lifespan of Meddies to be approximately one year for those that impact sea mounts and four years otherwise; as many as 29 Meddies can be expected to exist at any given time (Richardson et al., 2000). Prater and Sanford (Figure 19 of 1994) suggests that a reasonable range for mature Meddies is $0.1 < \mathrm{Bu} < 0.5$ and $-0.5 < \mathrm{Ro} < -0.1$, with some observed Meddies falling outside that range. There are relatively few observations of recently-formed Meddies compared to mature Meddies that are found propagating far from the coastlines in the Atlantic ocean. Meddies that are observed over many months are presumably quite stable and would only permit very slowly growing perturbations. The analysis in this chapter goes beyond the Meddy regime and considers a significantly wider parameter range. Moreover, we are looking to qualitatively identify the instabilities, which is why we idealize the Meddy shape into a simplified baroclinic Gaussian lens.

Motivated by the nature of Meddies, Arctic eddies, Reddies and Peddies, we investigate the stability of lens-shaped vortices over a wide range of Burger numbers. Previously, with a focus on Meddies, Nguyen et al. (2012) did a linear stability analysis (LSA) for lens-shaped vortices in the context of the Quasi-Geostrophic (QG) model. They determined that there were different types of instabilities that could occur depending on Bu. Our results focus on the same vortex solution in the QG model and confirm many of their conclusions but also better refine some of their findings, thereby giving us a more accurate picture of the linear stability characteristics of this particular type of vortex. Subsequently, the dynamics of these lens shaped vortices was studied in the non-hydrostatic primitive equations for a wide range of Rossby, Froude (or Burger), and Reynolds numbers, in the context of non-hydrostatic Boussinesq equations (Mahdinia et al., 2016; Yim et al., 2016). They identified many more different types of instabilities that can occur but they focused on the dissipative dynamics and therefore did not quite touch on the regime on which we focus.

It will be shown that in the QG model there are primarily four distinct regions of linear instability in parameter space and they are (where k_θ is the azimuthal wavenumber): *a*) $1 < \mathrm{Bu} < 10$: $k_\theta = 1$ is the only unstable mode, it is associated with vortex tilting, and is not accurately described by the linear theory presented here or in Nguyen et al. (2012), *b*) $\mathrm{Bu} \gg 1$: both $k_\theta = 1, 2$ are unstable, *c*) $0.1 < \mathrm{Bu} < 1$: $k_\theta = 2$ is the only unstable mode, is connected to vortex tearing events, and requires higher resolution than was used in previous results, and *d*) $\mathrm{Bu} < 0.1$: there are many unstable modes, but we note that this is reaching beyond the QG limits.

The chapter is organized as follows. Section 4.1 presents the problem formulation, model equations, and initial conditions that are considered. Section 4.2 discusses the linear stability analysis and compares our results with previous works. Section 4.3 considers two specific fully non-linear three-dimensional simulations and provides an in-depth discussion of the time-evolution. Azimuthal decompositions of the non-linear simulations are presented in subsection 4.3.3. Subsection 4.3.4 considers the energetics and growth-rates for a suite of non-linear simulations. Power spectra and wavelength-dependent rates of change of energy for selected simulations are then discussed in subsection 4.3.5. Conclusions and discussion are in section 4.5.

4.1 Model Equations and Numerical Methods

In this section we present the continuously stratified QG model as well as the equations for the linear stability problem. The details of the numerical methods for both the linear stability calculations and non-linear simulations are provided.

4.1.1 Quasi-Geostrophic Equations

For the QG model to be valid, it is sufficient that the Rossby number and aspect ratio are small and the Burger number is order one (Vallis, 2006, p. 207). In its conservative form, it states that Potential Vorticity (PV) is conserved following the flow (4.1.1), the PV is a sum of the relative vorticity and vertical stretching (4.1.2), and the leading order velocity is in geostrophic balance (4.1.3). The partial symbols denote partial derivatives, q denotes the potential vorticity, $\vec{u}_H$ denotes the horizontal velocity vector, $\vec{\nabla}_H$ is the horizontal gradient operator, $\vec{\nabla}_H^2$ is the horizontal Laplace operator, ψ is the stream-function, $\hat{z}$ is the vertical unit vector, f_0 is the constant Coriolis frequency corresponding to the f-plane assumption, and N_0 is the constant buoyancy frequency.

$$\partial_t q + \vec{u}_H \cdot \vec{\nabla}_H q = 0, \tag{4.1.1}$$

$$q = \left(\vec{\nabla}_H^2 + \frac{f_0^2}{N_0^2} \partial_{zz} \right) \psi, \tag{4.1.2}$$

$$(u, v) = \widehat{z} \times \vec{\nabla} \psi. \tag{4.1.3}$$

4.1.2 Initial Conditions

The physical geometry is chosen to be the rectangular domain given by $x \in [-\frac{1}{2}L_x, \frac{1}{2}L_x]$, $y \in [-\frac{1}{2}L_y, \frac{1}{2}L_y]$, and $z \in [-L_z, 0]$. The lens-shaped vortex has horizontal and vertical length scales of L_h and L_v, respectively. We choose to non-dimensionalize space using these length scales around the center of the vortex, $\left(0, 0, -\frac{1}{2}L_z\right)$:

$$(\widetilde{x}, \widetilde{y}, \widetilde{z}) = \left(\frac{x}{L_h}, \frac{y}{L_h}, \frac{z + \frac{1}{2}L_z}{L_v} \right).$$

We choose the non-dimensional parameter in the QG model to be the Burger number, which can be written as $\mathrm{Bu} = (L_D/L_h)^2$ with a deformation radius of $L_D = N_0 L_v / f_0$. For a particular Bu, one can then determine the corresponding horizontal length scale using $L_h = \frac{N_0 L_v}{f_0 \sqrt{\mathrm{Bu}}}$. While the derivation of the QG model requires a very small Rossby number, since the basic state has a non-zero velocity we can define an associated Rossby number

Parameter	Dimensions	Description	
L_h	m	Horizontal length-scale of the vortex	
L_v	m	Vertical length-scale of the vortex	
N_0	s^{-1}	Buoyancy (Brunt-Väisälä) frequency	
f_0	s^{-1}	Coriolis f-plane parameter	
U_0	m/s	Characteristic velocity of the vortex	
Bu	Dimensionless	Burger number	$= \left(\frac{N_0 L_v}{f_0 L_h}\right)^2$
x, y, z	m	Dimensional Cartesian co-ordinates	
$\widetilde{x}, \widetilde{y}, \widetilde{z}$	Dimensionless	Non-dimensional Cartesian co-ordinate	
q	s^{-1}	Potential vorticity	
ψ	$m^2 s^{-1}$	Stream-function	
Q	s^{-1}	Background potential vorticity	
Ψ	$m^2 s^{-1}$	Background stream-function	
k_θ	Dimensionless	Azimuthal modenumber	

Table 4.1: Description of parameters and notation

and relate them by $U_0 = f_0 L_h Ro$. The dimensional PV in terms of the non-dimensional coordinates is given by

$$q = -\frac{U_0}{L_h}\left(\widetilde{r}^2 - 1 + \frac{1}{\mathrm{Bu}}\left(\widetilde{z}^2 - 0.5\right)\right) e^{(-\widetilde{r}^2 - \widetilde{z}^2)}, \tag{4.1.4}$$

where $\widetilde{r}^2 = \widetilde{x}^2 + \widetilde{y}^2$. Dimensional values that are appropriate for Meddies are $f_0 = 8 \times 10^{-5}\mathrm{s}^{-1}$, $N_0 = \sqrt{5} \times 10^{-3}\mathrm{s}^{-1}$, $U_0 = 0.25\mathrm{ms}^{-1}$, and $L_v = 400\mathrm{m}$ (Hua et al., 2013), corresponding to a deformation radius of $L_d \approx 11\mathrm{km}$. In this investigation we consider $O(1\,\mathrm{km}) \leq L_h \leq O(100\,\mathrm{km})$. A summary of the notation is in Table 4.1, while the parameters used in the non-linear simulations are given in Table 4.2.

4.1.3 Formulation and Numerical Method for Linear Stability Problem

The generalized eigenvalue problem is given by equation (B.0.1), the derivation of which can be found in Appendix B. The spectrum of the generalized eigenvalue problem is computed with an indirect Krylov method implemented using SLEPc. A fourth-order finite difference scheme is used to discretize both the radial and vertical spatial derivatives. In order to speed up convergence on higher resolution grids, seed values were provided from calculations on coarser grids. It is important to note that the linear stability computations

Bu	Nx,Ny,Nz	Lh (m)	Lx,Ly (m)	Lz (m)
0.01	512	111 803.	2 236 070.	4 000
0.03	256	64 549.7	1 290 990.	3 000
0.05	256	50 000.	650 000.	3 000
0.1	256	35 355.3	707 107.	3 000
0.14	512	29 880.7	448 211.	3 000
0.22	256	23 836.6	476 731.	3 000
0.3125	256	20 000.	400 000.	3 000
0.4	256	17 677.7	353 553.	3 000
0.5	256	15 811.4	316 228.	3 000
0.6	256	14 433.8	288 675.	3 000
0.75	256	12 909.9	258 199.	3 000
1.2	256	10 206.2	204 124.	3 000
1.54	256	9 009.37	180 187.	3 000
2.	256	7 905.69	158 114.	3 000
3.	256	6 454.97	129 099.	3 000
4.	256	5 590.17	111 803.	3 000
5.	256	5 000.	100 000.	3 000
7.	256	4 225.77	84 515.4	3 000
10.	256	3 535.53	70 710.7	3 000
15.8489	256	2 808.37	56 167.5	3 000
25.1189	256	2 230.77	44 615.4	3 000
39.8107	256	1 771.96	35 439.3	3 000
63.0957	256	1 407.52	28 150.4	3 000
100.	256	1 118.03	22 360.7	3 000

Table 4.2: Simulation parameters. In each simulation, the following physical parameters are held constant: $f_0 = 0.8 \times 10^{-4}\text{s}^{-1}$, $N_0 = \sqrt{5} \times 10^{-3}\text{s}^{-1}$, and $L_v = 400$ m. Note that the linear stratification corresponds to a total density change of less than 1%. The filter parameters were $\alpha = 20$, $\beta = 2$, and $\kappa_{\text{cut}} = 0.7$, indicating that 70% of the wavenumbers are unchanged.

use cylindrical coordinates centered about the vortex core and are achieved for a given azimuthal modenumber, k_θ. Doing so reduces the problem to two dimensions, greatly simplifying the numerical calculations at the cost of an added boundary condition at $r = 0$.

The boundary conditions at the rigid lid and flat bottom is zero buoyancy, which ensures that there is no vertical velocity through the boundaries. Written in terms of the stream-function, this becomes $\partial_z \psi = 0$ at $z = -L_z, 0$ (Nguyen et al., 2012). As discussed in Baey and Carton (2002), the condition at $r = 0$ is that the pressure anomaly vanishes, $\psi = 0$, for all non-zero azimuthal mode numbers. This can be obtained from Yim (2015) in the QG limit. Furthermore, the stream-function is assumed to vanish in the far-field, yielding $\psi = 0$ at $r = L_r$.

4.1.4 Numerical Method for the Non-linear Dynamics

Non-linear simulations are performed using the SPIQG model (see chapter 2), which uses spectral collocation methods to numerically integrate the three-dimensional, linearly-stratified QG equations. Specifically, the code solves equation (4.1.1) using an adaptive third-order Adams-Bashforth scheme for the time stepping, Fast Fourier Transforms (FFTs) in each horizontal direction and a Discrete Cosine Transform (DCT) in the vertical for the stream-function. The horizontal FFTs correspond to periodic boundary conditions in x and y, while the DCT in the vertical corresponds to rigid-lid and free slip conditions in z. In contrast to the LSA calculations, no conditions are imposed at $r = \sqrt{x^2 + y^2} = 0$. In order to maintain nearly inviscid dynamics, the model equations do not include any viscous terms. To ensure numerical stability, an exponential filter is applied to remove energy from all wavenumbers that exceed a specified cut-off.

4.2 Linear Stability Analysis: Dependence on Bu

To better understand the types of lens vortices that can remain coherent for a long span of time, we begin with linear stability analysis. This analysis is presented here, not as the focus of the study, but to provide context for the non-linear results.

Using the method discussed in section 4.1.3, linear stability calculations are performed over a broad range of Burger numbers, with 250 points distributed logarithmically over $10^{-2} < \mathrm{Bu} < 10$ and 75 points over $10 < \mathrm{Bu} < 10^2$. The results of our calculations will be compared with previous studies of linear stability as well as the growth rates estimated by the fully non-linear simulations presented in this chapter.

Nguyen et al. (2012) found that there were three different ranges of Burger number that yield qualitatively different behaviours. The different stability characteristics in the regimes are well illustrated in their figure 1 (*a*) and (*c*). If Bu $= 1$, for which the vortex scale is equal to the Rossby radius of deformation ($L_h = L_D = N_0 L_v / f_0$), it is shown that the eddy is stable. If Bu $< 1^-$ (Bu $> 1^+$), corresponding to vortices larger (smaller) than the deformation radius, the most unstable wave has a mode two (one) in the azimuthal direction with a symmetric (asymmetric) structure in the vertical. Note that $1^\pm$ are used to denote $1 \pm \delta^\pm$, where $\delta^\pm$ accounts for the possibility of a small but undetermined region of stability around Bu $= 1$. Figure 1 (*c*) in Nguyen et al. (2012) focuses on the regime of very large length scales and shows that there are multiple unstable modes, $k_\theta \in \{1, 2, 3, 4, 5\}$, and that their growth rates are comparable, with $0.03 < \sigma \cdot \frac{4}{Ro} < 0.05$.

We confirm that the linear stability results of Nguyen et al. (2012) are robust using calculations with greater accuracy by making two important changes: we use fourth order discretization as well a spatial resolution of 1024×1024, which is roughly 10 times finer than what they present. In general we find good qualitative agreement in the range of Bu that they considered, although we find that there are four different regions of instability. Through doing a convergence study we determined that the results presented in figure 4.1 are robust; the only exceptions are the growth rates for $k_\theta = 3, 4, 5$ when the growth rate is below 2×10^{-2}.

4.2.1 Growth Rates of Eigenmodes and Comparisons to Previous Works

Figure 4.1 presents a summary of both the linear and non-linear growth-rate analyses. The linear stability analysis is plotted in small dots for the first five non-zero azimuthal modes, showing only the fastest-growing instability for each azimuthal mode. Squares indicate estimates of the growth rates produced by Nguyen et al. (2012), with grid resolution of 100×100, and large circles show the growth rates predicted by the non-linear simulations in QG SPINS (see section 4.3.4).

For very large vortices, Bu $< 10^{-1}$, the LSA reveals that $k_\theta = 1, 2, 3, 4, 5$ are each unstable with roughly comparable growth rates as Bu $\to 10^{-2}$. In the non-linear simulation with Bu $= 10^{-2}$ it was determined that the first five azimuthal modes were the only ones that experienced exponential growth at the early stages (not shown). This is the rationale for only considering these modes in the linear stability analysis since these calculations were computationally demanding. The stability of $k_\theta = 3, 4, 5$ is computed for the full parameter range, but they were only found to be unstable for very small Burger numbers, and are stable in each of the following regimes.

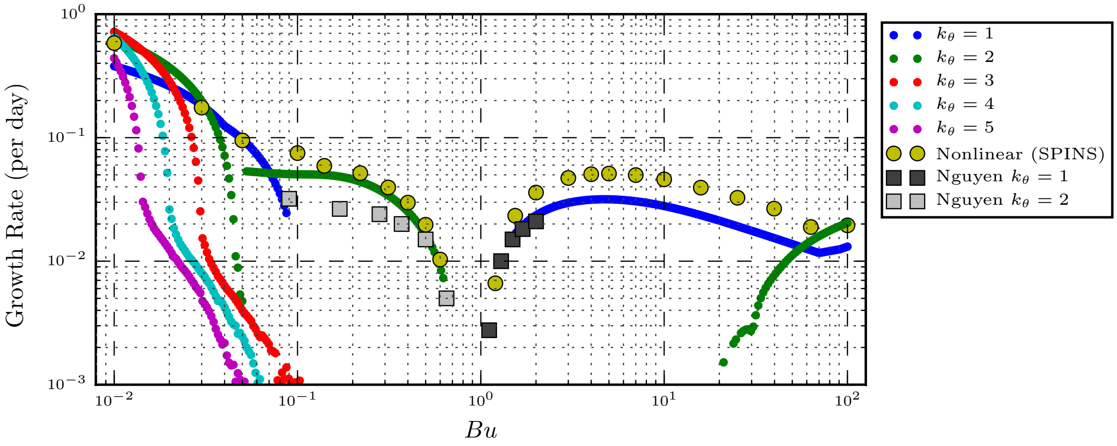

Figure 4.1: Linear stability analysis. Results from linear stability analysis (points), non-linear simulations (yellow circles), and estimates of the Nguyen et al. (2012) result (squares).

For moderately large vortices, $10^{-1} < \mathrm{Bu} < 1$, the primary instability has a $k_\theta = 2$ structure and is vertically symmetric about the mid-depth (see figure 4.4A). Throughout, the growth rates computed from the non-linear simulations agree well with those found in the linear calculations but are larger than those predicted by Nguyen et al. (2012). The disagreement with previous LSA results could be attributed to resolution. It has been recently shown that lens-shaped vortices in this regime can be stabilized by modifying the vortex profile (Sutyrin and Radko, 2016), which could explain how small Bu Meddies persist for long times.

Vortices on the order of the deformation radius, $\mathrm{Bu} \approx 1$, are stable in the linear stability calculations, agreeing with Nguyen et al. (2012) and the non-linear simulations.

Vortices smaller than the deformation radius, $1 < \mathrm{Bu} < 10$, have an unstable mode with a mode one azimuthal structure. In this case the growth rates predicted by the LSA agree with the predictions of Nguyen et al. (2012), but are significantly smaller than those observed in the non-linear simulations. The non-linear simulations used a three-dimensional Cartesian coordinate system and only imposed boundary conditions in the far-field, in contrast to the cylindrical coordinates used in the linear stability problem. As discussed in Ash and Khorrami (1995), the geometry of the problem means that the $k_\theta = 1$

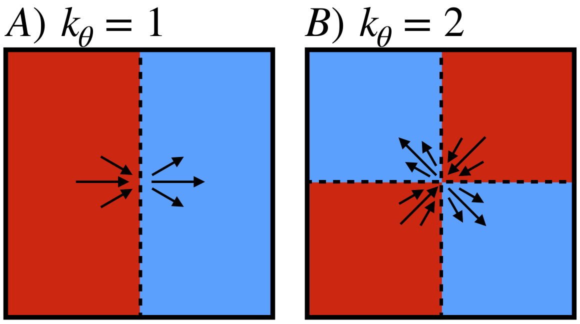

Figure 4.2: Illustration of how, in cylindrical coordinates, only $k_\theta = 1$ is able to demonstrate non-zero flow through the origin. Arrows indicate a sample flow field near the origin ($r = 0$), while colours indicate the symmetries.

mode alone can present non-zero flow at $r = 0$ [1] , a feature which is present in the non-linear simulations but not the linear stability calculations. Further, in the non-linear simulations the perturbation stream-function grows exponentially along $r = 0$ at a rate that is roughly comparable to the instability growth rate. A strict $k_\theta = 1$ mode could not present this, since an odd mode necessarily vanishes at the origin. As will be discussed in section 4.5, the instability in this regime produces vortex tilting through depth-varying horizontal translations of the vortex. These translations/tilting cause the vortex axis to become distinct from the $r = 0$ axis, producing non-zero stream-function perturbations along $r = 0$. Since the reference axis has changed, the original projection onto azimuthal modes becomes invalid, suggesting that linear stability analysis using azimuthal decomposition is inherently flawed when considering $k_\theta = 1$ modes. We have also solved the linearized QG equations in a modified version of QG SPINS in order to capture the true most unstable mode. Unfortunately, our preliminary investigations have only recovered the same mode as is predicted from the LSA, which perhaps suggests that non-linearity is important in the dynamics. This is something that we will investigate in future work.

For very thin vortices, $\mathrm{Bu} > 10$, both $k_\theta = 1, 2$ are unstable. The growth rates from the non-linear simulations agree with the LSA for the two right-most points, for which the $k_\theta = 2$ mode is dominant.

These results agree qualitatively with Mahdinia et al. (2016), who found that for $|Ro| \ll 1$ the dominant instability transitions from a symmetric $k_\theta = 2$ mode when $\mathrm{Bu} < 1$ to an

---

[1] Figure 4.2 illustrates how the symmetry of a $k_\theta = 1$ system allows for a non-zero flow through $r = 0$ with a uniquely defined direction. In contrast, a $k_\theta = 2$ setting would be unable to provide a unique direction for a non-zero velocity at $r = 0$ without breaking continuity.

asymmetric $k_\theta = 1$ mode when Bu > 1. When Bu $\ll 1$, Mahdinia et al. (2016) predict the return of an asymmetric $k_\theta = 1$ mode. Our linear stability results confirm that an asymmetric mode-one instability does arise for Bu $\ll 1$. However, taking the Burger number smaller still, Bu $\lesssim 0.04$, the mode-one instability is again symmetric and presents an $(r - z)$-spatial structure similar to the $k_\theta = 1$ mode of comparable Bu. The following section compares the spatial structures with Yim (2015); Yim et al. (2016) in order to identify the observed instabilities.

4.2.2 Identification of Unstable Modes

Barotropic instabilities develop from an unstable horizontal shear and predominantly extract kinetic energy from the background flow. In contrast, baroclinic instabilities occur when perturbations can extract potential energy from a basic state, for which there must be a vertical shear. Rayleigh's theorems give a necessary condition for each type of instability to occur in planar flow (Pedlosky, 1987), and these can be adapted to circular geometries (Gent and McWilliams, 1986). The necessary condition for a vortex in the stratified QG model to be barotropically unstable is that the radial gradient of the background PV, what we call $\partial_r Q$, changes sign along the radial direction. In contrast, the corresponding necessary condition for baroclinic instability in QG is that the radial gradient of the PV changes signs in the vertical direction (Gill, 1982, p. 564).

For the particular Gaussian profile under consideration here, both necessary conditions are satisfied for all Bu. However, for large enough Bu, the radius where the sign changes in the vertical is far above the vortex since it is dominated by horizontal shear. Similarly, for small enough Bu the radius at which $\partial_r Q$ changes sign is far removed from the center because vertical shear is dominant. The change of shear dominance is why, even though the necessary criteria for both barotropic and baroclinic instabilities are satisfied for all Bu, we expect the instabilities for large (small) Bu to be mostly barotropic (baroclinic).

Some care needs to be taken regarding the classification of the unstable modes. This chapter follows the nomenclature presented in Yim et al. (2016). A brief description of some of the important unstable modes is provided here. The term *Gent-McWilliams* mode refers to the barotropic instability that Gent and McWilliams (1986) called an *internal* mode, or a mode whose maximum growth rate occurs for a non-zero vertical wavenumber. In comparison, *Baroclinic Gent-McWilliams* mode refers to an instability that is characteristically very similar to a traditional *Gent-McWilliams* mode, but occurs in the regime of baroclinic instabilities (Bu < 1), and so is necessarily a baroclinic instability.

The modal structures that are presented here are not new, but are included in order to classify the unstable modes through comparison with Yim et al. (2016). The plots of the unstable modes, Figures 4.3 and 4.4, use colour-maps provided by Thyng et al. (2016).

These colour-maps are used later in Figures 4.10 and 4.11. Note that in figure 4.3 and 4.4 no colour-bar is shown since the magnitude of the linear modes is not important. However, the colour-bar is kept consistent across all figures for the purpose of comparison.

For $10^{-2} < \mathrm{Bu} < 10^{-1}$, there are two regimes of interest, the transition between which occurs at roughly $\mathrm{Bu} = 0.04$. Figures 4.3 A) and B) present the spatial structure of the $k_\theta = 1$ mode for $\mathrm{Bu} = 0.03$. Interestingly, the spatial structure of all five computed modes ($k_\theta \in \{1, 2, 3, 4, 5\}$) are qualitatively very similar. Following Yim et al. (2016), this regime corresponds to a *Baroclinic Instability mode*. Figures 4.3 C) and D) show the spatial structure for $k_\theta = 1$ when $\mathrm{Bu} = 0.05$. This mode falls within the regime of what Yim et al. (2016) call a *Baroclinic Gent-McWilliams mode* (see their figure 39d). In contrast to the *Baroclinic Instability mode*, this mode is vertically asymmetric and has a lower radial mode number.

For $10^{-1} < \mathrm{Bu} < 1$, the only unstable mode corresponds to $k_\theta = 2$. Figures 4.4 A) and B) plot the stream-function for $\mathrm{Bu} = 0.14$. This is a baroclinically unstable mode and corresponds to the *Baroclinc-Shear mode*, as named by Yim et al. (2016). This is readily verified by comparing these structures with the pressure field in Figure 5.46 of Yim (2015).

For $1 < \mathrm{Bu} < 10$, consider the unstable mode with $k_\theta = 1$ and $\mathrm{Bu} = 5$, the stream-function of which is presented in figures 4.3 E) and F). This is the only unstable mode in the range $1 < \mathrm{Bu} < 10$, and is due to the barotropic shear that is dominant in this parameter regime. This mode is asymmetric about the centre and is referred to as the *Gent-McWilliams mode*, as first introduced in Gent and McWilliams (1986), and further studied in Yim et al. (2016). These plots are similar to those of C) and D), however it should be emphasized that the underlying mechanism is a barotropic instability. Correspondingly, this mode is less radially constrained and more vertically constrained than the corresponding *Baroclinic Gent-McWilliams mode*. Note that the stream-function agrees qualitatively with the pressure field in Figure 5.43 of Yim (2015).

For $10 < \mathrm{Bu} < 100$, both $k_\theta = 1$ and $k_\theta = 2$ are unstable. Figures 4.3 G) and H) plot the stream-function of the most unstable $k_\theta = 1$ mode for $\mathrm{Bu} = 100$. It is readily seen that the mode is symmetric about the centre, in contrast to $\mathrm{Bu} = 5$, but more importantly there are much smaller vertical scales that develop near the top and bottom of the vortex, with the mode vanishing near the vortex core. Figures 4.4 C) and D) present the spatial structure of the $k_\theta = 2$ instability in this regime. This mode is barotropic in nature, again based on the stability criteria previously mentioned. The real part of this is very similar to the *Shear mode* studied in Yim et al. (2016).

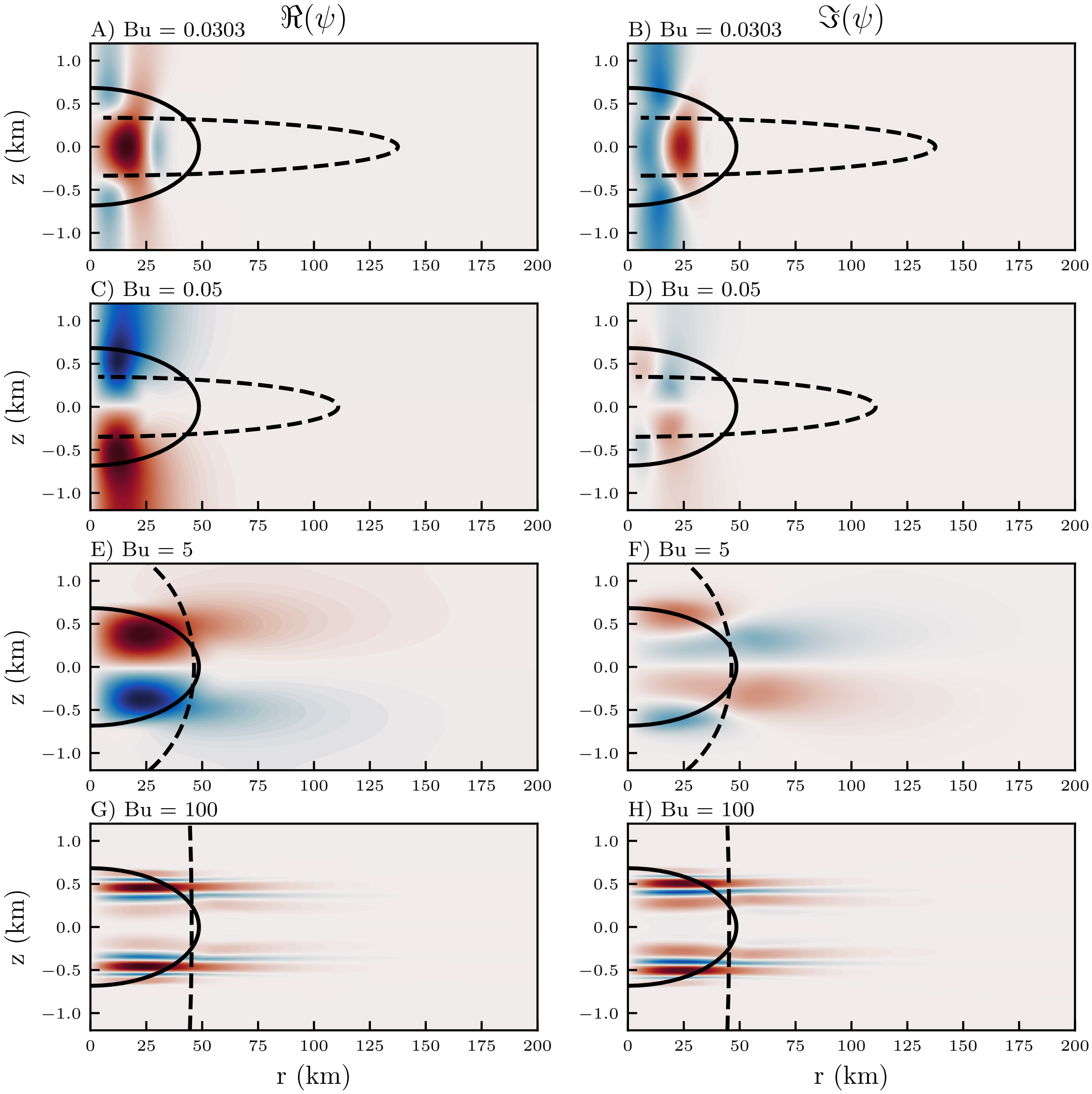

Figure 4.3: Contours of the real (left column) and imaginary (right column) components of the dominant $k_\theta = 1$ instability for selected Bu values. In each plot the colour bar is normalized to $[-1, 1]$ for comparison. The solid black contour line indicates the 10% stream-function level. The dashed black contour line indicates when the radial gradient of the background potential vorticity ($\partial_r Q$) changes sign.

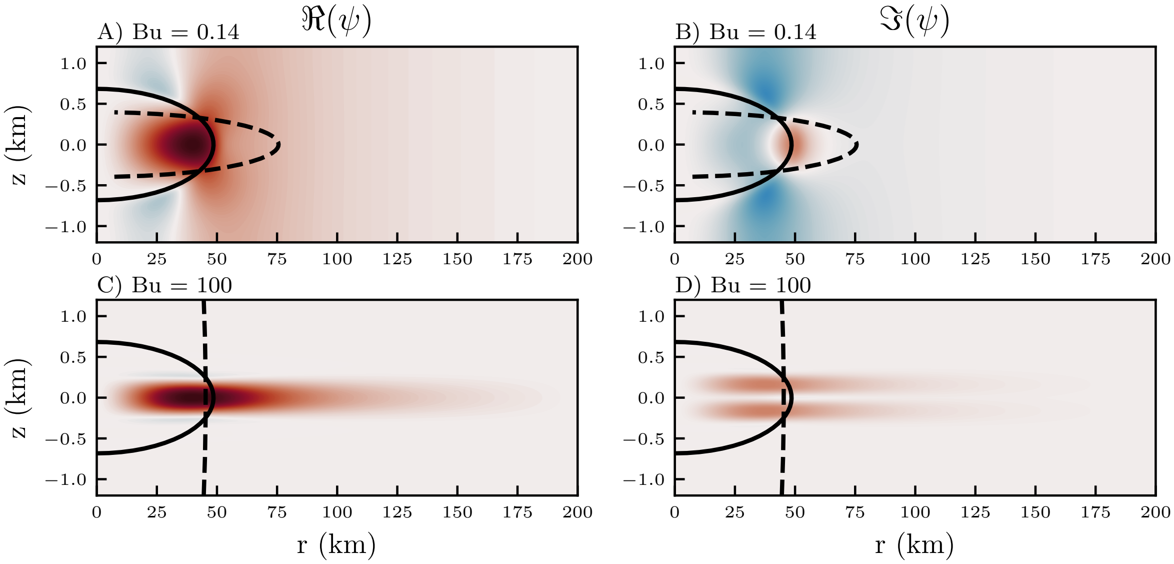

Figure 4.4: Contours of the real (left column) and imaginary (right column) components of the dominant $k_\theta = 2$ instability for selected Bu values. In each plot the colour bar is normalized to $[-1, 1]$ for comparison. The solid black contour line indicates the 10% stream-function level. The dashed black contour line indicates when the radial gradient of the background potential vorticity ($\partial_r Q$) changes sign.

4.3 Impact of the Burger Number on Non-linear Evolution

By using sufficiently small perturbations, typically six to eight orders of magnitude smaller than the basic state extrema, the simulated instabilities undergo an exponential growth phase (hereafter termed the linear regime) in accordance with what is predicted from linear theory, thereby providing a means to confirm predictions of the linear stability analysis. In addition, the three-dimensional simulations provide several other diagnostic tools, including three-dimensional renderings of the instability (*VisIt*, see Childs et al., 2012), measuring the extent and direction of energy transfers, computing wavenumber-dependent rates of change of energy, and quantifying the generation of small-scale energy.

In this section, two non-linear simulations are presented. The first is a representative for the moderately large Burger regime: with $\mathrm{Bu} = 5$, corresponding to a 5 km vortex. The second case presented is a representative of the moderately small Burger regime, with $\mathrm{Bu} = 0.14$ and corresponding to a 30 km vortex. While many more non-linear simulations were performed, these two simulations provide a good representation of the two primary regions of interest and the corresponding instabilities: $k_\theta = 1$ for large Bu and $k_\theta = 2$ for small Bu.

4.3.1 Large Burger Number Regime

Figures 4.5 A - D present four three-dimensional renderings of the vortex in various stages of destabilization. Each plot presents volume renderings of potential vorticity q, where gold denotes anti-cyclonicity and teal indicates cyclonicity. Note that the displayed aspect ratio differs greatly from the true aspect ratio.

The first frame, 4.5A, illustrates the initial conditions, in this case with $\mathrm{Bu} = 5$, hereafter referred to as the large Burger case. Physically, a large Burger number restricts the amount of vortex tube stretching that can occur. In equation (4.1.2), this corresponds to decreasing the influence of the vertical derivative of the stream-function. As a result, the vortex is dominated by horizontal shear, as demonstrated by the initial horizontal shielding of the anti-cyclonic core by a cyclonic layer.

The next frame, figure 4.5B, shows the initial destabilization at the end of the linear regime when the system is transitioning into non-linear saturation. The anti-cyclonic core begins to tilt, which results in tail-like features at the vertical periphery as the vortex continues to rotate about the original axis. As the tilted vortex rotates, there is strong tearing, or shedding, of the cyclonic shielding as the strong anti-cyclonic core interacts with the outer cyclonic layer.

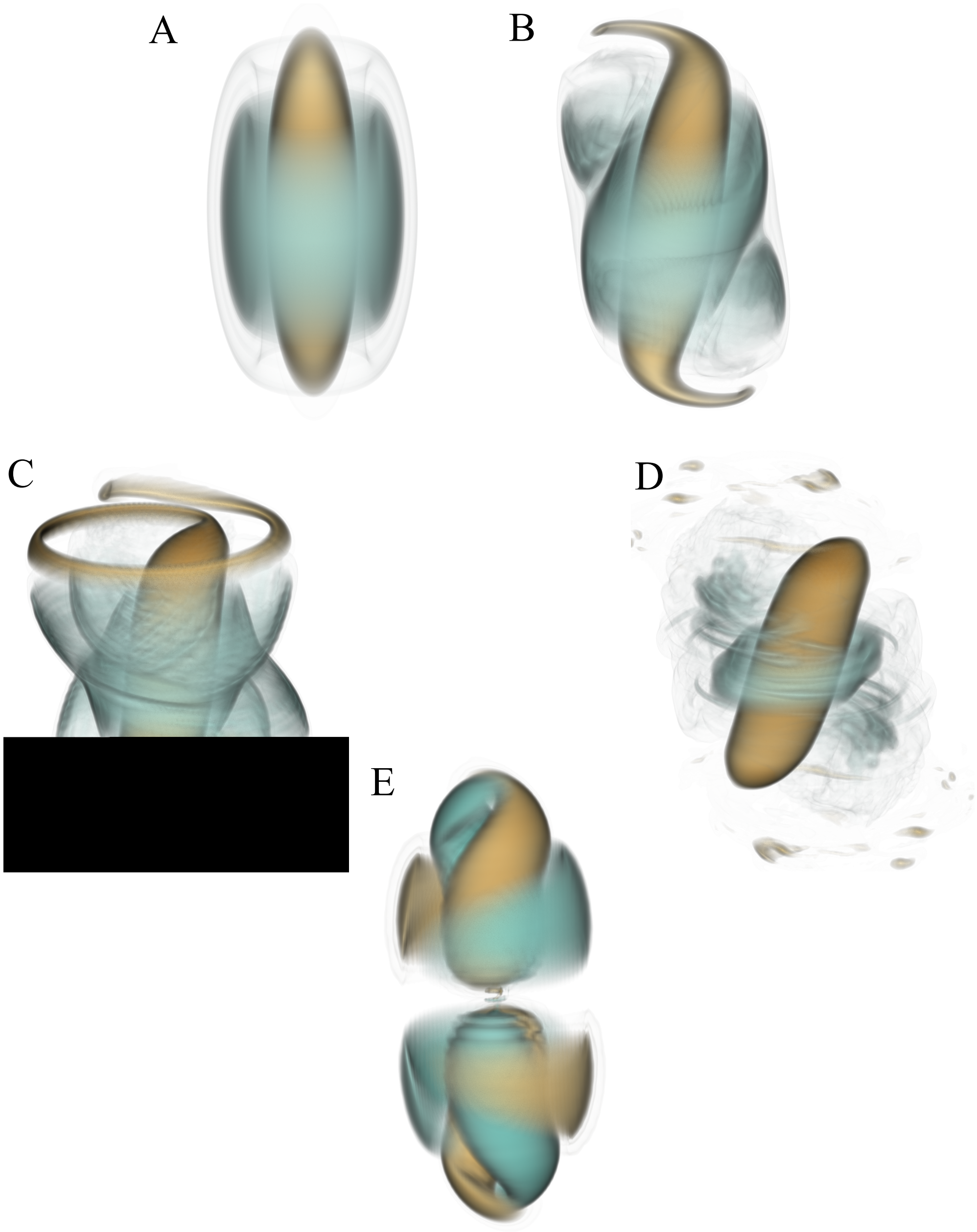

[redacted]

Figure 4.5: Three-dimensional plots of a Bu = 5 vortex at select times. Renderings are of the potential vorticity, with gold denoting anti-cyclonicity and teal denoting cyclonicity. A: initial conditions. B: 570 days. C: 640 days. D: 1060 days. E: perturbation field at 190 days. Aspect ratio not to scale.

Later, in figure 4.5C, the tails have elongated and have begun to separate from the vortex core, while the shielding deteriorates further. The remnants of the cyclonic shield show interesting spatial patterns at the length scale of the original vortex as well much smaller scale filamentary features. Ultimately, figure 4.5D reveals the quasi-steady end state. The tilted anti-cyclonic core has lost the vertical end-tails, which collapsed into small anti-cyclones. The cyclonic shielding has been greatly reduced, with mostly filamentary structures remaining along the centre. The simulation illustrates that for large Burger number, the mode one instability results in vortex tilting. Moreover, while the anti-cyclonic core remains mostly coherent, the cyclonic shielding is mostly removed.

The perturbation potential vorticity, extracted from the linear phase, is presented in figure 4.5E. As anticipated from the linear stability analysis, the mode demonstrates vertical asymmetry and has an azimuthal mode of $k_\theta = 1$. The dominant instability is composed of two twinned cores of opposing polarity in the centre, with thinner ribbons wrapping along the vortex periphery. The twinned cores and vertical asymmetry correspond to the vortex tilting, a mechanism which is further discussed in section 4.5.

Gent and McWilliams (1986) studied the stability of columnar vortices and found that $k_\theta = 1$ (their $l = 1$) corresponds to an instability with a baroclinic helical vertical structure. The instability presented here is comparable to the Gent-McWilliams $k_\theta = 1$ instability in that both present baroclinic helical structures, with one difference being the 'ribbons' along the vortex periphery in the non-linear simulation.

4.3.2 Small Burger Number Regime

Figures 4.6 A - D present four three-dimensional renderings of the vortex in various stages of destabilization. Since the fields are typically symmetric about the mid-depth, only the lower half domain is presented in order to provide a more detailed view of the system.

Figure 4.6A illustrates the initial conditions, a $\mathrm{Bu} = 0.14$ interior vortex. In the small Bu regime, vortex tube stretching is anticipated to be an important mechanism in contrast to horizontal shear. Indeed, the vortex is dominated by vertical shear, as demonstrated by the tri-lobe structure in the vertical (recall that only the lower half domain is presented, so the tri-lobe appears as a 1.5-lobe). That is, for small Burger numbers the cyclonic shielding appears in the vertical, while the shielding is in the horizontal for large Burger numbers.

The initial destabilization of the vortex is shown in figure 4.6B and the formation of arms in both the anti-cyclonic and cyclonic lobes is visible. Ménesguen et al. (2012) present seismic readings that indicate the presence of similar arm features in observed Meddies. Then, figure 4.6C shows that the core vortex has torn into two vortices of roughly equal size, with a trail of small vortices remaining, remnants of the vorticity filament that connected

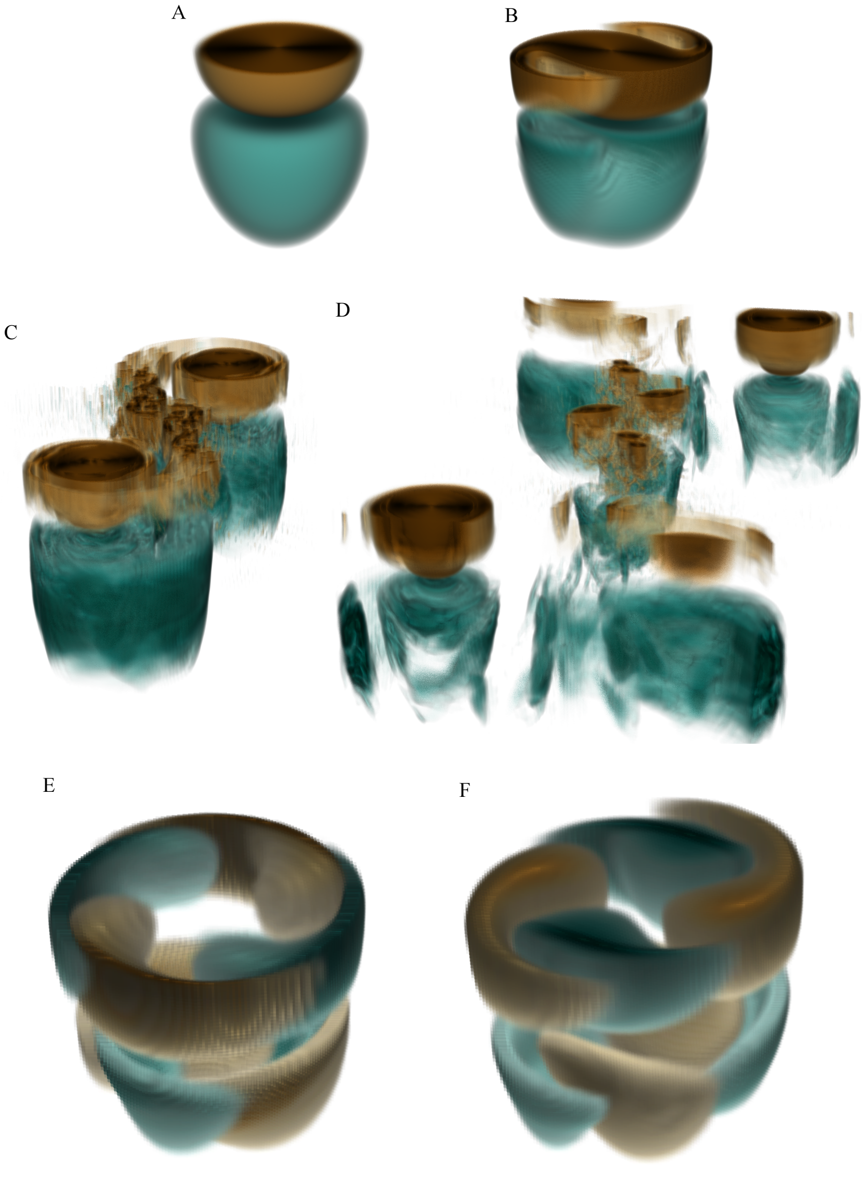

Figure 4.6: Three-dimensional plots of the inferior half-domain of a Bu = 0.14 (30 km) vortex at select times. Renderings are of the potential vorticity, with gold denoting anti-cyclonicity and teal denoting cyclonicity. A: initial conditions. B: 2530 days. C: 2860 days. D: 3200 days. E: perturbations at 1000 days. F: perturbations at 2500 days. Aspect ratio not to scale.

the two new vortices prior to the tearing event. Ultimately, figure 4.5D reveals the quasi-steady end state in which the initial vortex has been reduced to vortices with greatly reduced horizontal scales. During the linear regime, the dominant unstable mode can be extracted and is presented in figures 4.6 E - F. In contrast with figure 4.5E, this mode is primarily restricted to the vortex periphery. Figure 4.6F, which shows the perturbation field at 2500 days, shows how the $k_\theta = 2$ mode generates the arm structures. This is classified as a *Baroclinic-Shear Instability mode* (Yim et al., 2016).

4.3.3 Azimuthal Decomposition: a Comparison with Linear Theory

While the growth rates presented in figure 4.1 provide the over-all growth rate of the perturbation fields in the non-linear simulations, it does not distinguish between azimuthal modes. In order to compute the growth rates of the individual modes, the perturbation field of each three-dimensional simulation is projected onto a cylindrical coordinate basis, where the centre of the coordinate system corresponds to the centre of the initial vortex. A Fourier transform is applied to the azimuthal dimension to decompose the perturbation into k_θ-components. The transformed system is then integrated in r and z in order to compute the net contribution of each azimuthal mode. That is, for each k_θ the contribution $p\left(k_\theta\right)$ of each azimuthal mode is computed as:

$$p(k_\theta) = \int_{z=-Lz}^{z=0} \int_{r=0}^{r=L_r} \widehat{q}(r, k_\theta, z)^2 dr dz,$$

where $\widehat{q}$ denotes the θ-Fourier transformed potential vorticity perturbation, so that, following Parseval's theorem, $p(k_\theta)$ measures the k_θ component of the perturbation enstrophy, $(q - Q)^2$. Figure 4.7 presents a summary of the growth of the first ten azimuthal modes for a selection of non-linear simulations. In each plot, the vertical dotted lines indicate the beginning and end of the linear phase, while the vertical dashed line marks an approximation to the non-linear saturation time. Note that the azimuthal projections may be unreliable after the linear regime, as the vortices may tear or shift, causing the projection to cylindrical coordinates to be inappropriate.

In agreement with the linear stability analysis, the projections show that the large Burger number regime ($1 < \mathrm{Bu} \lesssim 10$, small vortex widths) is initially dominated by growth of the $k_\theta = 1$ mode, while small Burger number ($0.1 \lesssim \mathrm{Bu} < 1$, large vortex widths) is dominated by a $k_\theta = 2$ mode, and very small Burger number ($\mathrm{Bu} \lesssim 0.1$, very large vortex widths) demonstrates growth in both $k_\theta = 1$ and $k_\theta = 2$ modes. Towards the end of the linear phase, the non-dominant modes experience very rapid growth, corresponding to non-linear interaction.

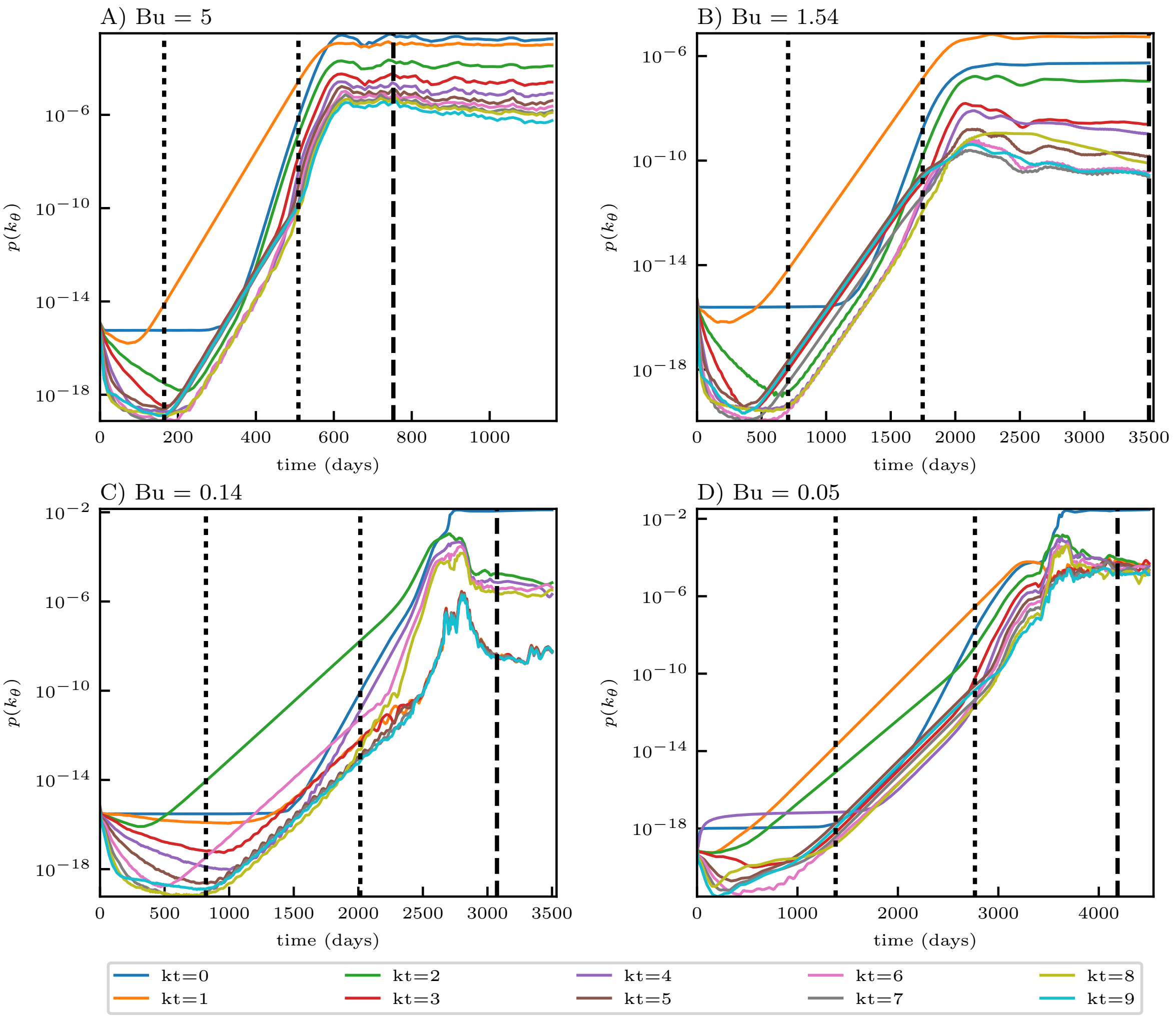

Figure 4.7: Azimuthal decompositions for four selected non-linear simulations, depicting the growth of the separate modes. Burger numbers are given in figure labels. The vertical dotted lines indicate an estimate for the beginning and end of the linear regime. The vertical dashed line estimates the non-linear saturation time. The first three subfigures show that the linear theory correctly predicts the most unstable mode that grows initially. The fourth subfigure the demonstrates that there are initially two unstable modes.

4.3.4 Main Stages of Non-Linear QG Evolution

Studying the growth of the total perturbation does not require a projection into cylindrical coordinates, and so in this subsection the full perturbation is considered instead of individual azimuthal modes. Further, the growth rate of the fastest growing azimuthal mode in each of the four cases presented in figure 4.7 was compared to those of the full perturbation and the two were found to agree to at least two significant digits. Note that figure 4.7 uses a log-scale and that during the linear growth phase the dominant mode is several orders of magnitude stronger than the other modes. The growth-rate diagnostics as well as integrated energy diagnostics are used to describe the different stages of the evolution of the unstable vortices.

Figure 4.8 presents the evolution of the norms of the full perturbation and associated growth rates (left column) and domain-integrated energetics (right column) for non-linear simulations with Bu $= 5, 0.31, 0.14$, and 0.05. For the left column, the red curve is associated with the left-hand y-axis and presents the normalized norm of the perturbation:$\frac{||q-Q||_2}{||q||_2+||Q||_2}$. Correspondingly, the blue curve is associated with the right-hand y-axis and presents the time derivative of the norm of the perturbation scaled by the Rossby number: $\frac{1}{Ro} \cdot \frac{d}{dt} (\log ||q - Q||_2)$. The growth rate is scaled by Ro since, following Vallis (2006, p. 207), the dimensionless time $t \cdot f_0$ scales as Ro^{-1}. In both metrics, q refers to the full potential vorticity field, while Q refers to the initial vortex solution. For the right column, kinetic (KE) and potential (PE) energy are computed as:

$$\text{KE} = \frac{1}{2}\rho_0 \iiint_V u^2 + v^2 dV = \frac{1}{2}\rho_0 \iiint_V (\partial_x\psi)^2 + (\partial_y\psi)^2 \, dV, \tag{4.3.1}$$

$$\text{PE} = \frac{1}{2}\rho_0 \iiint_V \left(\frac{f_0}{N_0}\partial_z\psi\right)^2 dV, \tag{4.3.2}$$

In each simulation, the motion is nearly conservative, which is reflected by the fact that the net energy loss is less than 1%.

The vertical dotted lines indicate an estimate for the beginning and end of the linear regime. The vertical dashed line estimates the non-linear saturation time by finding the time after which the net energetics change by no more than 2.5% in either direction. Meunier et al. (2015) describe three main stages of vortex destabilization: the linear stage, the splitting stage, and the restabilized stage. These stages correspond with what we term the linear stage, the non-linear transition phase, and the non-linearly saturated phase.

The first simulation (top row) corresponds to Bu $= 5$. This system is initially KE dominant and experiences a net transfer to PE. The energy transfer begins after the linear regime ends. As discussed in section 4.3.1, this system is dominated by vortex tilting. As regards the perturbation growth, the system undergoes smooth exponential growth after

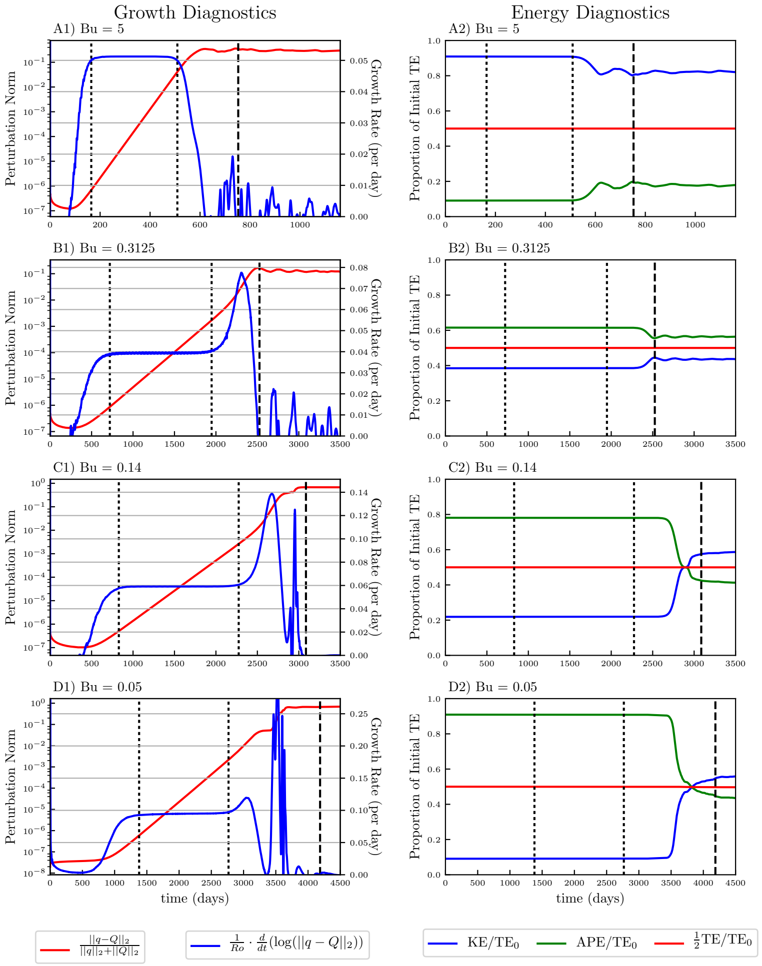

Figure 4.8: Growth rates of the full perturbation (left column) and non-dimensional energies (right column) for four non-linear QG simulations. Burger numbers are given in figure labels. In the left column, the red curves indicate the perturbation norms and the blue curves outline the growth rates. These growth rates are included in figure 4.1 as "Nonlinear (SPINS)", i.e. yellow circles. For the right column, the blue, green, and red curves denotes KE, PE, half the total energy, respectively, each normalized by the initial total energy. The vertical dotted lines indicate an estimate for the beginning and end of the linear regime. The vertical dashed line estimates the non-linear saturation time by finding the time after which the net energetics change by no more than 2.5% in either direction.

which the perturbation growth declines and the system enters a quasi-equilibrated regime. The latter three simulations correspond to Bu $= 0.31, 0.14$, and 0.05. These cases are initially PE dominant, with the initial disparity increasing as Bu decreases. In each case, there is a net transfer of PE to KE, corresponding to a baroclinic instability. The last two simulations experience sufficiently strong energy conversions so as to cause a change in the distribution of energy: the quasi-steady regime is KE dominant while the initial state is PE dominant. In these cases, the time of the change in energy dominance corresponds to the vortex tearing event. The Bu $= 0.31$ simulation, in contrast, remains PE dominant in the quasi-steady regime, and does not undergo vortex splitting. In each of these cases, the linear regime terminates in a rapid but brief increase of the perturbation growth rate. The spike in the perturbation growth rate is associated with the formation of the arms as seen in figure 4.6A.

Figure 4.9A provides measures of how large the instability grows before the system reaches non-linear saturation. The black curves plot the magnitude of the non-linearly saturated perturbation norms, while the magenta and cyan curves respectively plot the net amount of PE and KE transferred. For Bu < 1, the system is characterized by a conversion of PE to KE; in contrast, for Bu > 1 the system demonstrates a KE to PE transfer. These are respectively indicative of a baroclinic and barotropic instability.

Interestingly, the barotropic-type instability for $1 <$ Bu < 10 demonstrates much weaker energy conversion than the baroclinic instability for $10^{-1} <$ Bu < 1, despite the two instabilities having comparable growth rates in the non-linear simulations. Additionally, the proportion of converted energy for Bu > 1 increases when the $k_\theta = 2$ instability returns. Combined, these results suggest that it is not simply that baroclinic instabilities are stronger at converting energy than barotropic instabilities, but instead that the $k_\theta = 2$ mode is able to convert more energy than the $k_\theta = 1$ mode.

The norms of the non-linearly saturated perturbation show qualitatively similar behavior to the net energy transfers. However, in the case of vortex splitting, the non-linearly saturated perturbation may not be meaningful as the system has deviated too strongly from the initial condition.

Figure 4.9B, plots the initial and terminal global Bu for the system. For these purposes,

$$\mathrm{Bu}_{\text{measured}} \approx \frac{1}{2}\frac{KE}{APE} = \frac{1}{2}\left((\partial_x\psi)^2 + (\partial_y\psi)^2\right)\left(\frac{f}{N_0}\partial_z\psi\right)^{-2}.$$

That the blue dots, which indicate the initial Burger number under this metric, coincide with the identity function serves to validate the metric. The dynamics can be divided into three regimes. For Bu ≈ 1, there is no discernible change in Bu, corresponding with the stability of the system. When Bu < 1, the horizontal vortex scale exceeds the

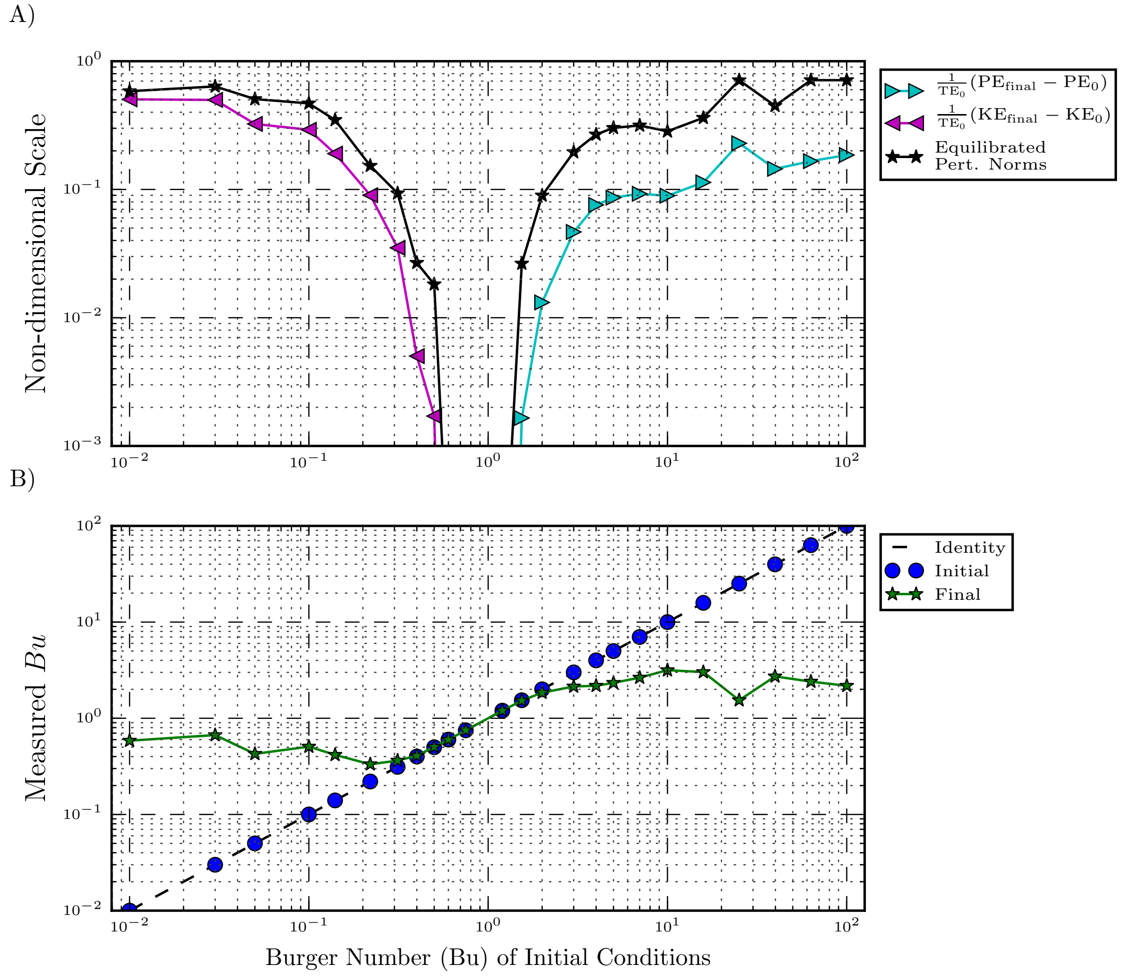

Figure 4.9: a) Net energy conversions (cyan and magenta) and final perturbations norms (black). For the energy transfers, magenta indicates net KE production while cyan indicates net PE production. This reinforces the idea that baroclinic instabilities correspond to Bu $<$ 1 while barotropic instabilities occur for Bu $>$ 1. b) The initial and terminal Burger number for each non-linear simulation.

deformation radius, and the baroclinic instability acts to reduce the horizontal scales, thereby increasing Bu (Vallis, 2006, p. 277). When Bu $>$ 1, the horizontal vortex scale is less than the deformation radius. The primary instability then tilts the vortex, causing an increase in the horizontal length scales and a net decrease in Bu (Gent and McWilliams, 1986). It is interesting to note that, while the instability always serves to drive the system towards the stable neighbourhood of Bu $=1$, stronger instabilities drive the system closer to Bu $=1$ than weak instabilities. As mentioned, the vortex tearing events for $k_\theta = 2$, Bu <1 correspond to the energy parity event, when KE $=$ APE. This suggests that $\text{Bu}_{\text{measured}} = 0.5$ is the Burger number during the vortex tearing event.

There are four major results in this subsection. First, the *Gent-McWilliams* and *Shear Instabilities* for Bu >1 have a net conversion of KE to PE, while the *Baroclinic-Shear* and *Baroclinic Instabilities* for Bu <1 have a conversion of PE to KE. Second, instabilities in the limit of very small Bu convert a greater proportion of initial total energy than in the limit of very large Bu. Third, in the simulation of the instability with $k_\theta = 2$ presented here, the energy parity event corresponds to the tearing event. Finally, sufficiently strong instabilities drive the system towards Bu $=1$, which is stable, and stronger instabilities can drive the system closer to Bu $=1$ than weaker instabilities. This implies that the instability events tend to generate structures whose horizontal length scales are commensurate to the Rossby radius of deformation.

4.3.5 Spectral Distribution of Energy and Energy Transfers

Figures 4.10 and 4.11 present the wavenumber-dependent time-rate of change of the potential and kinetic energies for the large and small Burger number vortices corresponding to figures 4.5 and 4.6. Figure 4.10 is restricted to only consider the linear regime (the portion between the vertical dotted lines in figure 4.8), while figure 4.11 considers the non-linear portion of the simulation (everything after the second vertical dotted line in figure 4.8). In each plot, the vertical axis is time and the horizontal axis represents inverse horizontal length scale. In order to produce the spectra, the full three-dimensional power spectra were azimuthally integrated and depth averaged to produce a mean horizontal power spectrum. The vertical cyan, magenta, and black lines indicate the vortex length, L_h, the deformation radius, L_D, and the filter cut-off, respectively. The horizontal dashed line indicates the estimated non-linear saturation time, as in figure 4.8.

Note that figures 4.10 and 4.11 each use two different logarithmic scales, with red (blue) indicating that energy is increasing (decreasing) in time. In each of figures 4.10 and 4.11, the upper row corresponds to the large Burger case, while the lower row corresponds to the small Burger case.

Recall that the large Bu case presents a net transfer of KE to PE. Throughout the

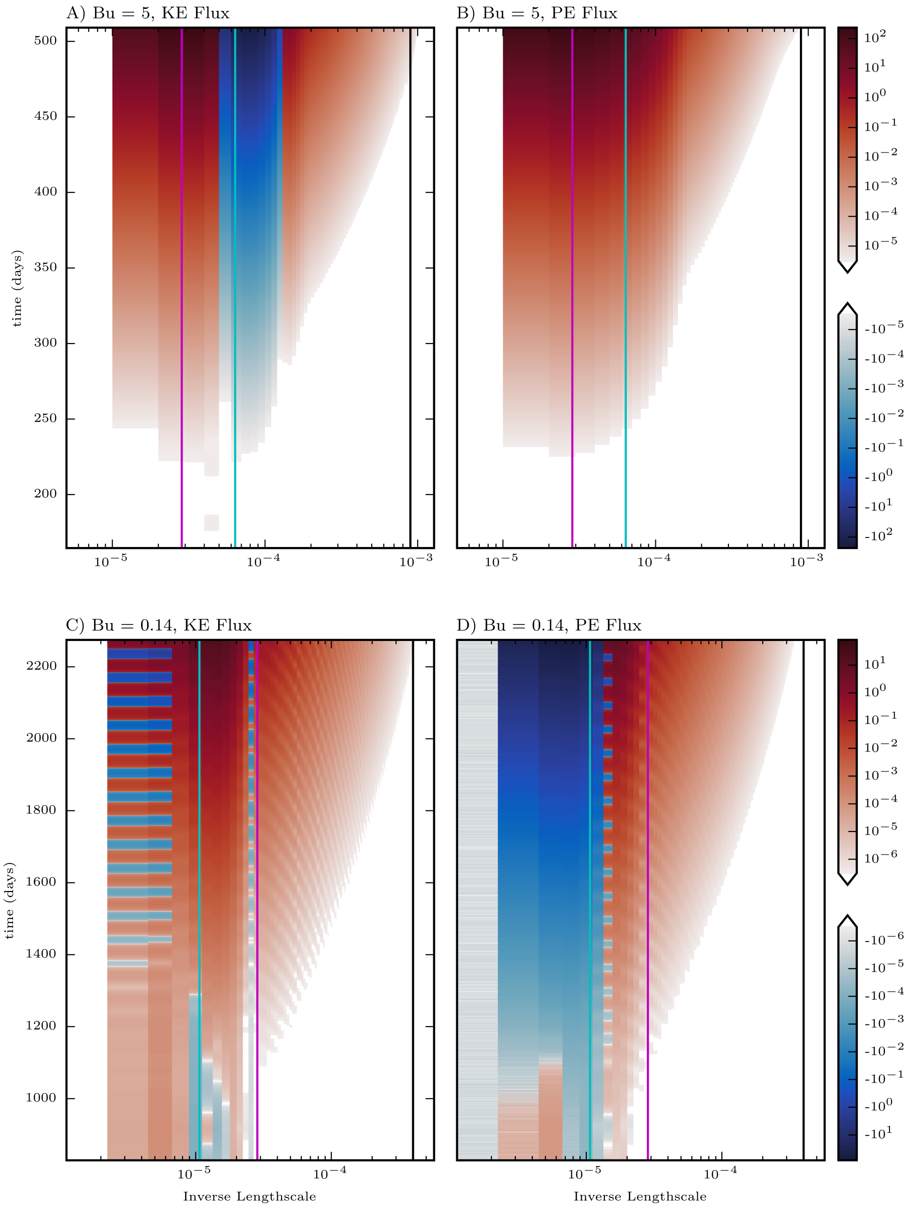

Figure 4.10: Wavenumber-dependent time-rate of change of KE (left column) and PE (right column) for Bu = 5 (top row) and Bu = 0.14 (bottom row) during the linear regime. The horizontal axis is inverse lengthscale (m^{-1}) and the vertical axis is time (days). The vertical cyan, magenta, and black lines indicate the vortex length, the deformation radius, and the filter cut-off respectively.

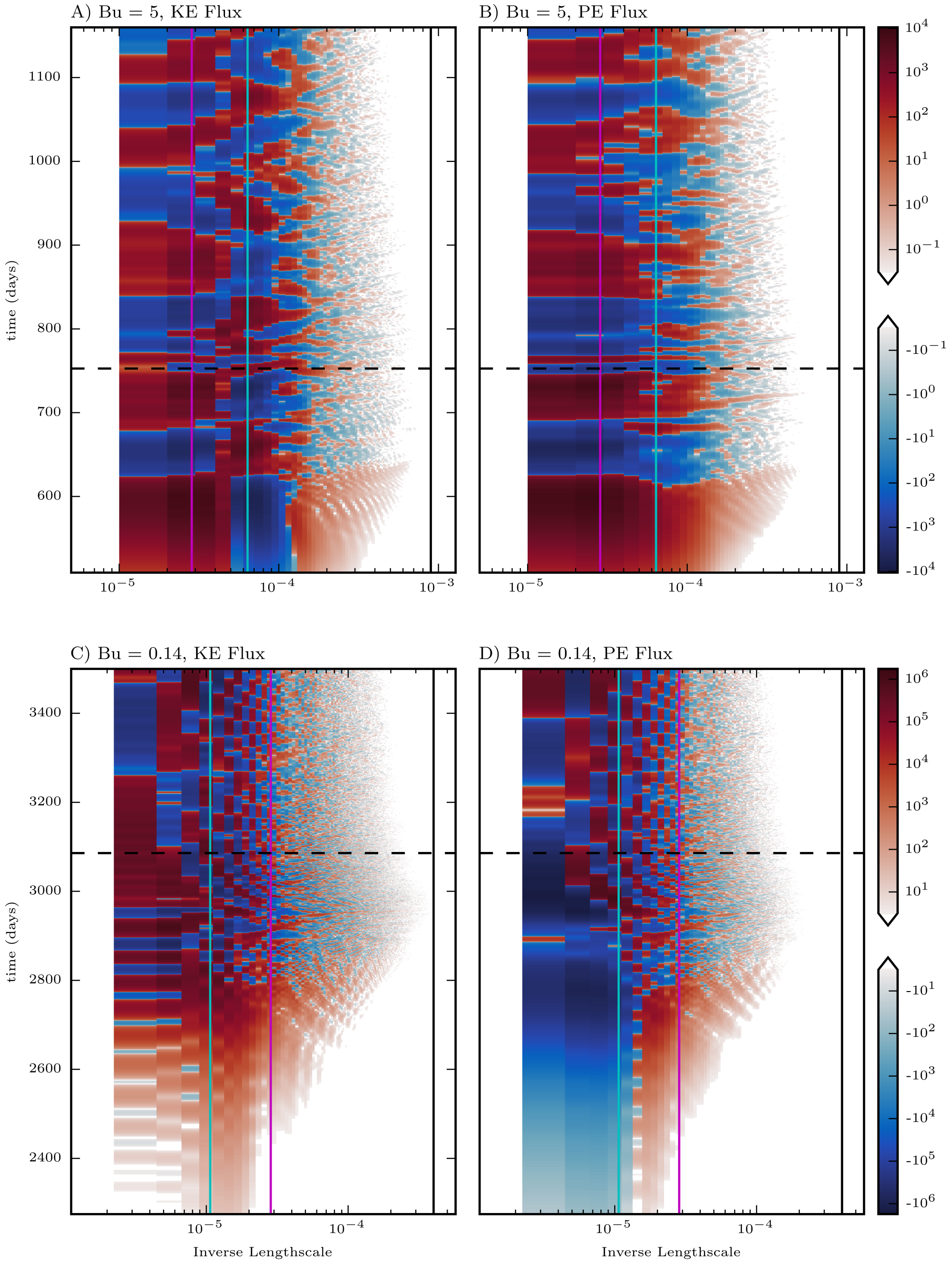

Figure 4.11: Same as Figure 4.10 for times after the linear regime. The horizontal dashed line indicates the estimated non-linear saturdation time.

linear regime (figure 4.10 A - B), KE increases at deformation scales and decreases at vortex scales, while PE increases at both deformation and vortex scales. Both KE and PE present positive energy fluxes to smaller scales. The beginning of the non-linear regime (figure 4.11 A - B) is marked with a positive flux towards small scales in both KE and PE, the magnitudes of which well exceeds the generation of small-scales presented in figure 4.10 A - B. At the conclusion of the down-scale energy flux, the system enters into a quasi-steady regime, in which PE alternates between increasing and decreasing at all scales. While KE demonstrates similarly periodic features, the sign of the flux alternates between sub-vortex scales and super-deformation scales.

The lower rows, figures 4.10 C - D and 4.11 C - D, present the spectra for the small Burger case shown in figure 4.6. The fluxes in the linear regime are characterized by a loss of PE and gain of KE at vortex and super-vortex scales, as well as a gain of both KE and PE at sub-vortex scales. In the non-linear regime, there is a loss of PE and a gain of KE at the vortex scale. Similar to the large Bu case, the system demonstrates a positive energy flux towards small scales within the non-linear transition regime, with the small-scale generation reaching smaller scales for kinetic energy than potential energy; the positive flux to small scales can be seen in Figure 4.11 in the red regions at scales smaller than the vortex length. Leading up to the production of small scales, the small Bu system exhibits a loss of PE and gain of KE at super-vortex lengths and a gain of both KE and PE at super-deformation and sub-vortex lengths. These fluxes correspond to the loss of energy at large length scales and the production of energy at small length scales as a result of the vortex splitting event. Again, similar to the large Bu case, in the quasi-steady regime the small Bu case exhibits temporally-periodic oscillations in flux. However, in the small Bu case the oscillations change sign more rapidly with both time and wavenumber than in the large Bu case. The oscillating fluxes below the deformation scale are significantly weaker and oscillate with a higher frequency than the fluxes above the deformation scale. In total, there is a noticeable increase in large-scale KE and loss of PE at large scales over the duration of the simulation.

Figure 4.12 presents a time-mean of the spectral energy fluxes during the linear regime, which corresponds to the times shown in figure 4.10, for a selection of simulations. Note that the horizontal axis is held constant across each plot for the purpose of comparison, and that the spectra do not necessarily span the whole domain for each plot. As a result, the vertical magenta lines, which indicate the respective deformation radii, are aligned.

For each simulation, the fluxes during the linear and first portion of the non-linear phases (the portion before the termination of the positive flux towards small scales) demonstrate qualitatively similar flux patterns (not shown). The main distinction is that, as seen in figures 4.10 and 4.11, the strength of the fluxes in the non-linear regime are several orders of magnitude stronger than the fluxes in the linear regime. This suggests that the linear phase simply ‘initializes’ the instability, but does not significantly impact the energetics.

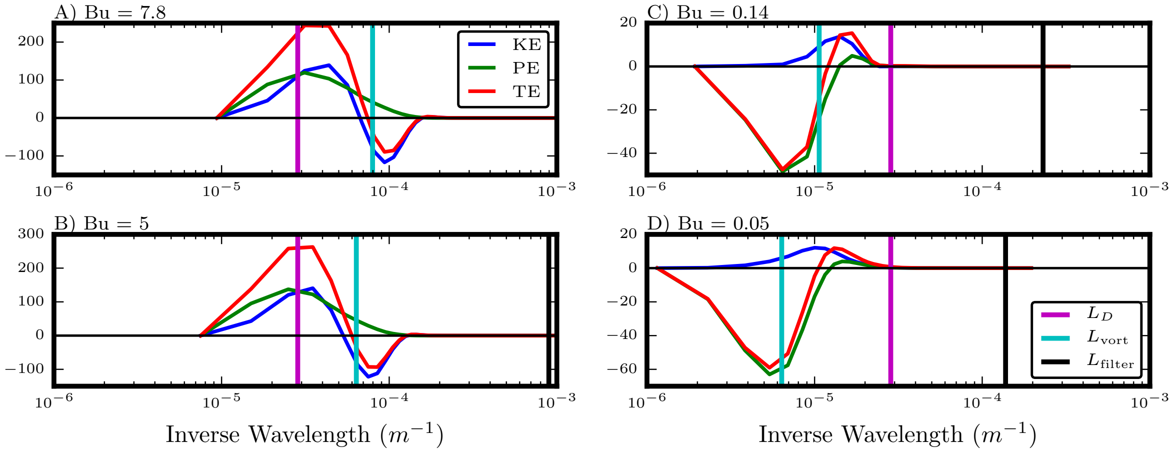

Figure 4.12: Time-averages of net wavenumber-dependent time-rates of change of energy across the full linear phase (as defined in figure 4.8 and illustrated in figure 4.10) for four different Bu values. The solid red, green, and blue curves provide the time-mean flux of total, potential, and kinetic energy respectively. Vertical cyan lines denote the vortex length, vertical black dotted lines indicate the filter cut-off, and vertical magenta lines identify the vortex length.

For large Bu (left column) the instability is characterized by a net loss of total energy (TE) and KE at vortex scales, with a corresponding increase of TE, KE, and PE at the deformation scale. The positive flux of energy towards larger scales corresponds to a vortex-tilting mechanism, which increases horizontal length scales. As the vortex scale increases, the wavenumber corresponding to the greatest negative energy flux also increases so that the two remain essentially coincident.

The right column of figure 4.12 corresponds to Bu < 1. In these cases, there is a loss of TE and PE at scales equal to or greater than the vortex scale, while TE and KE are produced at scales between the vortex length and deformation radius. Some PE is also produced at sub-vortex scales, but the energy generation is predominantly kinetic. The net energy transfer towards sub-vortex scales corresponds to a vortex-splitting mechanism, which produces smaller vortices with length scales more comparable to the deformation radius. Further, consider the wavenumber corresponding to the greatest positive energy flux. As the vortex length increases, the wavenumber of greatest positive flux also increases so that it remains roughly halfway (in a logarithmic sense) between the vortex and deformation scales.

In both cases, the non-linear dynamics create a strong positive energy flux to small scales in both KE and PE. Figure 4.13 presents three quantifications of the production

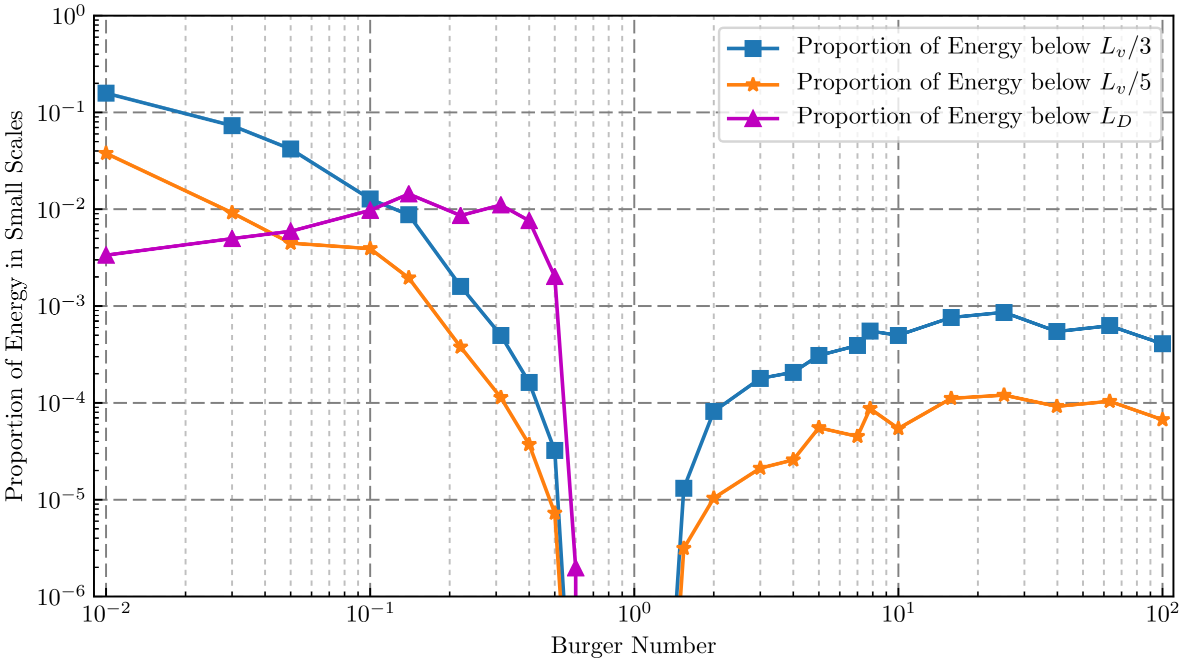

Figure 4.13: Three metrics for the production of small-scale energy. Points indicate the proportion of initial total energy that is at scales equal to or less than i) one third of the vortex scale (blue squares), ii) one fifth of the vortex scale (orange asterisks), or iii) the deformation radius (magenta triangles), at the end of the simulation.

of small scales: the proportion of energy in length scales smaller than one third of the vortex scale (blue squares), smaller than one fifth of the vortex scale (orange asterisks), and smaller than the deformation radius (magenta triangles). When $\mathrm{Bu} > 1$, the vortex itself is smaller than the deformation radius, and so the third metric is not meaningful. Note that the figure uses a log-scale. The two vortex-based metrics show two main trends. $\mathrm{Bu} < 1$ instabilities tend to be able to produce significantly more sub-vortex scale energy than when $\mathrm{Bu} > 1$, corresponding to a bias towards generating deformation-scale energy. Further, sub-vortex scale production increases as Bu deviates from 1, suggesting that larger vortices, which correspond to higher growth rates, also demonstrate a down-scale energy flux that reaches a wider range of wavenumbers. In contrast, the deformation-scale metric is maximized on $10^{-1} \lesssim \mathrm{Bu} \lesssim 3 \times 10^{-1}$. Above that, the amount of produced small scales decreases rapidly with increasing Bu, corresponding to the stabilization of the system. Below $\mathrm{Bu} = 0.1$, the amount of produced small-scale energy increases weakly with Bu.

We are not able to provide a definitive explanation as to why $\mathrm{Bu} \in [0.1, 0.4]$ maximizes the generation of sub-deformation radius energy. The spatial structure of the unstable modes do not present significant changes in small scale features, which is why the sub-deformation scale energy that is created must arise due to the nonlinearity of the system. This is not something that can be described in the context of linear theory and is beyond the scope of this project to explain this observation. A scale argument may help to explain why there is a region with maximized sub-deformation scale generation: as Bu decreases, the separation between the vortex scale and the deformation scale increases, and so a stronger energy transfer is required to produce sub-deformation energy for smaller Bu.

4.4 Anisotropy

The anisotropy metrics from chapter 3 can then be applied to the $Bu = 5$ and $Bu = 0.14$ cases that have been considered in detail. The wavenumber-dependent anisotropy and associated z-scores are shown in Figure 4.14. The initial grey bands roughly indicate the scale below which there is no significant vortex energy. In each case, small scale energy is initially statistically neutral, but is quickly isotropized to produce an over-all strongly isotropic initial field, denoted by the large red regions ($z < -2$). While this behaviour is expected for scales with significant vortex energy, which is by construction isotropic, it is interesting that scales without significant vortex energy rapidly isotropize, suggesting a cohering effect from the vortex. The $Bu = 5$ case, which has a predominantly up-scale cascade, shows a transition from strongly isotropic to statistically neutral anisotropies at small scales, but no significant changes above the deformation radius. In contrast, the $Bu = 0.14$ case, which has a strong down-scale cascade, has broad-spectrum anisotropization: scales above the deformation radius reduce to statistically neutral, while scales scales below the deformation radius are strongly anisotropized. After the vortex tearing event, the system begins to re-isotropize, particularly between the vortex and deformation scales, which is likely a result of the new-formed vortices that are more commensurate with the deformation radius.

4.5 Conclusions and Discussion

LSA is conducted using both high spatial and parametric resolution and is compared to both Nguyen et al. (2012) and non-linear simulations. It is determined that there are four different instability regimes. For moderately small Bu, $10^{-1} < \mathrm{Bu} < 1$, the linear and nonlinear results are in good agreement, but differ from the growth rates predicted by Nguyen et al. (2012) for decreasing Bu, a discrepancy which is explained by the requirement for high resolution to accurately resolve the fine-scale features. For moderately large Bu, $1 < \mathrm{Bu} < 10$, the presented LSA agrees well with Nguyen et al. (2012), but both LSA

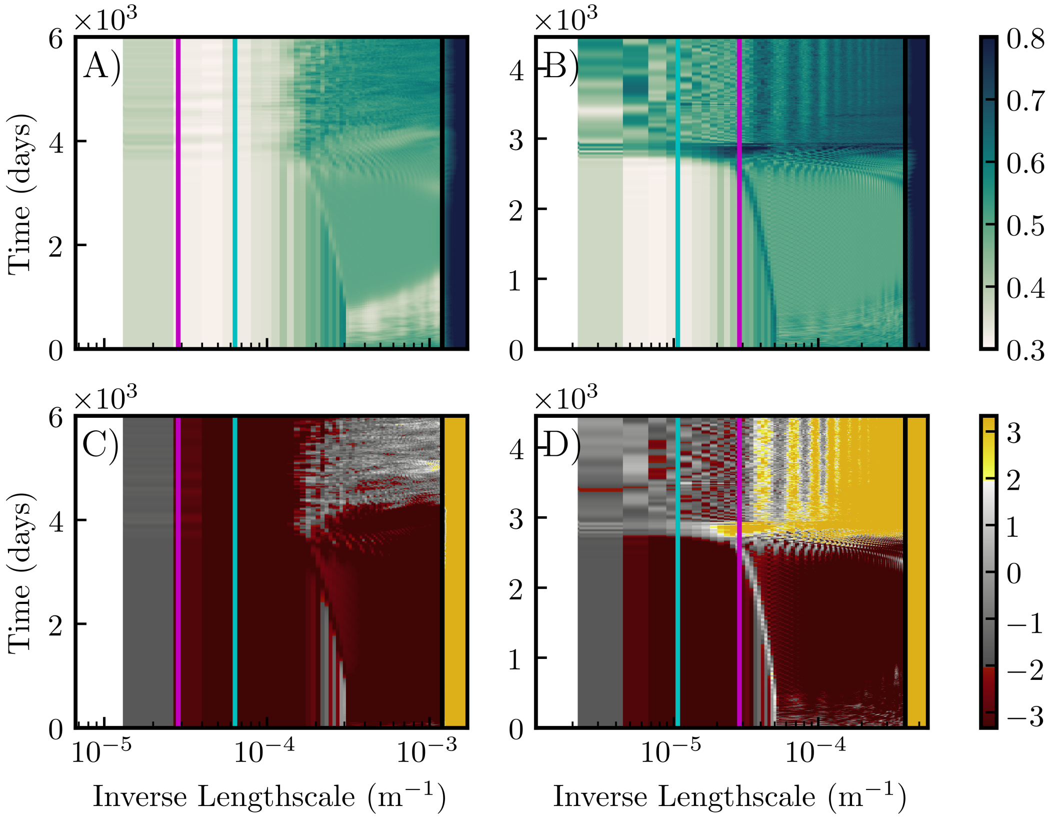

Figure 4.14: Wavenumber-dependent anisotropy metrics for the $Bu = 5$ (left column) and $Bu = 0.14$ (right column) cases. The top row shows the metric while the bottom row gives the z-score. In each frame the cyan, magenta, and black lines indicate the vortex, deformation, and filter scales respectively. The vertical axis is time (note: not common between the two columns) and the horizontal axis is the inverse lengthscale.

calculations disagree with the non-linear simulations. As discussed in section 4.2.1, this is in part caused by the additional condition that is imposed on the perturbation at the center of the vortex. Comparison with the linear modes presented by Yim et al. (2016) revealed that the instabilities in those regimes are the *Baroclinic Shear Instability* and *Gent-McWilliams Instability* respectively. Further, the presented LSA considered an expanded range of Bu: $10^{-2} < \mathrm{Bu} < 10^{2}$. For very large Bu, $\mathrm{Bu} > 10$, the $k_\theta = 2$ modes is again unstable, for which the LSA agrees with the non-linear calculations, re-enforcing that the discrepancy is inherent to the $k_\theta = 1$ mode. For very small Bu, $\mathrm{Bu} < 0.1$, all of the computed azimuthal modes are unstable, and it is anticipated that higher azimuthal modes are also unstable.

For moderately small Burger numbers ($0.1 < \mathrm{Bu} < 1$), or moderately large vortex scales, the dominant instability is vertically symmetric about the vortex centre, has azimuthal mode two and, following the nomenclature of Yim et al. (2016), is a *Baroclinic Shear Instability.* When the instability is sufficiently strong, as illustrated in figures 4.6 E - F, the $k_\theta = 2$ mode causes the formation of arms and a pinching of the vortex core, which can lead to vortex splitting. When a splitting even occurs, it corresponds to parity between kinetic and potential energy. Vortices in this regime have horizontal scales that exceed the deformation radius; as a result, vortex tearing produces vortices on scales that are more commensurate with the first deformation radius. The small Bu instability is characterized by a net transfer of potential energy into kinetic energy, which is consistent with a baroclinic instability. Corresponding to the decrease in horizontal scales, there is an over-all transfer of energy from vortex scales and larger towards sub-vortex and super-deformation scales (figure 4.12).

Moderately large Burger numbers ($1 < \mathrm{Bu} < 10$), or moderately small vortex scales, contrastingly present a dominant instability that is vertically asymmetric about the vortex centre, has azimuthal mode one, and is a *Gent-McWilliams Instability* (following Yim et al. (2016)). The $k_\theta = 1$ mode strengthens one side of the vortex while weakening the other, which yields an effect similar to horizontal translation. As a result of the vertical asymmetry, the upper portion of the vortex is translated in the opposite direction of the lower portion; resulting in vortex tilting. Since vortices in this regime have sub-deformation horizontal scales and vortex tilting increases horizontal scales, the tilting mechanism produces vortices on scales closer to the deformation radius. Corresponding to the increase in horizontal scales, kinetic and total energy transition from vortex lengths towards deformation lengths, while potential energy is generated at all scales with an emphasis on the deformation radius. Overall, there is a net transfer of kinetic energy into potential energy.

In the small Bu regime ($0.1 < \mathrm{Bu} < 1$) the cyclonic and anti-cyclonic portions of the vortex undergo similar evolution. In contrast, the large Bu regime ($1 < \mathrm{Bu} < 10$) has markedly different evolutions for the two portions: the anti-cyclonic core undergoes vortex tilting, while the cyclonic shielding is heavily dispersed.

As Bu decreases, a greater proportion of the initial energy is transferred to sub-vortex scales, corresponding to the increased strength of the instability. However, $10^{-1} \lesssim \mathrm{Bu} \lesssim 3 \times 10^{-1}$ maximizes the amount of sub-deformation radius energy that is produced. $\mathrm{Bu} > 1$ produces significantly less sub-vortex energy than $\mathrm{Bu} < 1$, corresponding to the net up-scale energy transfer. We do not have a physical explanation for why $10^{-1} \lesssim \mathrm{Bu} \lesssim 3 \times 10^{-1}$ maximizes the production of small scales, although it is interesting to note that this regime corresponds with the range for observed Meddies.

Many studies considered Meddies in the context of a Gaussian vortex, and we begin with the same basis, but find that the model is problematic. The observed long-lasting Meddies have Bu considerably less than one, while a Gaussian vortex would be unstable in that regime. Meddies that do not encounter sea mounts can live up to four years (Richardson et al., 2000). In the region $0.1 < \mathrm{Bu} < 0.3$, the growth rate estimated by both the presented LSA and non-linear simulations is approximately $Ro \times 0.05/\mathrm{day}$, so the timescale for the instability is 200 days if $Ro = 0.1$. As a result, small (1%) perturbations may yield a lens vortex lifetime of 1000 days, while larger (10%) perturbations may shorten the lifetime to 200-400 days.

Other assumptions made throughout this investigation were: the ambient rotation (f_0) is very strong compared to that of the vortex, the stratification is strong, and that it is only the density that is important, not the temperature-salinity distribution. In future work we will study lens vortices in a primitive equation model which will allow us to determine the merit in making some of these assumptions. This will allow for a more accurate description of the unstable modes in the very small Burger number regime.

In this chapter we sought to understand how lens vortices, idealized with a Gaussian stream-function, destabilize over a wide range of Burger numbers. We began by presenting a more precise view of the linear theory and what growth rates and spatial structures are expected as a function of Burger number. Then, by looking at the nonlinear evolution, we quantify the transfer of energy across the different length scales to better understand how sub-mesoscale features are generated as a function of Burger number. We hope that the combination of these two studies will lead to better parameterizations of unstable lens-shaped vortices that arise in the World's oceans.

Chapter 5

Summary and Conclusions

This thesis worked through the development of numerical models for simulating quasi-geostrophic systems in both doubly-periodic and channel geometries. In addition to presenting the details of the decomposition used to achieve this, a series of demonstration cases were used to illustrate various features of the model. Next, a spectrally-defined metric for length-scale dependent anisotropy was presented and its characteristic behaviour studied in the classical setting of two-dimensional turbulence. The statistical properties were studied analytically for the case of white noise, and numerically for QG turbulence. Finally, these tools were applied to study the linear and non-linear evolution of interior lens-shaped Gaussian vortices, inspired by the study of Mediterranean eddies.

By building on the efficient parallel framework provided by SPINS, *SPIQG* provides a powerful tool for simulating one-layer and linearly stratified quasi-geostrophic systems in high-performance computing environments. The python drivers for initializing and postprocessing simulations provide a user-friendly system for running simulations by minimizing the extent to which the user is required to interact with the source code. The built-in diagnostic tools enable the user to generate very high resolution time-series of important diagnostics, including perturbation norms, energy, enstrophy, power spectra, and anisotropy.

SPIQG extends the traditional spectral QG model by incorporating a decomposition that permits the use of channel geometries while still permitting and evolving non-zero net zonal transport along the channel. The decomposition is further extended to include the option of momentum forcing. The nature of the decomposition limits the forcing functions to analytically specified functions for which third derivatives and higher vanish, or essentially vanish, near the boundary.

A spectrally-defined metric for anisotropy is then presented to provide a way to measure orientation preference as a function of wavelength. While the presented metric has similarities to that of McWilliams et al. (1994), it provides a significant extension by accurately identifying anisotropies in which the preferred orientation may not align with the coordinate axes. It was shown that there is statistically significant variation between the anisotropy profiles for white noise and two-dimensional QG turbulence, revealing that the turbulence field was persistently more anisotropic. This discrepancy highlights the importance of using the appropriate reference state when measuring the statistical significance of measured anisotropy.

These tools were then applied to the study of interior lens-shaped vortices, which were taken to be idealized Gaussian vortices within a linear stratification. The linear and non-linear dynamics of these vortices were studied across a wide range of Burger numbers in order to understand the parametric dependence of the behaviour. When comparing the linear results, it was shown that for $0.1 < \mathrm{Bu} < 1$, higher resolution was required than previously used in order to resolve the small scale features. More interestingly, for $1 < \mathrm{Bu} < 10$ the azimuthal decomposition from cylindrical coordinates requires enforcing an additional boundary condition at the vortex centre, which is incompatible with the development of a mode-1 azimuthal structure. The particular instabilities were then classified following the nomenclature of Yim et al. (2016).

Next, the three-dimensional non-linear evolution of the vortices was studied using *SPIQG*, which illustrated the dominant vortex tilting mechanism in the $Bu = 5$ case and the vortex tearing in the $Bu = 0.14$ case. In each case, there is a general trend to produce deformation-scale energy, meaning a net upscale transfer for $Bu > 1$ and a net downscale transfer for $Bu < 1$. By measuring the net energy transfers, it was shown that $0.1 \lesssim \mathrm{Bu} \lesssim 0.3$ maximized the production of energy in sub-deformation scales.

5.1 Future Work

The *SPIQG* project can be further extended by incorporating a basin geometry in which all four sides are bounded by no-flux walls. In this case the streamfunction is constant and equal along all walls, but again that constant may vary in time. Extensions to planetary geostrophy and surface quasi-geostrophy would also be worthwhile. Another significant direction for development in SPINS would be to create a modified pressure solver in order to permit simulation under the hydrostatic Navier-Stokes equations. This extension would maintain much dynamic richness, while greatly reducing the cost of the pressure solve and relaxing the time-step restriction.

The primary extension for the anistropy study would be to perform a suite of simulations to obtain a statistical sample of the reference anisotropy for a series of classical turbulence problems, including stratified and un-stratified non-rotating three-dimensional turbulence.

These reference states could then be applied to diagnose anisotropy in a wider range of simulations.

For the lens-shaped vortex project, a meaningful extension is to relax the QG assumption and study their non-linear evolution under either hydrostatic or non-hydrostatic Navier-Stokes. This study would serve to determine the parameter regime in which one could justifiably use the QG model to study large-scale oceanic lens vortices. More specifically, by conducting a similar parameter sweep, which would now include the Rossby number in addition to the Burger number, the domain of validity could be determined.

References

Hidenori Aiki and T. Yamagata. A numerical study on the successive formation of Meddy-like lenses. *Journal of Geophysical Research*, 109(C6):C06020, 2004.

Robert L. Ash and Mehdi R. Khorrami. Vortex Stability. In *Fluids Vortices*, pages 317–372. 1995.

Jean-Michel Baey and Xavier Carton. Vortex multipoles in two-layer rotating shallow-water flows. *Journal of Fluid Mechanics*, 460:151–175, 2002.

Kevin H. Baines, Thomas W. Momary, Leigh N. Fletcher, Adam P. Showman, Maarten Roos-Serote, Robert H. Brown, Bonnie J. Buratti, Roger N. Clark, and Philip D. Nicholson. Saturn's north polar cyclone and hexagon at depth revealed by Cassini/VIMS. *Planetary and Space Science*, 57(14-15):1671–1681, dec 2009.

Xavier Carton. Modeling of oceanic vortices. *Surveys in Geophysics*, 22(36):179 – 264, 2001.

J.G. Charney. On the Scale of Atmospheric Motions. *Geofysike Publikasjoner*, 17(2), 1948.

Dudley B. Chelton, Michael G. Schlax, and Roger M. Samelson. Global observations of nonlinear mesoscale eddies. *Progress in Oceanography*, 91(2):167–216, 2011.

Hank Childs, Eric Brugger, Brad Whitlock, Jeremy Meredith, Sean Ahern, David Pugmire, Kathleen Biagas, Mark Miller, Cyrus Harrison, Gunther H Weber, Hari Krishnan, Thomas Fogal, Allen Sanderson, Christoph Garth, E Wes Bethel, David Camp, Oliver Rübel, Marc Durant, Jean Favre, and Paul Návratil. VisIt: An end-user tool for visualizing and analyzing very large data. *High Performance Visualization–Enabling Extreme-Scale Scientific Insight*, 2012.

Daniele Ciani. *Tourbillons océaniques intensifiés en subsurface: signature en surface et interactions mutuelles.* Phd, Université de Bretagne Occidentale, 2016.

Daniele Ciani, Xavier Carton, Igor Bashmachnikov, Bertrand Chapron, and Xavier Perrot. Influence of deep vortices on the ocean surface. *Discontinuity, Nonlinearity, and Complexity*, 4(3):281 – 311, 2015.

P. A. Davidson. *Turbulence.* Oxford University Press, 2004.

Dale R. Durran. *Numerical Methods for Fluid Dynamics*, volume 32 of *Texts in Applied Mathematics.* Springer New York, New York, NY, second edition, 2010. ISBN 978-1-4419-6411-3.

Glenn R. Flierl. Simple applications of McWilliams' "A note on a consistent quasi-geostrophic model in a multiply connected domain". *Dynamics of Atmospheres and Oceans*, 1(5):443–453, jul 1977.

Glenn R. Flierl and Joseph Pedlosky. The Nonlinear Dynamics of Time-Dependent Subcritical Baroclinic Currents. *Journal of Physical Oceanography*, 37(4):1001–1021, 2007.

Glenn R. Flierl, P. Malanotte-Rizzoli, and N. J. Zabusky. Nonlinear Waves and Coherent Vortex Structures in Barotropic beta-plane Jets, 1987.

Peter R. Gent and James C. McWilliams. The instability of barotropic circular vortices. *Geophysical & Astrophysical Fluid Dynamics*, 35(1):209–233, 1986.

Adrian E. Gill. *Atmosphere-Ocean Dynamics.* Academic Press, 1982.

James R. Holton. *An Introduction to Dynamic Meteorology.* Academic Press, third edit edition, 1972.

Bach Lien Hua, Claire Ménesguen, Sylvie Le Gentil, Richard Schopp, Bruno Marsset, and Hidenori Aiki. Layering and turbulence surrounding an anticyclonic oceanic vortex: in situ observations and quasi-geostrophic numerical simulations. *Journal of Fluid Mechanics*, 731:418–442, 2013.

Pijush K. Kundu and Ira M. Cohen. *Fluid Mechanics.* Academic Press, fourth edition, 2008.

John L. Lumley. Computational Modeling of Turbulent Flows. *Advances in Applied Mechanics*, 1979.

Mani Mahdinia, Pedram Hassanzadeh, Philip S Marcus, and Chung-Hsiang Jiang. Stability of 3D Gaussian vortices in an unbounded, rotating, vertically-stratified, Boussinesq flow: Linear analysis. *Journal of Fluid Mechanics*, 706:34–45, may 2016.

James C. McWilliams. Submesoscale, coherent vortices in the ocean. *Reviews of Geophysics*, 23(2):165–182, 1985.

James C. McWilliams, Jeffrey B. Weiss, and Irad Yavneh. Anisotropy and coherent vortex structures in planetary turbulence. *Science*, 1994.

Claire Ménesguen, Bach Lien Hua, Xavier Carton, F. Klingelhoefer, P. Schnürle, and C. Reichert. Arms winding around a meddy seen in seismic reflection data close to the Morocco coastline. *Geophysical Research Letters*, 39(5), mar 2012.

Thomas Meunier, Claire Ménesguen, Richard Schopp, and Sylvie Le Gentil. Tracer Stirring around a Meddy: The Formation of Layering. *Journal of Physical Oceanography*, 45(2): 407–423, 2015.

Louis-Philippe Nadeau and David N. Straub. Basin and Channel Contributions to a Model Antarctic Circumpolar Current. *Journal of Physical Oceanography*, 39(4):986–1002, apr 2009.

Hai Yen Nguyen, Bach Lien Hua, Richard Schopp, and Xavier Carton. Slow quasi-geostrophic unstable modes of a lens vortex in a continuously stratified flow. *Geophysical & Astrophysical Fluid Dynamics*, 106(3):305–319, jun 2012.

Athanasios Papoulis. *Probability, Random Variables, and Stochastic Processes.* McGraw-Hill, New York, 1965. ISBN 0070484481.

Joseph Pedlosky. *Geophysical Fluid Dynamics.* Springer New York, New York, NY, 1987. ISBN 978-0-387-96387-7.

Stephen B. Pope. *Turbulent Flows.* Cambridge University Press, 2000. ISBN 9780511840531.

Francis J. Poulin, Glenn R. Flierl, and Joseph Pedlosky. The Baroclinic Adjustment of Time-Dependent Shear Flows. *Journal of Physical Oceanography*, 40(8):1851–1865, aug 2010.

Mark D. Prater and Thomas B Sanford. A Meddy off Cape St. Vincent. Part I : Description. *Journal of Physical Oceanography*, 24:1572–1586, 1994.

William H. Press, Saul A. Teukolsky, William T. Vetterling, and Brian P. Flannery. *Numerical Recipes in Fortran.* Cambridge University Press, second edi edition, 1986.

Peter B. Rhines. Waves and turbulence on a beta-plane. *Journal of Fluid Mechanics*, 69 (3):417–443, 1975.

P. L. Richardson, A. S. Bower, and W. Zenk. A census of Meddies tracked by floats. *Progress in Oceanography*, 45(2):209–250, 2000.

Nuno Serra and Isabel Ambar. Eddy generation in the Mediterranean undercurrent. *Deep-Sea Research Part II: Topical Studies in Oceanography*, 49(19):4225–4243, 2002.

Nuno Serra, S. Sadoux, Isabel Ambar, and D. Renouard. Observations and Laboratory Modeling of Meddy Generation at Cape St. Vincent. *Journal of Physical Oceanography*, 32(1):3–25, 2002.

Nuno Serra, Isabel Ambar, and Rolf H. Käse. Observations and numerical modelling of the Mediterranean outflow splitting and eddy generation. *Deep-Sea Research Part II: Topical Studies in Oceanography*, 52(3-4):383–408, 2005.

Benjamin A. Storer, Francis J. Poulin, and Claire Ménesguen. The Dynamics of Quasigeostrophic Lens-Shaped Vortices. *Journal of Physical Oceanography*, 48:937–957, 2018.

Christopher J. Subich, Kevin G. Lamb, and Marek Stastna. Simulation of the Navier-Stokes equations in three dimensions with a spectral collocation method. *International Journal for Numerical Methods in Fluids*, 73(2):103–129, sep 2013.

Georgi Sutyrin and Timour Radko. Stabilization of Isolated Vortices in a Rotating Stratified Fluid. *Fluids*, 1(3):26, aug 2016.

Sigurdur T. Thoroddsen and C. W. Van Atta. The Influence of Stable Stratification on Small-Scale Anisotropy and Dissipation in Turbulence. *Journal of Geophysical Research*, 1992.

Kristen Thyng, Chad Greene, Robert Hetland, Heather Zimmerle, and Steven DiMarco. True Colors of Oceanography: Guidelines for Effective and Accurate Colormap Selection. *Oceanography*, 29(3):9–13, sep 2016.

Lloyd Nicholas Trefethen. *Spectral Methods in MATLAB*. Society for Industrial and Applied Mathematics, Philadelphia, 2000.

Ross Tulloch and K. Shafer Smith. A new theory for the atmospheric energy spectrum: Depth-limited temperature anomalies at the tropopause. *Proceedings of the National Academy of Sciences*, 103(40):14690—-14694, 2006.

Ross Tulloch and K. Shafer Smith. Quasigeostrophic Turbulence with Explicit Surface Dynamics: Application to the Atmospheric Energy Spectrum. *Journal of the Atmospheric Sciences*, 66(2):450–467, feb 2009.

Geoffrey K. Vallis. *Atmospheric and Oceanic Fluid Dynamics*. Cambridge University Press, Cambridge, U.K., 2006.

Geoffrey K. Vallis. *Climate and the Oceans*. Princeton University Press, 2012.

Ashwin R. Vasavada, Andrew P. Ingersoll, Don Banfield, Maureen Bell, Peter J. Gierasch, Michael J.S. Belton, Glenn S. Orton, Kenneth P. Klaasen, Eric DeJong, H.Herbert Breneman, Todd J. Jones, James M. Kaufman, Kari P. Magee, and David A. Senske. Galileo Imaging of Jupiter's Atmosphere: The Great Red Spot, Equatorial Region, and White Ovals. *Icarus*, 135(1):265–275, sep 1998.

Michael L. Waite and Peter Bartello. Stratified turbulence dominated by vortical motion. *Journal of Fluid Mechanics*, 517:281–308, sep 2004.

Paul Williams, T. W. N. Haine, P. L. Read, S. R. Lewis, and Y. H. Yamazaki. QUAGMIRE v1.3: a quasi-geostrophic model for investigating rotating fluids experiments. *Geoscientific Model Development*, 2(1):13–32, feb 2009.

John C. Wyngaard. *Turbulence in the atmosphere*. Cambridge University Press, 2010. ISBN 9780511840524.

Eunok Yim. *Stability of Columnar and Pancake Vortices in Stratified-Rotating Fluids*. Docteur de l'école polytechnique, École polytechnique, 2015.

Eunok Yim, Paul Billant, and Claire Ménesguen. Stability of an isolated pancake vortex in continuously stratified-rotating fluids. *Journal of Fluid Mechanics*, 801:508–553, aug 2016.

Mengnan Zhao and Mary-Louise Timmermans. Vertical scales and dynamics of eddies in the Arctic Ocean's Canada Basin. *Journal of Geophysical Research: Oceans*, 120(12): 8195–8209, dec 2015.

APPENDICES

Appendix A

Derivations for *SPIQG*

A.1 Conservation of Mass

Beginning with the shallow water continuity equation,

$$\frac{\partial}{\partial t}h + \vec{\nabla} \cdot (\vec{u}h) = 0, \tag{A.1.1}$$

and substituting the geostrophic relation for h, mass conservation is derived as follows.

$$F \iint_{\Omega} \frac{\partial \psi}{\partial t}\, dA + F \iint_{\Omega} (\vec{u}_g \cdot \vec{\nabla})\psi \, dA + \iint_{\Omega} \vec{\nabla} \cdot \vec{u}_a \, dA = 0, \tag{A.1.2}$$

$$F \frac{d}{dt} \iint_{\Omega} \psi \, dA + F \iint_{\Omega} \vec{\nabla} \cdot (\vec{u}_g \psi) \, dA + \oint_{\partial\Omega} \vec{u}_a \cdot \hat{n} \, ds = 0, \tag{A.1.3}$$

$$F \frac{d}{dt} \iint_{\Omega} \psi \, dA + F \oint_{\partial\Omega} \psi \vec{u}_g \cdot \hat{n} \, dA + \oint_{\partial\Omega} \vec{u}_a \cdot \hat{n} \, ds = 0, \tag{A.1.4}$$

$$F \frac{d}{dt} \iint_{\Omega} \psi \, dA + \int_{\ell} \psi v_g \, dx + \int_{\ell} v_a \, dx = 0, \tag{A.1.5}$$

$$F \frac{d}{dt} \iint_{\Omega} \psi \, dA + \int_{\ell} \frac{\partial}{\partial x} \left(\frac{1}{2} \psi^2 \right) \, dx + \int_{\ell} v_a \, dx = 0. \tag{A.1.6}$$

If Ω is chosen such that it extends along the channel, the periodic boundary conditions cause the second term to vanish identically, giving

$$F \frac{d}{dt} \iint_{\Omega} \psi \, dA + \int_{\ell} v_a \, dx = 0. \tag{A.1.7}$$

If Ω is the entire channel, then the second integral vanishes and mass conservation can be expressed as

$$\frac{d}{dt} \iint_{\Omega} \psi \, dA = 0. \tag{A.1.8}$$

A.2 Conservation of Circulation

Following Stokes' theorem, the circulation is equal to the domain integrated vorticity,

$$C = \oint_{\partial\Omega} \vec{u} \cdot d\vec{t} = \iint_{\Omega} \omega dA. \tag{A.2.1}$$

Begin by cross-differentiating the $\mathcal{O}(\mathrm{Ro})$ momentum equations:

$$\begin{aligned}
&\frac{\partial}{\partial x}\mathcal{F}_{m,y} - \frac{\partial}{\partial y}\mathcal{F}_{m,x} \\
=&\frac{\partial}{\partial x}\left[\frac{\partial}{\partial t}v_g + u_g\frac{\partial}{\partial x}v_g + v_g\frac{\partial}{\partial y}v_g + u_a\right] - \frac{\partial}{\partial y}\left[\frac{\partial}{\partial y}u_g + u_g\frac{\partial}{\partial x}u_g + v_g\frac{\partial}{\partial y}u_g - v_a\right] && \text{(A.2.2)} \\
=&\left[\frac{\partial}{\partial t} + u_g\frac{\partial}{\partial x} + v_g\frac{\partial}{\partial y}\right]\left(\frac{\partial}{\partial x}v_g - \frac{\partial}{\partial y}u_g\right) + \frac{\partial}{\partial x}u_a + \frac{\partial}{\partial y}v_a && \text{(A.2.3)}
\end{aligned}$$

Domain integrating yields and evolution equation for the circulation.

$$\frac{\partial}{\partial t}C + \underbrace{\iint_{\Omega} \frac{\partial}{\partial x}u_a + \frac{\partial}{\partial y}v_a dA}_{\text{Zero by BCs}} = \iint_{\Omega} \frac{\partial}{\partial x}\mathcal{F}_{m,y} - \frac{\partial}{\partial y}\mathcal{F}_{m,x} dA \tag{A.2.4}$$

$$\begin{aligned}
\frac{\partial}{\partial t}C &= \int_0^{L_y} \mathcal{F}_{m,y}\big|_{x=L_x} dy + \int_{L_x}^{0} \mathcal{F}_{m,x}\big|_{y=L_y} dx \\
&\quad + \int_{L_y}^{0} \mathcal{F}_{m,y}\big|_{x=0} dy + \int_0^{L_x} \mathcal{F}_{m,x}\big|_{y=0} dx && \text{(A.2.5)} \\
&= \int_{L_x}^{0} \mathcal{F}_{m,x}\big|_{y=L_y} dx + \int_0^{L_x} \mathcal{F}_{m,x}\big|_{y=0} dx && \text{(A.2.6)}
\end{aligned}$$

The y-integral terms vanish by periodicity, and in the absence of forcing the global circulation is conserved. Otherwise, the evolution is governed by a boundary-integral of the forcing terms.

A.3 Deriving the evolution equation for $\langle q \rangle$

A.3.1 Zonally Averaged $\mathcal{O}(\mathrm{Ro})$ Zonal Momentum Equation

The $\mathcal{O}(\mathrm{Ro})$ form of equation (2.1.3) is

$$\frac{\partial}{\partial t}u_g + u_g\frac{\partial}{\partial x}u_g + v_g\frac{\partial}{\partial y}u_g - v_a = -\frac{\partial}{\partial x}\phi_a + \mathcal{F}_{m,x}, \tag{A.3.1}$$

which, after substituting the geostrophic relations and applying the $\langle\cdot\rangle$ operator, yields the following evolution equation:

$$\frac{\partial}{\partial t}\left\langle \frac{\partial}{\partial y}\psi_g \right\rangle + \left\langle \frac{\partial}{\partial x}\psi_g \cdot \frac{\partial^2}{\partial y^2}\psi_g \right\rangle = -\left\langle v_a \right\rangle - \left\langle \mathcal{F}_{m,x} \right\rangle . \tag{A.3.2}$$

A.3.2 Zonally Averaged $\mathcal{O}(\mathrm{Ro})$ Thermodynamic Equation

The $\mathcal{O}(\mathrm{Ro})$ form of equation (2.1.5) is

$$\frac{\partial}{\partial t}b_g + u_g\frac{\partial}{\partial x}b_g + v_g\frac{\partial}{\partial y}b_g + \mathrm{Bu}\cdot w_a = \mathcal{F}_b. \tag{A.3.3}$$

Applying the $\langle\cdot\rangle$ operator and substituting the geostrophic relations yields the following evolution equation. Note that equation (2.1.7) is used to replace the w_a term with a v_a term.

$$\frac{\partial}{\partial t}\left\langle \frac{\partial^2}{\partial z^2}\psi_g \right\rangle + \left\langle \left(u_g\frac{\partial}{\partial x} + v_g\frac{\partial}{\partial y}\right)\frac{\partial^2}{\partial z^2}\psi \right\rangle = \mathrm{Bu}\cdot\frac{\partial}{\partial y}\left\langle v_a \right\rangle + \frac{\partial}{\partial z}\left\langle \mathcal{F}_b \right\rangle \tag{A.3.4}$$

A.3.3 Eliminating v_a

Combining the $\mathcal{O}(\mathrm{Ro})$ Zonal Momentum and Thermodynamic equations to eliminate the ageostrophic velocity terms yields:

$$\begin{aligned} 0 = {} & \frac{\partial}{\partial t}\left\langle \frac{\partial^2}{\partial z^2}\psi_g \right\rangle + \left\langle \left(u_g\frac{\partial}{\partial x} + v_g\frac{\partial}{\partial y}\right)\frac{\partial^2}{\partial z^2}\psi \right\rangle \\ & \qquad + \mathrm{Bu}\left(\frac{\partial}{\partial y}\left(\frac{\partial}{\partial t}\left\langle \frac{\partial}{\partial y}\psi_g \right\rangle + \left\langle \frac{\partial}{\partial x}\psi_g \cdot \frac{\partial^2}{\partial y^2}\psi_g \right\rangle \right)\right) \end{aligned} \tag{A.3.5}$$

$$\begin{aligned} = {} & \frac{\partial}{\partial t}\left\langle \frac{1}{\mathrm{Bu}}\frac{\partial^2}{\partial z^2}\psi_g \right\rangle + \left\langle \left(u_g\frac{\partial}{\partial x} + v_g\frac{\partial}{\partial y}\right)\frac{1}{\mathrm{Bu}}\frac{\partial^2}{\partial z^2}\psi \right\rangle \\ & \qquad + \frac{\partial}{\partial t}\left\langle \frac{\partial^2}{\partial y^2}\psi_g \right\rangle + \frac{\partial}{\partial y}\left\langle \frac{\partial}{\partial x}\psi_g \cdot \frac{\partial^2}{\partial y^2}\psi_g \right\rangle \end{aligned} \tag{A.3.6}$$

$$\begin{aligned} = {} & \frac{\partial}{\partial t}\left\langle \frac{\partial^2}{\partial y^2}\psi_g + \frac{1}{\mathrm{Bu}}\frac{\partial^2}{\partial z^2}\psi_g \right\rangle + \left\langle \left(u_g\frac{\partial}{\partial x} + v_g\frac{\partial}{\partial y}\right)\frac{1}{\mathrm{Bu}}\frac{\partial^2}{\partial z^2}\psi \right\rangle \\ & \qquad + \frac{\partial}{\partial y}\left\langle \frac{\partial}{\partial x}\psi_g \cdot \frac{\partial^2}{\partial y^2}\psi_g \right\rangle \end{aligned} \tag{A.3.7}$$

$$\begin{aligned} = {} & \frac{\partial}{\partial t}\left\langle q \right\rangle + \left\langle \frac{\partial}{\partial x}\psi_g \frac{\partial}{\partial y}\left(\frac{\partial^2}{\partial y^2}\psi_g + \frac{1}{\mathrm{Bu}}\frac{\partial^2}{\partial z^2}\psi_g \right) \right. \\ & \qquad\qquad \left. - \frac{1}{\mathrm{Bu}}\frac{\partial}{\partial y}\psi_g \cdot \frac{\partial^3}{\partial x z^2}\psi_g + \frac{\partial^2}{\partial xy}\psi_g \frac{\partial^2}{\partial y^2}\psi_g \right\rangle \end{aligned} \tag{A.3.8}$$

To simplify the zonal average term, first note that

$$-\frac{\partial}{\partial y}\psi_g \cdot \frac{\partial^3}{\partial x z^2}\psi_g = \frac{\partial^2}{\partial xy}\psi_g \frac{\partial^2}{\partial z^2}\psi_g - \frac{\partial}{\partial x}\left(\frac{\partial}{\partial y}\psi_g \frac{\partial^2}{\partial z^2}\psi_g\right), \tag{A.3.9}$$

which changes the zonal mean expression to

$$\begin{aligned}\Bigg\langle \frac{\partial}{\partial x}\psi_g \frac{\partial}{\partial y}&\left(\frac{\partial^2}{\partial y^2}\psi_g + \frac{1}{\mathrm{Bu}}\frac{\partial^2}{\partial z^2}\psi_g\right) \\ &+ \frac{1}{\mathrm{Bu}}\left(\frac{\partial^2}{\partial xy}\psi_g \frac{\partial^2}{\partial z^2}\psi_g - \frac{\partial}{\partial x}\left(\frac{\partial}{\partial y}\psi_g \frac{\partial^2}{\partial z^2}\psi_g\right)\right) + \frac{\partial^2}{\partial xy}\psi_g \frac{\partial^2}{\partial y^2}\psi_g \Bigg\rangle\end{aligned} \tag{A.3.10}$$

The term $\frac{\partial}{\partial x}\left(\frac{\partial}{\partial y}\psi_g \frac{\partial^2}{\partial z^2}\psi_g\right)$ vanishes after applying $\langle\cdot\rangle$, leaving

$$\left\langle \frac{\partial}{\partial x}\psi_g \frac{\partial}{\partial y}\left(\frac{\partial^2}{\partial y^2}\psi_g + \frac{1}{\mathrm{Bu}}\frac{\partial^2}{\partial z^2}\psi_g\right) + \frac{1}{\mathrm{Bu}}\frac{\partial^2}{\partial xy}\psi_g \frac{\partial^2}{\partial z^2}\psi_g + \frac{\partial^2}{\partial xy}\psi_g \frac{\partial^2}{\partial y^2}\psi_g \right\rangle \tag{A.3.11}$$

$$= \left\langle \frac{\partial}{\partial x}\psi_g \frac{\partial}{\partial y}\left(\frac{\partial^2}{\partial y^2}\psi_g + \frac{1}{\mathrm{Bu}}\frac{\partial^2}{\partial z^2}\psi_g\right) + \frac{\partial^2}{\partial xy}\psi_g\left(\frac{\partial^2}{\partial y^2}\psi_g + \frac{1}{\mathrm{Bu}}\psi_g \frac{\partial^2}{\partial z^2}\psi_g\right)\right\rangle \tag{A.3.12}$$

$$= \frac{\partial}{\partial y}\left\langle \frac{\partial}{\partial x}\psi \cdot \left(\frac{\partial^2}{\partial y^2}\psi_g + \frac{1}{\mathrm{Bu}}\frac{\partial^2}{\partial z^2}\psi_g\right)\right\rangle \tag{A.3.13}$$

Substituting (A.3.13) into (A.3.8) yields:

$$\frac{\partial}{\partial t}\langle q\rangle + \frac{\partial}{\partial y}\left\langle \frac{\partial}{\partial x}\psi \cdot \left(\frac{\partial^2}{\partial y^2}\psi_g + \frac{1}{\mathrm{Bu}}\frac{\partial^2}{\partial z^2}\psi_g\right)\right\rangle = 0 \tag{A.3.14}$$

Further, since $\left\langle \frac{\partial}{\partial x}\psi_g \frac{\partial^2}{\partial x^2}\psi_g \right\rangle = \left\langle \frac{1}{2}\frac{\partial}{\partial x}\left(\left(\frac{\partial}{\partial x}\psi_g\right)^2\right)\right\rangle = 0$, we may express this as:

$$\frac{\partial}{\partial t}\langle q\rangle + \frac{\partial}{\partial y}\langle v_g q\rangle = 0 \tag{A.3.15}$$

A.4 Zonal Decomposition for 2D Quasigeostrophy

From Pedlosky (p. 88), the non-dimensional zonal momentum and continuity equations are:

$$\mathrm{Ro}\left(\frac{\partial}{\partial t}u + u\frac{\partial}{\partial x}u + v\frac{\partial}{\partial y}u\right) - v = -\frac{\partial}{\partial x}\eta \tag{A.4.1}$$

$$\mathrm{Ro}\,\mathrm{Fr}\left(\frac{\partial}{\partial t}\eta + u\frac{\partial}{\partial x}\eta + v\frac{\partial}{\partial y}\eta\right) + (1 + \mathrm{Ro}\,\mathrm{Fr}\,\eta)\left(\frac{\partial}{\partial x}u + \frac{\partial}{\partial y}v\right) = 0 \tag{A.4.2}$$

A.4.1 $\mathcal{O}(\mathrm{Ro})$ Zonal Momentum

Beginning with the $\mathcal{O}(\mathrm{Ro})$ zonal momentum equation,

$$\frac{\partial}{\partial t}u_g + u_g\frac{\partial}{\partial x}u_g + v_g\frac{\partial}{\partial y}u_g - v_a = -\frac{\partial}{\partial x}\eta_a, \tag{A.4.3}$$

apply the zonal averaging operator $\langle\cdot\rangle$ and eliminate zonal derivative terms to obtain

$$\frac{\partial}{\partial t}\langle u_g\rangle + \underbrace{\left\langle \frac{1}{2}\frac{\partial}{\partial x}(u_g^2)\right\rangle}_{\to 0} + \left\langle v_g\frac{\partial}{\partial y}u_g\right\rangle - \langle v_a\rangle = -\underbrace{\left\langle \frac{\partial}{\partial x}\eta_a\right\rangle}_{\to 0} \tag{A.4.4}$$

Using the geostrophic relations, this can then be written as

$$\frac{\partial}{\partial t}\langle u_g\rangle - \left\langle \frac{\partial}{\partial x}\psi_g \cdot \frac{\partial^2}{\partial y^2}\psi_g\right\rangle = \langle v_a\rangle . \tag{A.4.5}$$

A.4.2 $\mathcal{O}(\mathrm{Ro})$ Continuity

Starting with the $\mathcal{O}(\mathrm{Ro})$ continuity equation,

$$\mathrm{Fr}\left(\frac{\partial}{\partial t}\eta_g + \frac{\partial}{\partial x}(h_g u_g) + \frac{\partial}{\partial y}(h_g v_g)\right) + \frac{\partial}{\partial x}u_a + \frac{\partial}{\partial y}v_a = 0, \tag{A.4.6}$$

apply the zonal averaging operator $\langle\cdot\rangle$ and eliminate the zonal derivative terms to obtain

$$\mathrm{Fr}\,\frac{\partial}{\partial t}\langle\eta_g\rangle + \mathrm{Fr}\left\langle \frac{\partial}{\partial y}(h_g v_g)\right\rangle = -\frac{\partial}{\partial y}\langle v_a\rangle , \tag{A.4.7}$$

into which substituting the geostrophic relation yields

$$\mathrm{Fr}\,\frac{\partial}{\partial t}\langle\psi_g\rangle + \mathrm{Fr}\left\langle \frac{\partial}{\partial y}\left(\psi_g\frac{\partial}{\partial x}\psi_g\right)\right\rangle = -\frac{\partial}{\partial y}\langle v_a\rangle . \tag{A.4.8}$$

We can interchange the zonal averaging and meridional derivative in the second term, yielding the zonal average of a zonal derivative, which again vanishes by periodicity. Ultimately, the zonally averaged $\mathcal{O}(\mathrm{Ro})$ continuity equation becomes

$$\mathrm{Fr}\,\frac{\partial}{\partial t}\langle\psi_g\rangle = -\frac{\partial}{\partial y}\langle v_a\rangle . \tag{A.4.9}$$

A.4.3 Eliminating v_a

It is again necessary to eliminate the ageostrophic meridional velocity from the two equations. Substituting the $\mathcal{O}(\mathrm{Ro})$ zonal momentum equation into the $\mathcal{O}(\mathrm{Ro})$ continuity equation yields the following.

$$\mathrm{Fr}\,\frac{\partial}{\partial t}\left\langle \psi_g \right\rangle = -\frac{\partial}{\partial y}\left\{\frac{\partial}{\partial t}\left\langle u_g \right\rangle - \left\langle \frac{\partial}{\partial x}\psi_g \cdot \frac{\partial^2}{\partial y^2}\psi_g \right\rangle\right\} \tag{A.4.10}$$

$$\mathrm{Fr}\,\frac{\partial}{\partial t}\left\langle \psi_g \right\rangle = -\frac{\partial}{\partial y}\left\{-\frac{\partial}{\partial t}\left\langle \frac{\partial}{\partial y}\psi_g \right\rangle - \left\langle \frac{\partial}{\partial x}\psi_g \cdot \frac{\partial^2}{\partial y^2}\psi_g \right\rangle\right\} \tag{A.4.11}$$

$$-\mathrm{Fr}\,\frac{\partial}{\partial t}\left\langle \psi_g \right\rangle + \frac{\partial}{\partial t}\left\langle \frac{\partial^2}{\partial y^2}\psi_g \right\rangle = -\frac{\partial}{\partial y}\left\langle \frac{\partial}{\partial x}\psi_g \cdot \frac{\partial^2}{\partial y^2}\psi_g \right\rangle \tag{A.4.12}$$

$$\frac{\partial}{\partial t}\left\langle \frac{\partial^2}{\partial y^2}\psi_g - \mathrm{Fr}\,\psi_g \right\rangle = -\frac{\partial}{\partial y}\left\langle \frac{\partial}{\partial x}\psi_g \cdot \frac{\partial^2}{\partial y^2}\psi_g \right\rangle \tag{A.4.13}$$

$$\frac{\partial}{\partial t}\overline{q} = -\frac{\partial}{\partial y}\left\langle v_g \cdot \frac{\partial^2}{\partial y^2}\psi_g \right\rangle \tag{A.4.14}$$

Further, since $\left\langle \frac{\partial}{\partial x}\psi_g \cdot \mathrm{Fr}\,\psi_g \right\rangle = \frac{1}{2}\,\mathrm{Fr}\left\langle \frac{\partial}{\partial x}\left(\psi_g^2\right)\right\rangle = 0$, we may express this as:

$$\frac{\partial}{\partial t}\overline{q} + \frac{\partial}{\partial y}\left\langle v_g q \right\rangle = 0 \tag{A.4.15}$$

A.5 Coefficients for $\ddot{\mathcal{F}}$

$$a = \frac{1}{6L_y}\left(\frac{\partial^2}{\partial y^2}\bar{\mathcal{F}}_{m,x}(L_y) - \frac{\partial^2}{\partial y^2}\bar{\mathcal{F}}_{m,x}(0)\right) \tag{A.5.1}$$

$$b = \frac{1}{2}\frac{\partial^2}{\partial y^2}\bar{\mathcal{F}}(0) \tag{A.5.2}$$

$$c = \frac{1}{L_y}\left(\frac{\partial}{\partial t}u_N - \frac{\partial}{\partial t}u_S\right) - \frac{L_y}{6}\left(2\frac{\partial^2}{\partial y^2}\bar{\mathcal{F}}_{m,x}(0) + \frac{\partial^2}{\partial y^2}\bar{\mathcal{F}}_{m,x}(L_y)\right) \tag{A.5.3}$$

$$d = \frac{\partial}{\partial t}u_S \tag{A.5.4}$$

Appendix B

Derivation of Quasi-Geostrophic Meddy Linear Stability Problem

In cylindrical coordinates we can write the geostrophic velocity components in the same manner as in the Cartesian coordinate system; that is:

$$\vec{u}_g = \vec{k} \times \nabla \psi.$$

From the definition of the gradient operator above we see that

$$u_{r,g} = -\frac{1}{r}\partial_\theta \psi \qquad \text{and} \qquad u_{\theta,g} = \partial_r \psi,$$

in the cylindrical coordinate system. Furthermore, the potential vorticity in the cylindrical coordinate system can be written as:

$$q = \nabla_h^2 \psi + \frac{f_0^2}{N^2}\partial_{zz}\psi,$$

where N is taken to be constant. Using the definition of the Laplacian operator we evaluate this as:

$$q = \frac{1}{r}\partial_r\big(r\partial_r\psi\big) + \frac{1}{r^2}\partial_{\theta\theta}\psi + \frac{f_0^2}{N^2}\partial_{zz}\psi.$$

The quasi-geostrophic potential vorticity equation can now be rewritten in terms of the Jacobian in the cylindrical coordinate system, $J_{\vec{r}}$, as:

$$\partial_t q + J_{\vec{r}}(\psi, q) = 0.$$

Next, if we assume that the basic state is periodic in the θ coordinate, then the basic-state fields can be expressed as:

$$\psi = \Psi(r,z), \quad u_r = 0, \quad u_\theta = \Psi_r, \quad q = Q(r,z) = \frac{1}{r}\partial_r\big(r\partial_r\Psi\big) + \frac{f_0^2}{N^2}\partial_{zz}\Psi,$$

We consider perturbations around this background state in the form:

$$\psi = \Psi(r,z) + \psi'(r,\theta,z,t),$$
$$q = Q(r,z) + q'(r,\theta,z,t).$$

Upon substitution into the quasi-geostrophic evolution equation and linearizing, we get the linear equation:

$$\partial_t q' - \frac{1}{r}\partial_\theta \psi' \partial_r Q + \partial_r \Psi \left(\frac{1}{r}\partial_\theta q'\right) = 0.$$

We assume a normal mode solution of the form:

$$[q', \psi'] = \Re\left\{\left[\widehat{q}, \widehat{\psi}\right](r,z)e^{i(k\theta-\omega t)}\right\}.$$

Upon substitution into the linear equation above, and cancellation of the exponential factor, we get the normal mode equation:

$$i\omega\widehat{q} = -\frac{1}{r}ik\,\partial_r\Psi\,\widehat{q} - \frac{1}{r}ik\widehat{\psi}\,\partial_r Q. \qquad \Longrightarrow \qquad \frac{\omega}{k}\widehat{q} = \frac{1}{r}\,\partial_r\Psi\,\widehat{q} - \frac{1}{r}\,Q_r\,\widehat{\psi}$$

We now apply the relationship between q and ψ to write $\widehat{q}$ as:

$$\widehat{q} = \left(\frac{1}{r}\partial_r + \partial_{rr} - \frac{k^2}{r^2}\right)\widehat{\psi} + \frac{f_0^2}{N^2}\partial_{zz}\widehat{\psi}.$$

Therefore, we get the normal mode equation in terms of $\widehat{\psi}$ as:

$$\frac{\omega}{k}\left(\frac{1}{r}\partial_r + \partial_{rr} - \frac{k^2}{r^2} + \frac{f_0^2}{N^2}\partial_{zz}\right)\widehat{\psi} = \left[\frac{1}{r}\partial_r\Psi\left(\frac{1}{r}\partial_r + \partial_{rr} - \frac{k^2}{r^2} + \frac{f_0^2}{N^2}\partial_{zz}\right) - \frac{1}{r}\partial_r Q\right]\widehat{\psi}. \tag{B.0.1}$$

In matrix form, this can be written as the generalized eigenvalue problem:

$$A\widehat{\psi} = Bc\widehat{\psi}, \tag{B.0.2}$$

where

$$\begin{aligned}
A &= \left[\frac{1}{r}\partial_r\Psi\left(\frac{1}{r}\partial_r + \partial_{rr} - \frac{k^2}{r^2} + \frac{f_0^2}{N^2}\partial_{zz}\right) - \frac{1}{r}\partial_r Q\right] && \text{(B.0.3)}\\
&= \left[\frac{1}{r}\partial_r\Psi B - \frac{1}{r}\partial_r Q\right], && \text{(B.0.4)}\\
B &= \left[\frac{1}{r}\partial_r + \partial_{rr} - \frac{k^2}{r^2} + \frac{f_0^2}{N^2}\partial_{zz}\right], && \text{(B.0.5)}\\
c &= \tfrac{\omega}{k}. && \text{(B.0.6)}\\
& && \text{(B.0.7)}
\end{aligned}$$